UNIVERSITÄT BAYREUTH

Lehrstuhl für Kristallographie

Aperiodic Molecular Ferroelectric Crystals

Von der Universität Bayreuth
zur Erlangung des akademischen Grades eines
Doktors der Naturwissenschaften (Dr. rer. nat.)
genehmigte Abhandlung

vorgelegt von
Leila Noohinejad
aus Tabriz, Iran

1. Gutachter: Prof. dr. Sander van Smaalen
2. Gutachter: Prof. em. Chapuis Gervais

Tag der Einreichung: 13. July 2016
Tag des Kolloquiums: 10. November 2016

For My Angel Called ***Mother***

Acknowledgement

I first wish to express my deepest appreciation to my *"Doctorvater"* Prof. dr. Sander van Smaalen who gave me the opportunity to be a member of his research team. I am thankful for his generous and insightful guidance on both my research and writing, his patient and untiring moral support and his invaluable mentoring on my life and education during *"Promotion"* in Bayreuth. He taught me how to deal with scientific problems in a well organised, professional and ethical manner, skills and values that have carried over to my personal life. Working for Sander has been both a huge pleasure and an immense privilege.

I greatly appreciate the motivation and support of PD. Dr. Andreas Schönleber for his time, valuable advice and discussion on data processing and feedback on the research projects and presentations. From him I also learned to present and teach scientific work in a way that is both accessible and professional. I express my warm appreciation of Mrs. Denise Kelk-Huth for both her kind care as a colleague and her support as a friend. Thanks to Mrs. Wil Meijer for the warm atmosphere and pleasant moments she created in the lab of Crystallography.

I would like to thank my fellow colleagues and faculty staffs especially, Dr. Maxim Bykov, Somnath Dey, Franz Fischer, Dr. Sk Imran Ali, Dr. Prathapa S. Jagannatha, Kerstin Küspert, Dr. Swastik Mondal, Sitaram Ramakrishnan, Alfred Suttner, Dr. Alexander Wölfel, and Dr. Jian Zhang who always motivated me with their help and positive energies. Many thanks to Dr. Jake Chandler and Claudio Eisele not only as good friends but also for proofreading of this manuscript. I am thankful to Dr. Christian Hübschle for German translation of summary and for enlightening me about the research.

My kind appreciation goes to Prof. dr. Natalia Dubrovinskaia for encouraging me with kind words and for being a source of motivation during my study.

I thank the Deutscher Akademischer Austauschdienst (DAAD) for financial support. Especially, I would like to thank the team of DAAD- section Iran, Mrs.

Hosseini-Razi, Mrs. Seeler, and Mrs. Pietsch for their generous guidance and help to gain more knowledge of German Culture. It will be an honour for me to be a alumni of DAAD.

I wish to express my warm and kind appreciation to my former supervisor, Dr. Seyed. A. Hosseini-Yazdi for his priceless encouragement and counselling especially during the time I needed to work far from Bayreuth and he was kindly hosting me for one semester at his lab at University of Tbariz in 2015.

I owe many thanks to Dr. Matthias Zeller from University of Youngstown (recently, at Purdue University) who introduced to me Crystallography in such a fascinating way that it to being the major research topic of my PhD studies.

I would like to warmly thank Luca Cesarano for bringing positive energy around me with enthusiasm also for his help in solving mathematical problems and theory. Luca's comprehension, support, and kindness created memorable memories and made me to feel at home.

I greatly appreciate Mrs and Mr Holz-Koberg, Johannes and Evelin, who were like a family for me, supporting me with their love and care.

Beloved Dr. Saeedeh Aliaskari-Sohi, dearest Dr. Mehrnaz Karimi, Dr. Matteo Masotta, Dr. Roya Montakhabi, Dr. Amir H. Pahlevani and Dr. Salimeh Yasaei-Sekeh who gave their love, care, and with whom I shared my happiness and difficult times are also greatly acknowledged.

Many thanks to my dearest Zahra Ebrahimi-Asl, who is always there for me, even when I can't be here for myself.

Last but not least, there are no words to express my gratitude and thanks to my inspiration and mentors: my beloved parents, **Maasume Azimzade**, and **Qodrat Noohinejad**. This work would not have been possible without their patience and everlasting support. The love of my parents and siblings, to whom I owe everything, has been the major spiritual support in my life.

Contents

Chapter 1

Introduction

The history of discovery of ferroelectricity in single crystals (Rochelle salt), dates back to 1921. Later, in the early to mid 1940s, during World War II, the pressing need for larger capacitors lead to the discovery of ferroelectricity in ABO_3-type perovskite, $BaTiO_3$ (Haertling, 1999), with a high dielectric constant. Since then, there has been a continuous succession of new materials and technological developments that have led to a significant number of industrial and commercial applications that can be directly credited to this most unusual phenomenon.

Towards designing new molecular ferroelectrics, strong hydrogen bonds (H-bonds; Gilli and Gilli (2009)) have received considerable attention, due to their functional ability to control properties of many different systems. Novel solid-state materials can be designed by particular donor and acceptor functional groups governed by a H-bond pattern. Supramolocular assemblies are designed for ferroelectrics where H-bonds are one of the non-covalent bonds to bind two molecular moieties. The H-bond is much weaker than covalent bonds. Therefore, H-bonded systems easily undergo temperature or pressure induced phase transitions, as the result of exchanges of H-bonds, proton transfer, or proton disordering (Gilli and Gilli, 2009; Jeffrey, 1997). Further experimental evidence will be discussed in Chapters 4, 3, and 5. The effect of H-bonds on physical properties of materials requires an understanding of crystal structures. Aside from spectroscopic and theoretical methods, diffraction methods are a very important tool for studying hydrogen bonds. Structural analysis by single crystal X-ray or neutron diffraction may provide very precise information about not only interatomic distances, but also the exact location of H atoms in the structure.

The purpose of the present thesis is to study temperature-dependent phase transition in hydrogen bonded molecular compounds, in order to gain knowledge about

the role of hydrogen bonds in structural phase transitions. Single crystal X-ray diffraction is applied to two hydrogen bonded supramolecular compounds, which undergo phase transitions to incommensurately modulated phases. Hence, Chapter 2 gives an introduction to aperiodic crystallography, with a focus on incommensurately and commensurately modulated molecular crystals. The concept of a superspace approach (van Smaalen, 2012) is described. An overview to molecular aperiodic crystals is given and special methods for molecular compounds, i.e. rigid bodies, are introduced.

The study of phase transitions is at the core of condensed-matter physics. The material undergoes a change of symmetry at most phase transitions. The ferroelectric phase is defined by the possessing a spontaneous polarization (P_s). Paraelectric to ferroelectric phase transition are results from structural changes in crystal and are able to be distinguished from behavior of electric polarization, which can be reversed by application of an external electric field (Lines and Glass, 2001; Kittle, 2005) (Fig. 1.1).

Polarization hysteresis loop is the characteristic of ferroelectric materials, which arises due to the presence of ferroelectric domains in the crystal. At coercive field, E_c, polarization reversal occurs giving a large dielectric non-linearity [Fig. 1.1(c)]. The area within loop is a measure of the energy required to twice reverse the polarization. At zero field, the electric displacement within a single domain (saturated value of the displacement) has two values corresponding to the opposite orientation of the spontaneous polarization ($\pm P_s$),(Lines and Glass, 2001). In a multi-domain crystal, the average zero-field displacement can have any value between these two extremes. In principle, the spontaneous polarization is equal to the saturation value of the electric displacement extrapolated to zero field, [Fig. 1.1(b-c)], and usually it is larger than the remanent polarization, P_r, which is displacement at zero field (Lines and Glass, 2001). The distinguishing feature of ferroelectrics is that the spontaneous polarization can be reversed by a suitably strong applied electric field in the opposite direction [Fig. 1.1 (a)]. The polarization is therefore dependent on the current electric field, and the direction of electric field. Therefore, these materials can be used as a memory function, and ferroelectric capacitors.

Fig. 1.2(a) shows temperature-dependent hysteresis loops for the co-crystal of phenazine-chloranilic acid (abbr. Phz-H_2ca). The width of the loop at lower temperature is larger. By increasing the temperature, the coercive field decreases [Fig. 1.2 (b)], the loops become sharper and at temperature larger than $T_c^I = 253$ K, the loop is disappearing and the crystal becomes paraelectric [Fig. 1.2(a)]. At $T_c^I = 253$

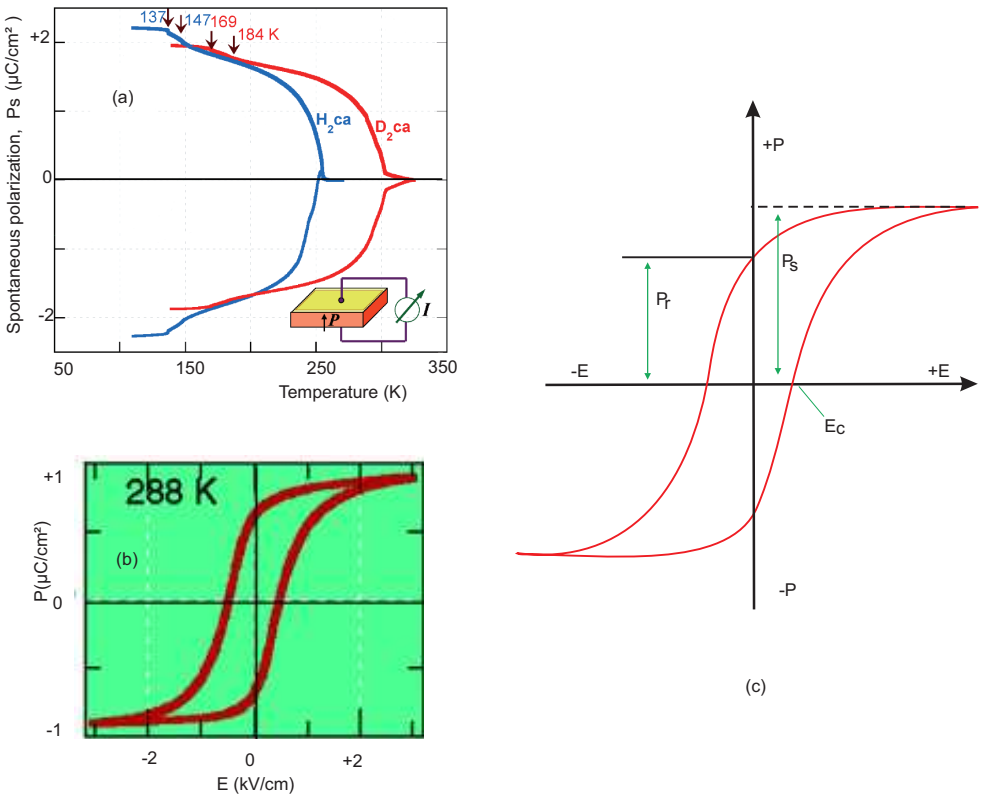

Figure 1.1: (a) Temperature dependence of spontaneous polarization P_s along the crystallographic *b*-axis of Phz-H_2ca and its deuterated co-crystals (reprinted from Fig.8 of Horiuchi et al. (2009)). (b) A hysteresis loop in deuterated co-crystal of Phz-D_2a along the direction of *b*-axis at T= 288 K (reprinted from graphical abstract of Horiuchi, Kumai and Tokura (2005)). (c) A hysteresis loop (P–E), illustrating the coercive field, E_c, the spontaneous polarization, P_s, and the remanent polarization, P_r. The behaviour of the loop is the same as Phz-D_2a, that P_s is equal to the saturated polarisation, since, the direction of E has been chosen along the direction of the P_s, i.e. along *b*-axis.

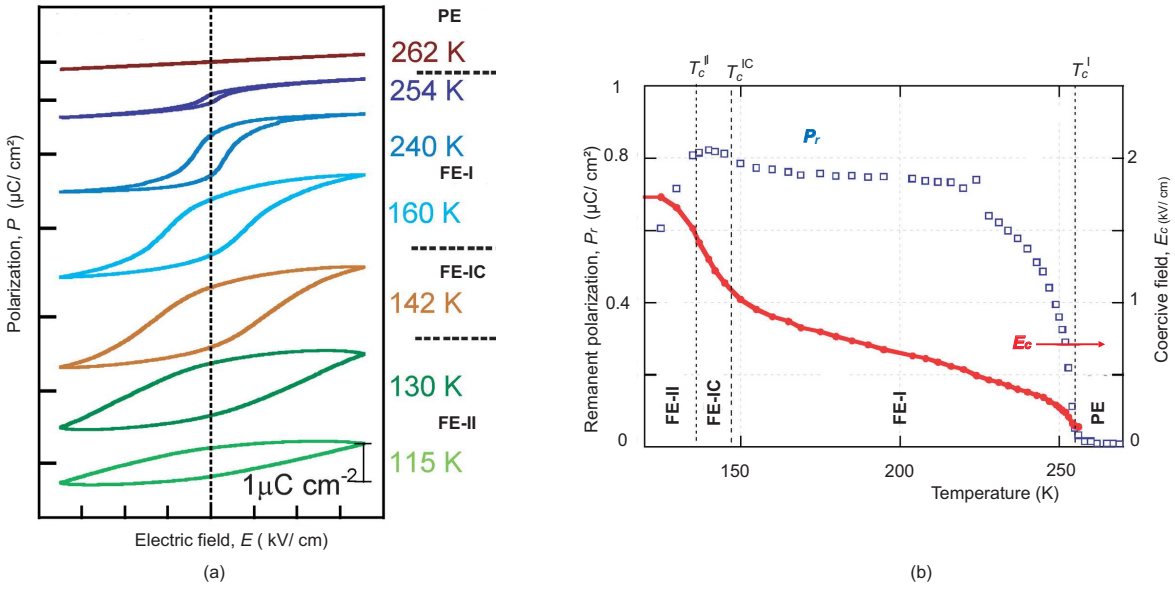

Figure 1.2: Temperature dependence of hysteresis loops in Phz-H_2ca (a). Temperature dependence of remanent polarization P_r and coercive electric field E_c (b). Compare the curves in (b) with the change of size of loops shown in (a)(*a* and *b* are reprinted from Fig.7 of Horiuchi et al. (2009)).

K, E_c has the minimum value of external field sufficient to reverse the spontaneous polarization. The remanent polarization P_r increases stepwise up to T_c^{IC}. Below T_c^{IC}, although E_c increases rapidly, the P_r does not change significantly (Horiuchi et al., 2009) [Fig. 1.2 (b)].

Since the electrical polarization, P, is a vector, the point group of the crystal must not contain any symmetry operator which changes the direction of polarization, e.g. an inversion operator. The crystal must be polar, i.e. have a polar space group. Eleven out of thirty two crystal classes are centrosymmetric (non-polar crystal). Ten out of twenty one non-centrosymmetric crystal classes are characterized by a unique polar axis. Crystals belonging to these classes are considered to be polar because they may posses a spontaneous polarization (Lines and Glass, 2001).

All polar space groups are non-centrosymmetric, but the reverse is not true. For example, the space group $P2_1$ and superspace group $P2_1(1/2\,\sigma_2\,1/2)0$ are both non-centrosymmetric and polar where ferroelectric phase transition is reported in lower temperatures for Phz-H_2ca (Chapters 4 and 3). On the other hand, the space group $P2_12_12_1$ is non-centrosymmetric but not polar where the reduction of symmetry from centrosymmetric to non-centrosymmetric space group at lower temperature is

not a ferroelectric phase transition (Chapter 5). In summary, there are only ten crystal classes that allow a macroscopic polarization: 1, 2, m, mm2, 4, 4mm, 3, 3m, 6, 6mm.

Most ferroelectric materials for applications belong to the class of inorganic perovskite oxides, specifically barium titanate (BTO) and lead zirconate titanate (PZT) (Gonzalo, 1990). However, these materials have some drawbacks, e.g. heavy weight, high-processing temperatures. Furthermore, a high lead content concerning environmental issues. Rochelle salt (Valasek, 1920), is not only the first discovered ferroelectric material but it is also the first molecular ferroelectric. Although, later, a few other molecular systems, such as thiourea (Goldsmith and White, 1959), triglycine sulfate (TGS) (Hashino et al., 1959), and vinylidene fluoride copolymers (Furukawa, 1989) were discovered, their poor performance compare to BTO kept them as materials without widespread use. It is only recently that the organic ferroelectrics received considerable attention. The discovery of diisopropylammonium bromide (DIPAB) (Fu et al., 2013) (with a polar point group at room temperature) which posses spontaneous polarization, $P_s = 23\ \mu C/cm^2$ below $T_c = 426$ K (remarkably matching that of BTO with $P_s = 26\ \mu C/cm^2$ below $T_c = 393$K (Lines and Glass, 2001)) was a significant step in designing organic ferroelectrics. Ferroelectricity in DIPAB is the result of alignment of the polar molecules in the crystal. Also, successive development of organic ferroelectrics is reported for the hydrogen bonded assemblies where the ferroelectricity is governed by proton disordering or proton transfer within hydrogen bonds (Horiuchi and Tokura, 2008). An example from this family is croconic acid (Horiuchi et al., 2010), as a single-component molecular crystal, with comparable properties of the inorganic ones with $P_s = 21\ \mu C/cm^2$ at room temperature. Croconic acid is a π-conjugated system with keto-enol transformation which causes polar hydrogen bond at crystalline state. These developments in ferroelectrics are reflected in two recent publications, titled *Ferroelectric Organic Materials Catch Up with Oxides* (Bonnell, 2013) and *Can molecular ferroelectrics challenge pure inorganic ones?* (Wang and Gao, 2013).

Ferroelectricity has been reported for H-bonded supramolecular crystals with binary neutral acid-base systems, i.e. co-crystals of phenazine (Phz) as base with three acids, namely 2,5-halo-3,6-dihydroxy-p-benzoquinone (chloranilic acid, H_2ca), bromanilic acid (H_2ba), and fluoranilic acid (H_2fa) (Horiuchi et al., 2009). Both Phz as a base and H_2ca as an acid are π-conjugated system. H_2ca is a strong diprotic acid (pk1=0.73, pk2=3.08) which can be dissociate to monoanion and dianion based on the strength of the base Fig. 1.3. Due to the π-conjugated systems of both acid

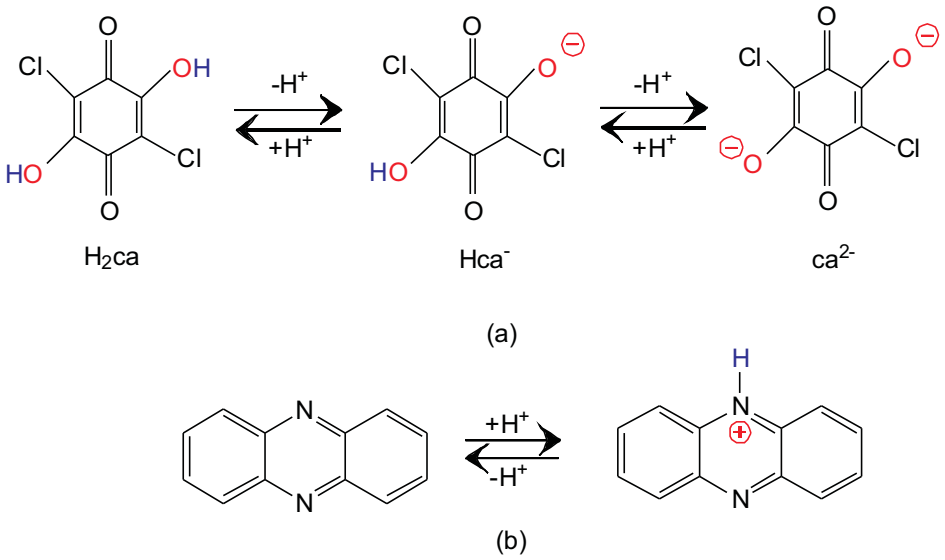

Figure 1.3: (a) Dissociation of acid H_2ca to monoanion and dianion. (b) Protonation of phenazine.

and base, the organic co-crystal has a dark brown color. Hydrogen bonded linear chains are governed by alternating molecules of Phz and H_2ca, Fig.1.4.

The ferroelectric phase transitions have been confirmed by pyroelectric charge measurements at different temperatures (Horiuchi et al., 2009), Figs. 1.1 and 1.2. At room temperature the co-crystal of Phz-H_2ca is in paraelectric phase, (PE-phase). Below $T_c^I = 253$ K, the crystal undergoes to a first ferroelectric phase transition (FE-I phase). Further cooling, follows by two more ferroelectric phase transitions: an incommensurate phase, below $T_c^{IC} = 147$ K (FE-IC phase), and a commensurate phase below $T_c^{II} = 137$ K (FE-II phase) (Horiuchi et al., 2009).

The crystal structure of Phz-H_2ca has been established within the PE phase. Both Phz and H_2ca are neutral and all hydrogen bonds between them are equivalent by the symmetry of the centrosymmetric space group $P2_1/n$ (Horiuchi, Ishii, Kumai, Okimoto, Tachibana, Nagaosa and Tokura, 2005), Fig.1.4. It has been found that below $T_c^I = 253$ K, the reduction of symmetry to a polar space group $P2_1$ is the result of acidic H atoms within one of the two of the intermolecular O–H$\cdots$N, H-bonds (Horiuchi, Ishii, Kumai, Okimoto, Tachibana, Nagaosa and Tokura, 2005; Gotoh et al., 2007; Kumai et al., 2007). The understanding of ferroelectricity within incommensurate or commensurate phases belongs to number of unsolved problems of solid-state physics in relation to ferroelectricity. Hence, Chapters 4 and 3 are

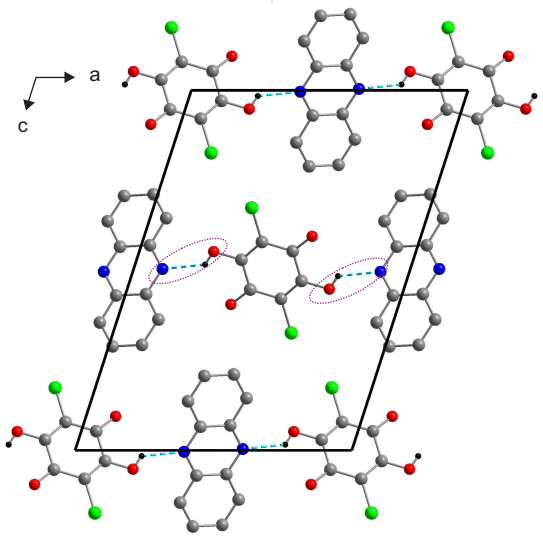

Figure 1.4: Projection of the crystal structure of Phz–H_2ca at ambient condition along **b** axis. Equivalent H-bonded layers of Phz–H_2ca are shown in half a unit cell. Two active H-bonded sites are indicated in dashed-lined ellipses. The atoms are shown for nitrogen in blue, oxygen in red, carbon in gray, hydrogen in black, and chlorine in green.

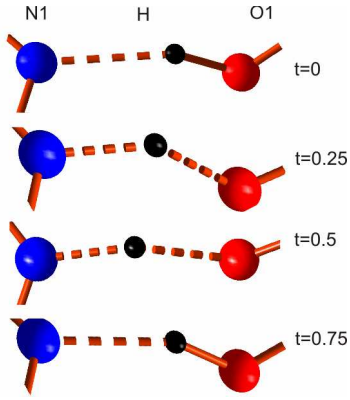

Figure 1.5: Hydrogen displacement between N1 and O1 through the hydrogen bond at four valid values of phase t of modulation wave at FE-II phase in the hydrogen bonded co-crystal of Phz–H_2ca. Details will be discussed in Chapter 4.

dedicated to the behavior of Phz-H_2ca in its commensurate and incommensurate ferroelectric phases, respectively.

Another series of supramolecular ferroelectrics belong to the family of hydrogen bonded hybrid organic-inorganic complexes. Hybrid materials combine the advantageous properties of inorganic solids with those of organic molecules. Overlapping the p-orbitals between adjacent conjugated organic molecules eases charge transfer. In addition, inorganic backbones are formed by strong covalent or ionic metal–halogen bonds to form an extended framework which allows magnetic interactions. The H-bond is a bridge between organic and inorganic blocks. The functional groups in organic molecules arrange in a way that makes hydrogen bond with the halogen atoms of the inorganic block. This type of hydrogen bond resembles those of pure organic ferroelectrics (Chapters 4 and 3).

Morpholinium, as organic block has been used with halogenoantimonates (III) and halogenobismuthates (III) as inorganic blocks with stoichiometry of RMX_4 (Owczarek et al., 2013) and R_2MX_5 (Owczarek et al., 2012) (R stands for organic cation, M: Sb(III), Bi(III), and X: Cl, Br, I). The complexes with stoichiometry R_2MX_5 show non-linear optical, dielectric dispersion and polar properties. Among RMX_4 analogs, only $[C_4H_{10}NO][BiBr_4]$ undergoes structural phase transition which is ferroelastic (Owczarek et al., 2013). Perchlorate or tetrafluoroborate anions with pyridinium (Czarenki et al., 1994a), (Czarenki et al., 1994b), or imidazolium (Pajak et al., 2004; Czapla et al., 2005) cations belong to the RMX_4 family that include aromatic or cycloalkane amine with inorganic acids with tetrahedral geometry. The mechanism of ferroelectric phase transition is related to the movement and partial ordering both of the dipolar cationic moieties and of the distorted tetrahedral anions at lower temperatures in comparison to high temperatures. On the other hand, in the case of cation, 1,4-diazabicyclo[2.2.2]octane, the mechanism of phase transition is connected to proton displacement within hydrogen bond (Katrusiak and Szafranski, 1999).

The behavior of morpholinium cation as cycloalkane amine with inorganic acids $[BF_4]$ (Owczarek et al., 2008), $[ClO_4]$ (Grigoriev et al., 2008), and $[ReO_4]$ (Grigoriev et al., 2007) has been extensively studied. The morpholinium cation makes hydrogen bonds with different ionic blocks that affect the dynamics of anion. Temperature dependent measurements have been done in order to track the behaviour of complex of morpholinium cation with tetrafluoroborate anion (Fig. 1.6) (Szklarz et al., 2009; Owczarek et al., 2008; 2011). The ionic complex undergoes two phase transitions, upon cooling. At room temperature, the crystal posses centrosymmetric

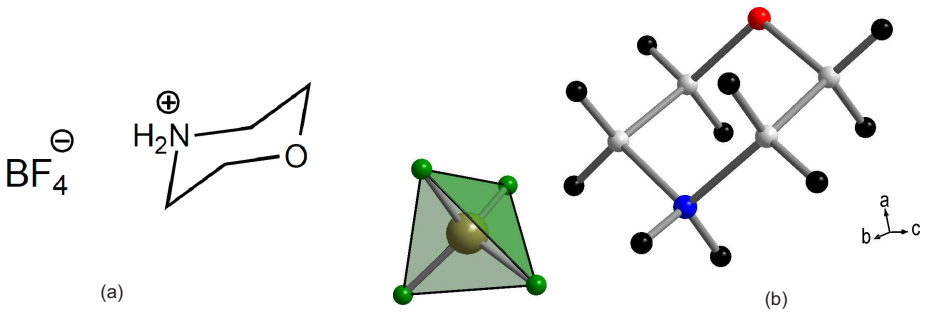

Figure 1.6: (a) Schematic depiction of molecular structure of morpholinium tetrafluoroborate. (b) Molecular configuration of morpholinium cation and tetrafluoroborate anion. The atoms are shown for nitrogen in blue, oxygen in red, carbon in gray, hydrogen in black, and BF_4 anion in a green tetrahedral.

space group *Pnam* and contains H-bonded $[C_4H_{10}NO]^+$ and $[BF_4]^-$ in the unit cell (Fig. 1.7). The single crystal X-ray structure at several temperatures 160, 180, 240, 290 K, with highly disordered anion with orthorhombic symmetry of space group *Pnam* has been reported (phase I) by Szklarz et al. (2009). At lower temperatures, the crystal undergoes two phase transitions: below $T_c^I = 153$ K the crystal to an incommensurate phase (phase II) (Szklarz et al., 2009) and below $T_c^{II} = 117/118$ K (phase III) to a commensurate phase or a threefold superstructure (Szklarz et al., 2009; Owczarek et al., 2008).

In order to analyse the phase transition mechanism, it is necessary to gain knowledge of structural changes in different phases, Chapter 5 is dedicated to the structural analysis of morpholinium tetrafluoroborate at its incommensurate phase. Single crystal x-ray diffraction is used for structure determination at T=130 K. The incommensurately modulated structure is solved and refined within a superspace approach (van Smaalen, 2012).

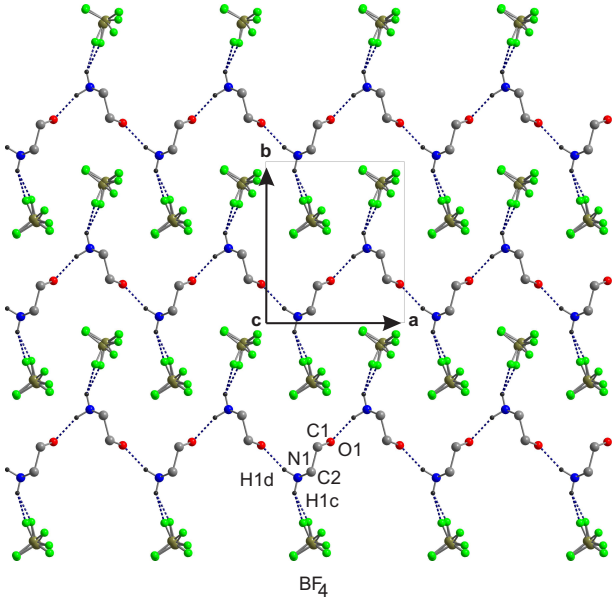

Figure 1.7: Two types of hydrogen bonds, N–H$\cdots$F and N–H$\cdots$O, in morpholinium tetrafluoroborate crystal at T=160 K. Tetrafluoroborate anion is highly disordered with fourfold sites. Experimental details will be discussed in Chapter 5.

Chapter 2

Aperiodic Molecular Crystals

2.1 Periodic versus aperiodic Crystals

A crystal is a solid matter in which a basic motif is repeated regularly along all three dimensions. The translational symmetry can be characterized by the lattice $\Lambda = \{\mathbf{a}_1, \mathbf{a}_2, \mathbf{a}_3\}$ with lattice vectors

$$\mathbf{L} = l_1\mathbf{a}_1 + l_2\mathbf{a}_2 + l_3\mathbf{a}_3. \tag{2.1}$$

Where l_i (i = 1,2,3) are integers. Translational symmetry implies long-range order of the atomic structure. As a consequence, the diffraction pattern exhibits sharp Bragg reflections (Stout and Jensen, 1989). The position of atom μ within the first unit cell is given by its coordinates $[x_1^0(\mu), x_2^0(\mu), x_3^0(\mu)]$ with respect to the basis vectors of the lattice, according to:

$$\mathbf{x}^0(\mu) = x_1^0(\mu)\mathbf{a}_1 + x_2^0(\mu)\mathbf{a}_2 + x_3^0(\mu)\mathbf{a}_3. \tag{2.2}$$

Aperiodic crystals are crystalline materials also with long-range order and in consequence sharp Bragg reflections, but without translational symmetry. The work on incommensurate crystal structures was pioneered by de Wolff (1974). He was able to index the diffraction pattern of anhydrous γ-Na_2CO_3 by four integer indices and he proposed the superspace description for this kind of crystals (de Wolff, 1974). Based on these findings the atomic structures of aperiodic crystals are described today by the so-called superspace theory, as it was developed by de Wolff, Janner and Janssen (1981). Aperiodic crystals are classified in three groups: modulated crystals, incommensurate composite crystals and quasicrystals (van Smaalen, 2012). Modulated

crystals are discussed in detail in the following sections, since, this thesis reports analysis of molecular modulated structures.

2.2 Modulated Structures

In modulated crystals the translational symmetry can be recovered by the superspace approach in higher dimensions (van Smaalen, 2012; de Wolff et al., 1981). A incommensurate structures are then given by modulation functions together with the positions $x^0(\mu)$ of the atoms in the unit cell of basic model for the crystal structure is employed that has translational symmetry in a space with (3+d) dimensions, where d is the number of independent modulated structures, however, are not arbitrary; they follow distinct rules. In other words, the modulated structure is the basic structure with modulation wave vectors. Modulated structures are those structures in which three-dimensional translational symmetry is destroyed. These distortions in periodic distortions. These distortions can mathematically be described by so-called atomic modulation functions. The positions of atoms in structure (Eq. 2.2). Modulated structures are classified in two groups, commensurately and incommensurately modulated structures (Fig. 2.1). Commensurately modulated crystals are superstructures with transitional symmetry. Fig. 2.1.(b) shows a twofold superstructure, which has translational symmetry with periodicity of two times that of the basic cell. The twofold superstructure can be described with a commensurate wave where the displacement of atoms in neighboring unit cells are equal but of opposite direction $\pm\ \mathbf{a}_2$. Therefore, the periodicity of modulation wave is equal to the superlattice period, i.e. $2\mathbf{a}_2$ (Chapter 4 will discuss refinement of a twofold superstructure by describing it as a commensurately modulated structure). If the period of modulation wave does not fit with any integer number of lattice translations, then it is called incommensurate. Periodicity in incommensurate crystals is defined by incommensurate modulation function together with periodic basic cell [Fig. 2.1.(c)] (van Smaalen, 2012).

Three independent modulation functions are required for describing the displacement of each atom from its position in the basic structure toward its position in the superstructure. Modulation functions can be harmonic (continuous) and therefore be expressed by sine/cosine waves or they may be discontinuous, in which case crenel or saw-tooth functions are needed for their description.

Modulation functions are wave functions. The direction and wavelength of the

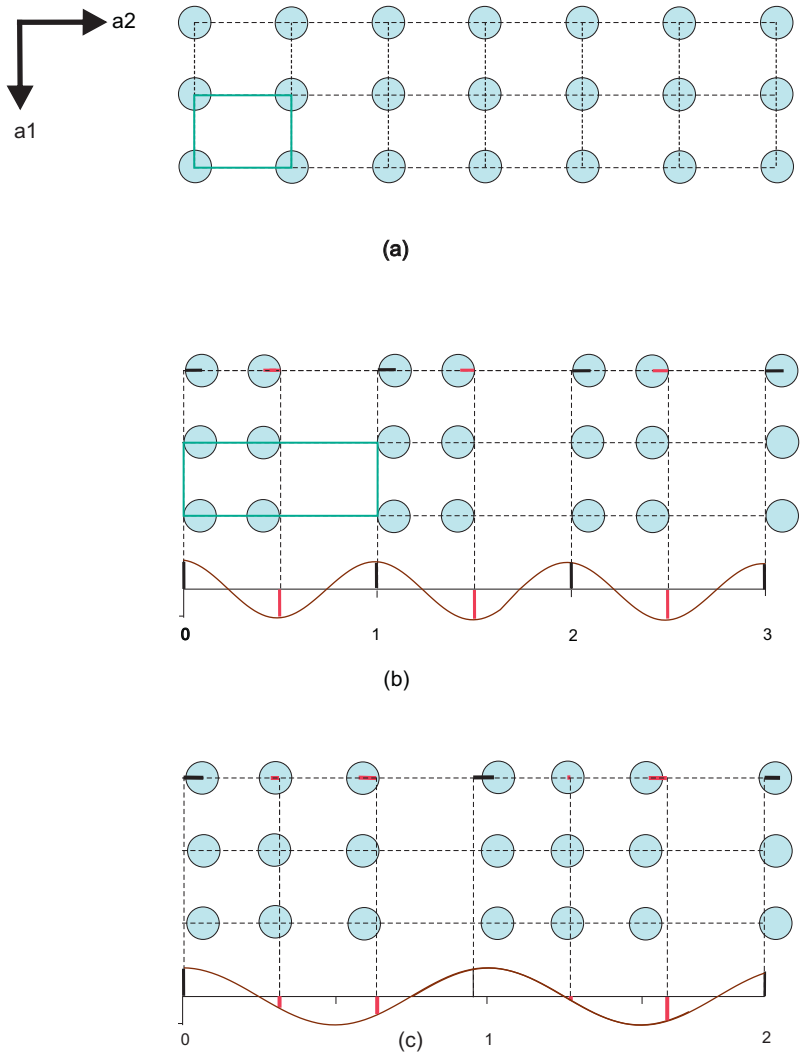

Figure 2.1: (a) Basic crystal structure. (b) Formation of a superstructure with doubled periodicity of basic structure along $\mathbf{a}_2$ axis, represented as commensurate structure with displacement wave. (c) Formation of an incommensurate structure with displacement wave.

wave functions is characterized by a wave vector **q**. Each modulation wave vector can be defined by its components σ_i (i=1,2,3) with respect to the basis vectors of the reciprocal lattice of the basic structure, $\Lambda^* = \{\mathbf{a}_1^*, \mathbf{a}_2^*, \mathbf{a}_3^*\}$, according to:

$$\mathbf{q} = \sigma_1 \mathbf{a}_1^* + \sigma_2 \mathbf{a}_2^* + \sigma_3 \mathbf{a}_3^*. \tag{2.3}$$

If at least one of the components is an irrational number, then the structure is incommensurately modulated.

2.3 Superspace approach

2.3.1 Reciprocal superspace

Diffraction pattern of modulated crystals contain two sets of reflections, main and satellite reflections. The concept of superspace is based on the observation that all Bragg reflections can be indexed by (3+d) integers. Due to the lack of transitional symmetry, all reflections cannot be indexed according a lattice in 3D space. Nevertheless, the main reflections of modulated crystal can be indexed by reciprocal lattice:

$$\Lambda^* = \{\mathbf{a}_1^*, \mathbf{a}_2^*, \mathbf{a}_3^*\}. \tag{2.4}$$

The main reflections are usually strong and they define an average or basic structure with translational symmetry. Deviations from this translational symmetry are reflected in the diffraction pattern by satellite reflections. Satellite reflections cannot be indexed with three small integer numbers. Therefore, depending on the dimension of modulation, one, two, or three additional vectors **q** are required to index all Bragg reflections, i.e. main and satellite reflections. In case of (3+1)D, four integers needed to index all reflections. Therefore, by selecting the fourth vector $\mathbf{a}_4^* = \mathbf{q}$, all reflections can be indexed. Fig. 2.2 exhibits the diffraction pattern of $[C_4H_{10}NO]^+[BF_4]^-$ in its incommensurate phase. It has orthorhombic symmetry, all reflections, including main and satellite reflections, can be indexed with one extra vector $\mathbf{q} = (\sigma_1\ 0\ 0)$ (detailed description provided in Chapter 5). The fourth basis vector can be expressed as:

$$\mathbf{a}_4^* = \sigma_1 \mathbf{a}_1^* + \sigma_2 \mathbf{a}_2^* + \sigma_3 \mathbf{a}_3^*. \tag{2.5}$$

Indeed, $\mathbf{a}_4^*$ in the Eq. 2.5 is the definition of **q** vector (Eq. 2.3).

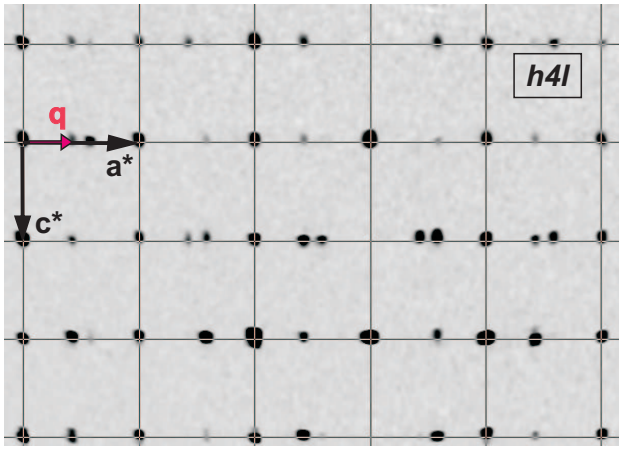

Figure 2.2: Reconstruction of *h4l* layer of reciprocal space of morpholinium tetrafluoroborate in its incommensurate phase, T=130 K. The diffraction pattern exhibits the rectangular reciprocal lattice of main reflections, and first-order satellite reflections of 1D modulation along $\mathbf{a}^*$. All reflections can be indexed with four integers (h, k, l, m) by applying the (3+1)-dimensional superspace approach with additional vector $\mathbf{q} = (\sigma_1\ 0\ 0)$ and $\sigma_1 = 0.4216$. See Chapter 5 for experimental details.

The scattering vectors of Bragg reflections for (3+1)d modulated structures is expresses as in Eq. 2.6 which makes possible to index all reflections by four integer (h_1, h_2, h_3, h_4)

$$\mathbf{H} = h_1\mathbf{a}_1^* + h_2\mathbf{a}_2^* + h_3\mathbf{a}_3^* + h_4\mathbf{a}_4^*. \tag{2.6}$$

As discussed in Section 2.2 incommensurability is identified by the irrational components of the $\mathbf{q}$ vector (at least one out of three components). Experimentally, the incommensurate $\mathbf{q}$ vector varies as a function of temperature, or pressure.

For understanding the superspace approach, the original idea of de Wolff can be followed. The periodicity can be recovered in higher dimensional space by considering that the observed Bragg reflections in 3D space are the projections of Bragg reflections in (3+d)D space. Fig. 2.3 is a schematic representation of the diffraction pattern of one-dimensionally modulated morpholinium tetrafluoroborate along $\mathbf{a}^*$ including main and first-order satellite reflections (compare Fig. 2.2). The positions of observed reflections in real space are the projections of reciprocal lattice vectors in reciprocal superspace. For the projection, an additional vector is required. Vector $\mathbf{b}^*$ introduces the additional superspace dimension which is perpendicular to real space (or physical space). Hence, the reciprocal superspace vectors includes three

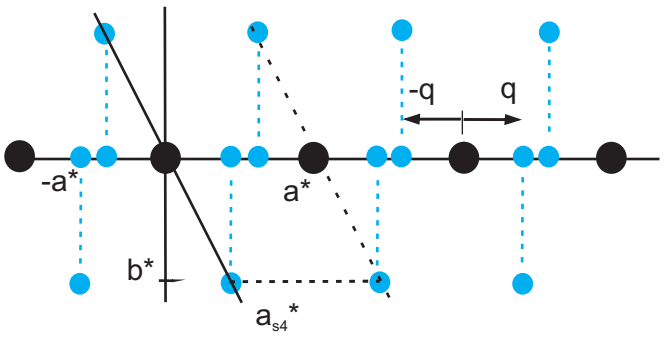

Figure 2.3: Schematic drawing of diffraction pattern for one-dimensionally modulated crystal of morpholinium tetrafluoroborate exhibiting the (3+1)D superspace approach along the reciprocal lattice line $\mathbf{a}^*$ including the main reflections (black circles) and satellites (blue circles). The superspace reciprocal lattice is represented in black dashed lines. The reciprocal lattice points in superspace are projected onto reflection positions in 3D space (physical space) by blue dashed lines.

reciprocal basis vectors in 3D space with components zero along the additional dimensions, together with the additional vectors with components $\mathbf{q}$ along real space and $\mathbf{b}^*$ along the additional space (van Smaalen, 2004; 2012). If we define the reciprocal basis vectors in 3D as $\mathbf{a}_i^*$, the superspace reciprocal vectors $\mathbf{a}_{si}^*$ are (van Smaalen, 2012):

$$\Sigma^* : \begin{cases} \mathbf{a}_{si}^* = (\mathbf{a}_i^*, 0) & i = 1, 2, 3 \\ \mathbf{a}_{s4}^* = (\mathbf{a}_4^*, \mathbf{b}^*). \end{cases} \tag{2.7}$$

2.3.2 Direct superspace

Similar to 3D periodic structures, the inverse Fourier transform of the phased diffraction pattern results in the crystal structure, that is periodic in direct superspace. The direct-lattice basis vectors related to Σ^* are (van Smaalen, 2012):

$$\Sigma : \begin{cases} \mathbf{a}_{si} = (\mathbf{a}_i, -\sigma_i \mathbf{b}) & i = 1, 2, 3 \\ \mathbf{a}_{s4} = (0, \mathbf{b}). \end{cases} \tag{2.8}$$

The relation between direct and reciprocal lattice vectors in 3D space is applicable for superspace as well (van Smaalen, 2012):

$$\mathbf{a}_{sk}^* \cdot \mathbf{a}_{sk'} = \delta_{kk'} \tag{2.9}$$

If k = k′ then $\delta_{kk'} = 1$ and otherwise zero. A fourth coordinate axis, **b**, is introduced perpendicular to physical space. Vector **b** is dimensionless, with arbitrary length. It is parallel to the reciprocal basis vector $\mathbf{b}^*$, and its length defined by b^*b =1. Coordinates (x_{s1}, x_{s2}, x_{s3}, x_{s4}) in direct superspace are defined relative to Σ as:

$$\mathbf{x}_s = x_{s1}\mathbf{a}_{s1} + x_{s2}\mathbf{a}_{s2} + x_{s3}\mathbf{a}_{s3} + x_{s4}\mathbf{a}_{s4}. \tag{2.10}$$

The superspace coordinates of a atom in direct space are obtained by :

$$\begin{aligned} x_{si} &= x_i \qquad\qquad i = 1, 2, 3 \\ x_{s4} &= \mathbf{q} \cdot \mathbf{x}. \end{aligned} \tag{2.11}$$

Where **x**= (x_1, x_2, x_3) are the coordinates in physical space with respect to the basic structure lattice, Λ. The coordinates of a point which is located outside of physical space, are obtained by adding the value of distance between the point and physical space to the $\mathbf{q} \cdot \mathbf{x}$ term. This distance defines a new parameter t (Fig. 2.4).

$$x_{s4} = t + \mathbf{q} \cdot \mathbf{x}. \tag{2.12}$$

A cut in fourth dimension axis ($\mathbf{a}_{s4}$) parallel to physical space defines a t section. Physical space is recovered at t=0. The superspace coordinates of the basic structure position of an atom are defined as:

$$\bar{x}_{s4} = \bar{x}_4 = t + \mathbf{q} \cdot \bar{\mathbf{x}}. \tag{2.13}$$

$\bar{x}_4$ is equal to the fourth superspace coordinate. If all atoms with non-periodic arrangement in 3D space (physical space, the cut at t=0) are translated to a direct superspace unit cell by application of the translations Σ (Eq. 2.8), the translated atoms will form a dense set of points with a wavy shape. This wavy line is shape of atomic modulation function. Modulation functions are wave functions with period of one. Hence, the parameter t is called phase of modulation with a value between 0 to 1 [Fig. 2.4(c)]. t has an important role in the crystal-chemical analysis of aperiodic crystals. The argument $\bar{x}_4$ in Eq. 2.13 appears in wave functions $\mathbf{u}(\bar{x}_4)$ of atom μ. As discussed in Section 2.1 modulation wave functions are defined in three directions as :

$$\mathbf{u}^{\mu}(\bar{x}_4) = u_1^{\mu}(\bar{x}_4)\mathbf{a}_1 + u_2^{\mu}(\bar{x}_4)\mathbf{a}_2 + u_3^{\mu}(\bar{x}_4)\mathbf{a}_3. \tag{2.14}$$

The basic position is defined by $\bar{\mathbf{x}}$

$$\bar{\mathbf{x}} = \bar{x}_1\mathbf{a}_1 + \bar{x}_2\mathbf{a}_2 + \bar{x}_3\mathbf{a}_3 \tag{2.15}$$

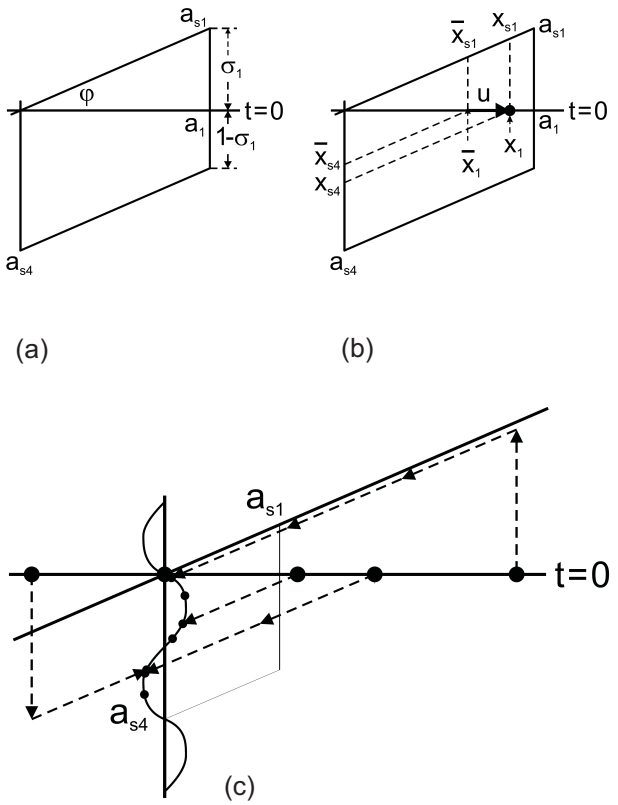

Figure 2.4: (a) Unit cell of the direct superspace lattice with intersection along $\mathbf{a}_1$ at 3D space (i.e. t=0). The angle ϕ (sin(ϕ)= (σ_1 a_{s4}/a_{s1})) defines the direction of $\mathbf{a}_{s1}$ (reprinted of Fig. 7. from van Smaalen (2004)). (b) The coordinates of one atom at its basic position ($\bar{x}_{s1}$,$\bar{x}_{s4}$) with respect to Σ in superspace and $\bar{x}_1$ with respect to Λ in 3D space. The atom shifted from its basic position by vector $\mathbf{u}$ (reprinted of Fig. 7. from van Smaalen (2004)). (c) Translation of atoms in 3D space towards the first unit cell (reprinted of Fig. 8. from van Smaalen (2004)).

The position of atom μ with basic position of $\bar{\mathbf{x}}$ in the crystal is given by

$$\mathbf{x}_i^{\mu} = \bar{\mathbf{x}^{\mu}} + \mathbf{u}^{\mu}(\bar{x}_4). \tag{2.16}$$

Any periodic function can be written as a Fourier series, which can be a continuous modulation function:

$$u_i^{\mu}(\bar{x}_4) = \sum_{n=1}^{\infty} A_i^n(\mu)\sin(2\pi n\bar{x}_4) + B_i^n(\mu)\cos(2\pi n\bar{x}_4). \tag{2.17}$$

$\mathbf{A}_i^n(\mu)$ and $\mathbf{B}_i^n(\mu)$, (i = 1,2,3), define the six independent coefficients for atom μ in three directions of space. The order of harmonics is defined by n.

2.4 Aperiodic molecular compounds

The majority of modulated structures that have been analyzed are materials not composed of individual molecules, but extended solids such as metals, alloys, ceramics. The present thesis focuses on incommensurately modulated molecular crystals. The origin of the modulation and the possible ways how they can be analyzed differs from metallic or ionic compounds (Schönleber, 2011; van Smaalen, 2012; Wagner and Schönleber, 2009). For molecules and molecular ions the conformation of the entity as a whole has to be taken into account. In metallic or ionic solids, atoms are to a certain degree free to move independently within the lattice. The covalent bonds within a molecular entity drastically limit this kind of movement, and large parts of molecules have a predetermined shape that cannot be altered. This character gives the opportunity to employ rigid bodies for molecular fragments. On the other hand, non-covalent interactions have great effects on crystal packing and the modulation of molecular compounds.

A well known example of an organic incommensurately modulated compound is biphenyl, Fig. 2.5 (Baudour and Sanquer, 1983; Dzyabchenko and Scheraga, 2004). The dihedral angle between two phenyl rings widely varies depending on the environment. In the gas phase the stable conformer is at dihedral angle 44.4° (Bastiansen and Samdal, 1985). In solution dihedral angle is ranging from 19 to 32° depending on the intermolecular interactions between neighboring molecules and π–π interactions between neighboring phenyl rings (Eaton and Steele, 1973).

In the solid state the crystal behaves interesting as temperature varies. X-ray studies has been done at different temperatures. At room temperature the two rings

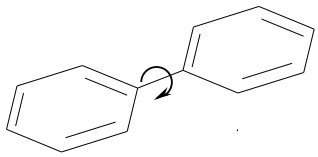

Figure 2.5: Molecular structure of biphenyl. The main modulation is a result of torsion of the C–C bond between two rigid phenyl rings.

are coplanar, i.e the torsion angle is 0°. The observed planar structure is in fact the statistical average of two alternately twisted conformations (Charbonneau and Delugeard, 1977). Hence, the crystal symmetry belongs to centrosymmetric space group $P2_1/a$. This symmetry has been reported for the crystal structure at higher temperatures in phase I, at T= 110 to 298 K (Charbonneau and Delugeard, 1976), (Charbonneau and Delugeard, 1977).

The two low temperature phases of biphenyl were found to be incommensurate. At lower temperatures molecules take one of the two conformers with different torsion angles in an alternating ordered manner. The first phase transition happens at 40 K (phase II). In phase II, due to the constrained torsional angles in the incommensurate molecules, thus, the crystal loses the inversion symmetry with doubled length of the longest axis of the unit cell in HT. The dihedral angles observed in the low temperature varying between ± 10° (phase II) (Atake and Chihara, 1980). Further cooling lead to second phase transition at 20 K (phase III) that is also incommensurately modulated. The dihedral angle are close to ± 11°. The origin of the modulation was shown to be a result of an competition between the intramolecular forces favouring nonzero torsion angle and the crystal packing effects (Dzyabchenko and Scheraga, 2004). The incommensurate crystal structure of (6R,7aS)-6-(tert-butyl-dimethylsilanyloxy)-1-hydroxy-2-phenyl-5,6,7,7a tetrahydropyrrolizin-3-one has been successfully refined in superspace using a rigid body approach (Wagner and Schönleber, 2009). Three individual molecular fragments each act as rigid units, while the overall shape of the molecule varies significantly with the phase of the modulation.

Recently the incommensurate crystal structurer of adamantan-1-ammonium 4-fluorobenzoate was reported (Schönleber et al., 2014). The modulation for this molecule was described not only by displacements of atoms, but also by varying

orientations of three rigid fragments: the adamantan-1-ammonium cation, the fluorophenyl, and the carboxylate group (Schönleber et al., 2014).

In this thesis two modulated molecular crystals will be presented: the commensurate and incommensurate phase of the co-crystal of phenazine and chloranilic acid (Chapters 4 and 3) and the incommensurately modulated structure of crystals of morpholinium tetrafluoroborate (Chapter 5).

2.4.1 Rigid bodies and local symmetries for molecules

Different parameters in crystal structures can be modulated. They include positions of atoms, site occupancy, and atomic displacement parameters (ADPs). Each harmonic modulation function (Eq. 2.17) includes for each atom in the basic-structure, six parameters of displacive modulation, two for occupancy modulation, and twelve parameters for modulation of ADPs. In Chapters 4 and 3, harmonic modulation functions are applied to the coordinates and ADPs for each individual atom in the unit cell. Alternatively, modulation functions can be applied to a group of atoms rather than individual atoms (Section 2.4). This method is called the rigid body approach. The rigid body approach was introduced for incommensurately modulated molecular structures by Petricek et al. (1985). A group of atoms in a molecule with a rigid covalently bonded framework, can be treated as rigid body, e.g. a benzene ring. A so-called pseudo-rigid body approach can be used for groups of atoms where the internal structure is also varied in the refinement. Degrees of freedom can be reduced by application of the local symmetry for the pseudo-rigid body. Any of the thirty two crystallographic point groups and any non-crystallographic point group can be used for definition of local symmetry. For example, a sixfold orientationally disordered nitrate group is defined as a rigid group in Λ-cobalt(III) sepulchrate trinitrate (Schönleber et al., 2010). The local symmetry 32 (Schönflies, D_3) is applied for planar molecule of NO_3 group, which improves the crystal structure model. Also, this approach can be generalized for molecules which is consist of non-rigid groups. The refinement of both standard and incommensurate crystal structures of morpholinium tetrafluoroborate (Chapter 5) are examples where a fourfold disordered tetrafluoroborate is defined as non-rigid group.

Jana2006 (Petricek et al., 2014) is not only a software that is suitable for modulated crystal structure analysis but also it makes possible for refining the molecular structures within rigid bodies approach.

The dynamics of a rigid body, *rb*, in which all interatomic distance and bond

lengths are fixed constraints is an excellent approximation, although, this is an idealization which ignores elastic and plastic deformations of real body. In fact it reduces the number of parameters of all constituent atoms to one body with six degrees of freedom. The possible motions which leave the interatomic distances fixed are combinations of:

(a) translations of the body as a whole, $rb \rightarrow rb + \mathbf{T}$

(b) rotations of the body about a fixed point, k.

Describing the translations can be specified by giving the coordinates of the fixed point, k, in the body. Often k is center of mass or one particular atom belonging to the body. In order to discuss other atoms forming the pseudo-rigid body, we will use an orthonormal coordinate system fixed in body, known as body coordinates with the origin fixed in k. The constraints mean that the position of each atom of the body $\mathrm{x}^0(\mu)$, has fixed coordinates of in terms of this coordinate system. Thus the configuration of the body in the crystal is completely specified by $\mathrm{x}^0(\mathrm{k};\mu)$ toghether with a rotation $\mathbf{R}(k)$ and translation $\mathbf{T}$:

$$\mathbf{x}^0(\mu) = [\mathbf{R}(k) \times \mathbf{x}^0(k;\mu))] + \mathbf{T}(k) \tag{2.18}$$

As discussed the displacement of atoms involved in molecular fragments are not determined by each individual atom location, but by a point common to all atoms in molecular fragment. Therefore, modulation of molecular crystal affect entire rigid body and modulation functions can be used for it. The coordinates, $\mathrm{x}^0(\mathrm{k})$, are introduced for the center or reference point of rigid body k, if the rotation is done about the origin of coordinate system, then it would be equal to the translation.

$$\mathbf{x}^0(k) = \mathbf{T} \tag{2.19}$$

Displacive modulations are described by two modulation functions (van Smaalen, 2012): a vector function, $\mathbf{u}_T^k[\bar{x}_{s4}(k)]$, for modulation of translations and axial vector function, $\mathbf{u}_R^k[\bar{x}_{s4}(k)]$, for describing the modulation of the rotations.

$$\mathbf{u}^\mu[\bar{x}_{s4}(\mu)] = \mathbf{u}_T^k[\bar{x}_{s4}(k)] + \mathbf{u}_R^k[\bar{x}_{s4}(k)] \times \mathbf{x}^0(k;\mu)]. \tag{2.20}$$

Modulation function of rigid body are a function of Eq. 2.13

$$\bar{x}_{s4}(k) = t + \mathbf{q} \cdot [\mathbf{L} + \mathbf{x}^0(k)]. \tag{2.21}$$

Although thermal motion does not effect the internal structure of rigid body, they might be refined for whole the molecule as TLS parameters that stands for

Translation-Libration-Screw formalism (Schomaker and Trueblood, 1968). The TLS parameters can be employed as an independent parameters instead of the temperature parameters of individual atoms. Similar to the individual atoms, in addition to the molecular modulated displacement parameters (i.e. rotation and translation parameters) TLS thermal parameters can be modulated. Modulation functions are applied for whole the molecule within the TLS formalism.

Other parameters in the model molecule include occupancy. Occupancy of molecular orientations also can be modulated. The modulation of the occupational probabilities that are described by harmonic modulation functions is given by:

$$p^{\mu}(\bar{x}_{s4}) = P^{0}(\mu) + \sum_{n=1}^{\infty}[P^{sn}(\mu)\sin(2\pi n\bar{x}_{s4}(k)) + P^{cn}(\mu)\cos(2\pi n\bar{x}_{s4}(k))]. \quad (2.22)$$

Average occupation probabilities of the molecule is $\mathrm{P}^{0}(\mu)$ and modulation function $\mathrm{p}^{\mu}(\bar{x}_{s4})$ are occupation in the nth cell with Fourier coefficients of $P^{sn}(\mu)$ and $P^{cn}(\mu)$. The order of harmonics is given by n.

Full site occupancies are required for all values of t in $\bar{x}_{s4} = \mathrm{t} + \mathbf{q}\cdot\,\mathbf{x}^{0}(\mu)$ leading to the condition:

$$\sum_{\mu=1}^{N_{site}} p^{\mu}[t + \mathbf{q}\cdot\mathbf{x}^{0}(\mu)] = 1. \quad (2.23)$$

The calculated probabilities of different sites of the molecule versus phase of modulation, t which is shown in Fig. 5.3 fulfils the condition of Eq. 2.23.

Chapter 3

Resonance-stabilized partial proton transfer in hydrogen bonds of incommensurate Phenazine–chloroanilic acid [1]

3.1 Introduction

Organic compounds are of interest as ferroelectric materials, because they have a low specific weight and they are potentially cheap to produce (Horiuchi and Tokura, 2008). Furthermore, organic compounds offer more possibilities than inorganic compounds for designing properties. Organic materials based on hydrogen-bonded supramolecular chains with a polar space group form one class of ferroelectric materials. The co-crystal of phenazine (Phz) and 2,5-dichloro-3,6-dihydroxy-*p*-benzoquinone (chloranilic acid, H_2ca) is one of several recently discovered hydrogen-bonded organic ferroelectrics (Horiuchi, Ishii, Kumai, Okimoto, Tachibana, Nagaosa and Tokura, 2005; Horiuchi et al., 2009; Kumai et al., 2012; 2006).

Phz-H_2ca contains chains of alternating Phz and H_2ca molecules connected through O–H$\cdots$N intermolecular hydrogen bonds. At room temperature, all hydrogen bonds are equivalent by the symmetry of the centrosymmetric space group $P2_1/n$ ($Z = 2$), and the crystal of Phz-H_2ca is paraelectric (PE phase) (Horiuchi, Ishii, Kumai, Oki-

[1] This chapter has been published as: Leila Noohinejad, Swastik Mondal, Sk Imran Ali, Somnath Dey, Sander van Smaalen and Andreas Schönleber: Resonance-stabilized partial proton transfer in hydrogen bonds of incommensurate Phenazine–chloroanilic acid; *Acta Cryst.* *B*, **71**: 228- 234 (2015)

moto, Tachibana, Nagaosa and Tokura, 2005; Kumai et al., 2007). Below $T_c^I = 253$ K the symmetry is reduced to $P2_1$ ($Z = 2$), allowing for two inequivalent hydrogen bonds. One of the two bonds exhibits partial proton transfer, which is responsible for the spontaneous polarization (FE-I phase) (Horiuchi, Ishii, Kumai, Okimoto, Tachibana, Nagaosa and Tokura, 2005; Kumai et al., 2007; Gotoh et al., 2007). Phz-H_2ca has an incommensurately modulated structure between $T_c^{IC} = 147$ K and $T_c^{II} = 137$ K (FE-IC phase) (Saito et al., 2006; Horiuchi et al., 2009). Below T_c^{II} another ferroelectric phase is stable, that can be characterized as a twofold superstructure of the room-temperature structure (FE-II phase) (Noohinejad et al., 2014).

Here we report the crystal structure of the incommensurate phase, employing the superspace formalism applied to single-crystal X-ray diffraction data. The modulation is found to mainly affect the positions of the hydrogen atoms within the O–H$\cdots$N intermolecular hydrogen bonds. Evidence for proton transfer in part of these bonds is provided by the correlated variations of bond lengths reflecting resonance stabilization of the anion. A detailed comparison of the various phases reveals that the incommensurate phase has a crystal structure intermediate between the crystal structures of the FE-I and FE-II phases. A mechanism is proposed for the sequence of phase transitions.

3.2 Experimental

3.2.1 X-ray diffraction

Single crystals of Phz-H_2ca were obtained by cosublimation of phenazine and chloranilic acid (Horiuchi, Ishii, Kumai, Okimoto, Tachibana, Nagaosa and Tokura, 2005; Noohinejad et al., 2014). A diffraction experiment at $T = 139$ K was performed on the same crystal as was employed in our previous study on the commensurate FE-II phase (Noohinejad et al., 2014). X-ray diffraction data have been measured at beamline F1 of Hasylab at DESY in Hamburg, Germany, employing a MAR165 CCD detector mounted on a kappa diffractomter. The temperature of the crystal was regulated by a nitrogen gas-flow cryostat. X-ray diffraction data were collected by φ scans and ω scans for various settings of the orientation of the crystal. To better evaluate strong and weak reflections, two measurements were performed with the same measurement strategies but with different exposure times of 20 and 160 seconds, respectively. Data processing of the measured images has been done with the software Eval15 for indexing and extraction of integrated intensities of

Bragg reflections (Schreurs et al., 2010), and with SADABS for absorption correction (Sheldrick, 2008). The latter employed groups of equivalent reflections defined according to the point group $2/m$, which appeared as symmetry of the diffraction. Experimental details are given in Table 5.1.

Indexing of the diffraction images with EVAL15 resulted in an indexing with four integers on the basis of a monoclinic unit cell closely related to the unit cell of the FE-I phase at 160 K (Horiuchi, Ishii, Kumai, Okimoto, Tachibana, Nagaosa and Tokura, 2005) together with the incommensurate modulation wave vector $\mathbf{q}'$ = ($\frac{1}{2}$, $\sigma_2{}'$, $\frac{1}{2}$), where $\sigma_2{}' = 0.4861$. However, the integration routine of EVAL15 did not accept a modulation wave vector with rational components. Therefore, the integration has been performed within the supercentered setting with $\mathbf{q}_i' = (0, \sigma_2{}', 0)$ and centering translation ($\frac{1}{2}$, 0, $\frac{1}{2}$, $\frac{1}{2}$) with respect to the transformed basic-structure unit cell $\mathbf{A} = \mathbf{a} - \mathbf{c}$, $\mathbf{B} = \mathbf{b}$, and $\mathbf{C} = \mathbf{a} + \mathbf{c}$ (Stokes et al., 2011). The same setting has been employed in SADABS.

3.2.2 Choice of the superspace group

The low-temperature superstructure of the FE-II phase at 100 K has been described as a commensurately modulated structure with a basic structure similar to the structure at higher temperatures and the commensurate modulation wave vector $\mathbf{q}_{comm}$ = ($\frac{1}{2}$, $\frac{1}{2}$, $\frac{1}{2}$). The superspace group $P2_1(\frac{1}{2}\,\sigma_2\,\frac{1}{2})0$, with $\sigma_2 = \frac{1}{2}$ has been found to describe the symmetry of this phase (Noohinejad et al., 2014).

Presently, the indexing with modulation wave vector $\mathbf{q}'$ = ($\frac{1}{2}$, $\sigma_2{}'$, $\frac{1}{2}$) and $\sigma_2{}' = 0.4861$ (see Section 3.2.1) leads to the superspace group $P2_1(\frac{1}{2}\,\sigma_2{}'\,\frac{1}{2})s$. The acentric superspace group is established by the lack of inversion symmetry of both the FE-I and FE-II phases (see the *Introduction*) as well as by measurements of the electrical polarization, indicating a ferroelectric state below T_c^I (Horiuchi et al., 2009). The two superspace groups appear to be alternate settings of superspace group No. 4.1.6.3 with standard setting $P2_1(\frac{1}{2}\,0\,\sigma_3)0$ (Stokes et al., 2011). The two settings can be transformed into each other by a shift of the origin. However, this would result in different coordinates of the atoms in the basic structures of the low-temperature and incommensurate phases, which is not desired. The setting with zero intrinsic translation along the fourth coordinate can also be obtained by the choice of a different modulation wave vector for the incommensurate modulation, according to

$$\begin{aligned} \mathbf{q} &= \mathbf{a}^* + \mathbf{b}^* + \mathbf{c}^* - \mathbf{q}' \\ &= (\tfrac{1}{2},\ \sigma_2,\ \tfrac{1}{2}) \end{aligned} \tag{3.1}$$

Table 3.1: Crystal data and refinement details for model A

Temperature (K)	139
Chemical formula	$C_{18}Cl_2H_{10}O_4N_2$
Formula weight	389.19
Superspace	$P2_1(1/2\,\sigma_2\,1/2)0$
q	(1/2, 0.5139, 1/2)
a (Å)	12.372 (2)
b (Å)	3.7649 (5)
c (Å)	16.8315 (2)
β (°)	107.789 (7)
V (Å^3)	746.52 (14)
Z	2
Crystal size (mm^3)	$0.22 \times 0.125 \times 0.05$
Crystal color	Dark brown
Crystal form	Platelet
Radiation type	Synchrotron
Wavelength (Å)	0.5600
Scan mode	ω and ϕ
Theta range (deg)	1.92 to 33.33
Range of h	-16 to 16
Range of k	-7 to 7
Range of l	0 to 33
Range of m	-1 to 1
μ (mm^{-1})	0.243
Absorption corr.	empirical
T_{min}, T_{max}	0.7769, 0.9910
No. of reflections	
Measured	25001
Independent	15433
Observed	8092
Main (obs, all)	5607, 5942
Satellites, 1st order (obs, all)	2485, 9491
$R_{int}(obs, all)$	1.85, 1.94
Criterion for observed reflection	$I > 3\sigma(I)$
Refinement, Software	on F, JANA2006
Weighting scheme	$1/(\sigma(F)^2 + (0.01F_{obs})^2)$
GOF^{obs},GOF^{all}	2.78, 2.08
R_F^{obs}, R_F^{all} (all)	0.0449, 0.0720
R_F^{obs}, R_F^{all} (main)	0.0411, 0.0425
R_F^{obs}, R_F^{all} (sat)	0.1268, 0.3661
No. of parameters	719
$\Delta\rho_{max}$, $\Delta\rho_{min}$ (e Å^{-3})	0.63, -0.55

with

$$\sigma_2 \;=\; 1 - \sigma_2{}' \;=\; 0.5139 \tag{3.2}$$

Diffraction data were re-indexed according to this transformation (Eqs. 3.1 and 3.2), and the superspace group $P2_1(\frac{1}{2}\,\sigma_2\,\frac{1}{2})0$ with $\sigma_2 = 0.5139$ has been used for all refinements.

3.2.3 Structure refinements

Initial values for the parameters of the basic structure have been taken from the basic structure at 100 K (Noohinejad et al., 2014). Anisotropic atomic displacement parameters (ADPs) have been used for all non-hydrogen atoms. Hydrogen atoms were placed at calculated positions with a bond length d(C–H) of 0.96 Å, and they were refined using a riding model with isotropic ADPs equal to 1.2 times the equivalent isotropic ADPs of the bonded carbon atoms. Hydrogen atoms of the hydroxyl groups were located in the difference Fourier map. They were then shifted to positions fulfilling the restraints d(O–H) = 0.85 (2) Å and $\angle$(C–O–H) = 109.5 (2.0)° (Müller et al., 2005; Engh and Huber, 1991), while their isotropic ADPs were restricted to 1.5 times the equivalent isotropic ADPs of the adjacent oxygen atoms. Employing Jana2006 (Petricek et al., 2014), the positions of all atoms were refined with these restraints in effect. In the last step the restraints were released, resulting in a good fit to the main reflections with $R_{obs} = 0.0412$.

Three approaches have been chosen for determination of the atomic modulation functions for the incommensurate phase. In one approach, the modulation functions of the model at 100 K (Noohinejad et al., 2014) were used as starting model. The same superspace group was employed, but with $\sigma_2 = 0.5139$ instead of the commensurate value of 0.5. The refinement converged smoothly to a good fit to the combined set of main and satellite reflections, resulting in model A (Table 5.1). Model A involves one harmonic wave for the displacive modulation of all atoms as well as one harmonic wave for the modulation of ADPs of all non-hydrogen atoms. The origin was fixed on the Cl2 atom. Inversion twins are expected to be present, because the IC phase has been reached by phase transitions, starting with the centrosymmetric PE phase at room temperature. Twinning did have a marginal effect on the refinement, while a significant deviation from equal volume fractions of the twin domains was not found. Therefore, equal volume fractions were employed for the final refinements. A model with the alternative symmetry $P2_1(\frac{1}{2}\,\sigma_2\,\frac{1}{2})s$ did not lead to a good fit to the data.

Table 3.2: R values for the different structure models. Included are R values and partial R values for observed (obs; defined by $I > 3\sigma_I$) and all (all) reflections.

Model	A	B	C
GOF^{obs}	2.78	2.78	2.79
R_F^{obs} (all)	0.0449	0.0449	0.0451
R_F^{obs} (main)	0.0411	0.0412	0.0411
R_F^{obs} (sat)	0.1268	0.1266	0.1301
GOF^{all}	2.08	2.08	2.08
R_F^{all} (all)	0.0720	0.0718	0.0720
R_F^{all} (main)	0.0425	0.0425	0.0425
R_F^{all} (sat)	0.3661	0.3634	0.3663
No. of parameters	719	719	719

Starting with the same basic structure, model B was developed by assigning arbitrary but small values to the modulation parameters of the heaviest atom (chlorine). Refinements alternated with the subsequent introduction of modulation parameters for the O, N, C and H atoms, finally resulting in a fit to the diffraction data of equal quality as that of model A (Table 3.2).

In a completely different approach, charge-flipping was applied for the direct solution of the incommensurately modulated structure in superspace (Palatinus, 2013; Palatinus and Chapuis, 2007). For the solution, the software SUPERFLIP suggested the centrosymmetric symmetry $P2_1/n(\frac{1}{2}\,\sigma_2\,\frac{1}{2})00$. Since we knew that the modulation is non-centrosymmetric, we have chosen the superspace group $P2_1(\frac{1}{2}\,\sigma_2\,\frac{1}{2})0$. JANA2006 was subsequently used to extract the basic-structure positions and values of the first-order harmonics of the displacive modulation functions for all non-hydrogen atoms. Atoms were then named to match Fig. 3.1. For this model the basic-structure coordinates were refined against all reflections, resulting in $R_F = 0.3046$, $R_F^{main} = 0.2901$ and $R_F^{sat} = 0.6184$. Hydrogen atoms were added at calculated positions near carbon atoms as in model A. Refinement of the atomic coordinates within the riding model resulted in $R_F = 0.3037$, $R_F^{main} = 0.2892$ and $R_F^{sat} = 0.6174$. Subsequent refinement of anisotropic ADPs of the non-hydrogen atoms resulted in $R_F = 0.0680$, $R_F^{main} = 0.0430$ and $R_F^{sat} = 0.6081$. Hydrogen atoms of the hydroxyl groups were located in the difference Fourier map and treated like in model A. Refinement of the restrained model gave $R_F = 0.0672$, $R_F^{main} = 0.0427$

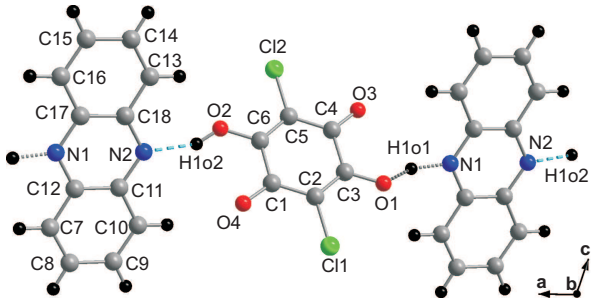

Figure 3.1: Phenazine $C_{12}H_8N_2$ and chloranilic acid $C_6Cl_2H_2O_4$ with the atom labels as employed in the present work.

and $R_F^{sat} = 0.5993$. Refinement of the free model gave $R_F = 0.0666$, $R_F^{main} = 0.0420$ and $R_F^{sat} = 0.5998$. Small values were applied to the displacive modulation functions of the hydrogen atoms. Refinement of the modulated structure resulted in $R_F = 0.0472$, $R_F^{main} = 0.0412$ and $R_F^{sat} = 0.1787$. Finally, modulation parameters were introduced for the ADPs of the non-hydrogen atoms, resulting in the final fit of model C to the diffraction data as given in Table 3.2.

3.3 Discussion

3.3.1 The structure model

The final fit to the diffraction data is excellent for the main reflections (Table 5.1). The rather high value of $R_F^{obs}(\text{sat}) = 0.127$ can completely be explained by the weakness of the satellite reflections and the resulting values for $R_\sigma(\text{sat}) = 0.151$, representing the average standard uncertainty over intensity, and $R_{int}(\text{sat}) = 0.129$ for averaging satellite reflections.

Model A and model B give the same fit to the diffraction data (Table 3.2). Although modulation parameters are different, these two models are completely equivalent. They differ from each other by a phase shift (Fig. 3.2). Further support for model A comes from difference Fourier maps obtained after refinements of model A and of a similar model without the acidic hydrogen atoms (see Supporting Information). Model C has been obtained by solving the modulated structure by charge flipping in superspace. The modulation of model C is different from the modulations in models A and B, but $R_F^{obs}(\text{sat})$ is clearly higher for model C than for the other two models (Table 3.2). Therefore, model C provides a less good description

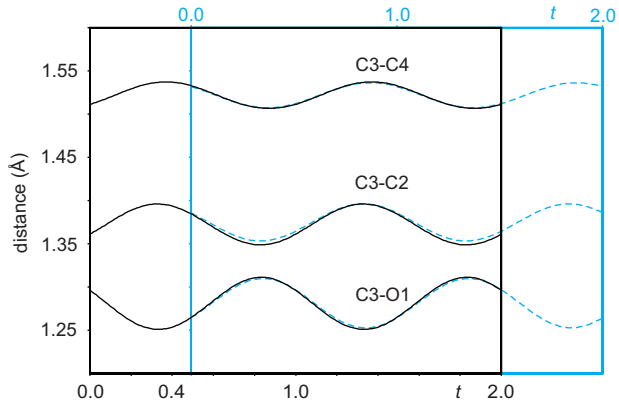

Figure 3.2: Interatomic distances (Å) as a function of the phase t of the modulation. The t plot for model B (in blue) is superimposed onto the t plot for model A (in black), after application of a phase shift of -0.5139 in t to model B.

of the modulation than models A and B do. Difficulties in obtaining the correct structure model by charge flipping are probably related to the pseudo-symmetry of the structure, with deviations from inversion symmetry being mainly the result of rearrangements of hydrogen atoms.

These properties give strong support that model A (as well as the equivalent model B) is the correct model for the modulated crystal structure of the incommensurate phase. In view of these results, we have restricted the analysis to model A.

3.3.2 Resonance-stabilized proton transfer

The modulated structure of the incommensurate phase of Phz-H_2ca has been successfully determined at a temperature of 139 K. The magnitudes of the modulation amplitudes of the atoms reveal that the major effect of the modulation is a displacive modulation of the hydrogen atom of one of the two hydrogen bonds in which each molecule is involved in. This feature is in complete agreement with the crystal structures of the FE-I and FE-II phases, where also one half of the hydrogen bonds is involved in the distortions of the structure.

More precisely, the crystal structure of the FE-I phase contains one crystallographically independent molecule H_2ca with two independent oxygen atoms involved in O–H$\cdots$N hydrogen bonds, denoted by O1 and O2 (Gotoh et al., 2007). The basic structure of the FE-IC phase is the same as the crystal structure of the FE-I

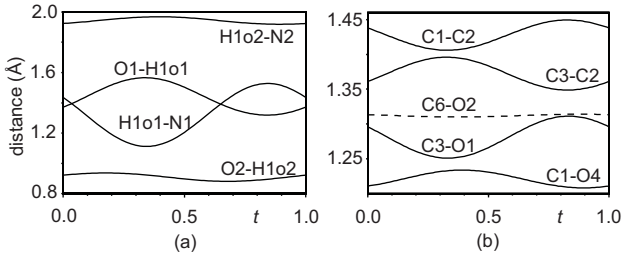

Figure 3.3: Selected interatomic distances (Å) as a function of the phase t of the modulation. (a) The O–H and N–H distances within the two hydrogen bonds. (b) C–C and C–O distances of the resonance system stabilizing the Hca^- anion, as well as the C6–O2 distance not involved in resonance. Notice the different length scale on the vertical axes for panels (a) and (b).

phase, so that the FE-IC phase contains modulated atoms O1 and O2. Finally, the FE-II phase represents a twofold superstructure of the structure of the FE-I phase. Together with a reduction of the point symmetry to triclinic, this results in four crystallographically independent molecules H_2ca with atoms O1A through O1D derived from O1, and atoms O2A through O2D derived from O2 (Noohinejad et al., 2014). In all three phases, the hydrogen bonds O2–H1o2$\cdots$N2 are not involved in superstructure formation. For the FE-IC structure, Table 3.3 and Fig. 3.3(a) show that bond lengths involving the O2, H1o2 and N2 atoms exhibit only a weak dependence on the phase t of the modulation. For the FE-I and FE-II structures this property has been previously determined by (Gotoh et al., 2007) and (Noohinejad et al., 2014), and it is summarized in Table 3.3. Therefore, the hydrogen bonds O2–H1o2$\cdots$N2 do not play a direct role in the ferroelectricity of this compound.

The largest variation of bond lengths within the FE-IC phase is found for the hydrogen bond O1–H1o1$\cdots$N1, with a variation of Δd(O1–H1o1) = 0.25 Å and Δd(N1–H1o1) = 0.42 Å (Table 3.3). All other bonds are much less affected by the modulation, with a maximum variation of 0.06 Å for C3–O1 in H_2ca and of 0.019 Å for C14–C15 in Phz (see Appendix A). The next largest variations of bond lengths are found for C3–C2, C1–C2 and C1–O4 (Table 3.4). These bonds are precisely those involved in resonance stabilization of the Hca^- ion, as it is obtained after transfer of the proton within the O1–H1o1$\cdots$N1 hydrogen bond. Further evidence for this interpretation comes from t-plots (Fig. 3.3), which show that an elongation of the O1–H1o1 bond (interpreted as proton transfer) correlates with an elongation of the C3–C2 and C1–O4 bonds, for which resonance represents the admixture of

Table 3.3: Geometry of the inter-molecular hydrogen bonds O1–H1o1$\cdots$N1 and O2–H1o2$\cdots$N2 at different temperatures corresponding to the FE-I, FE-IC and FE-II phases, respectively. Interatomic distances are given in Å and bond angles in degree. (max-min) provides the difference between maximum (max) and minimum (min) separation in dependence on the phase t of the modulation in the FE-IC phase. Mean gives the value averaged over t. Standard uncertainties are given in parentheses.

Atoms	170 K [a] distance	139 K distance	max-min	100 K [b] distance
O1–H1o1	1.02(4)	1.44(2) (mean)	0.25	0.943(15) (A)
		1.32(2) (min)		1.609(15) (B)
		1.57(2) (max)		1.066(14) (C)
				1.467(14) (D)
O2–H1o2	0.73(2)	0.91(2) (mean)	0.06	0.863(15) (A)
		0.88(2) (min)		0.796(15) (B)
		0.94(2) (max)		0.840(14) (C)
				0.815(13) (D)
H1o1–N1^{i}	1.66(4)	1.320(14) (mean)	0.42	1.879(15) (A)
		1.11(2) (min)		1.027(15) (B)
		1.53(2) (max)		1.700(14) (C)
				1.205(14) (D)
H1o2–N2^{ii}	2.15(2)	1.945(2) (mean)	0.05	1.908(14) (A)
		1.92(2) (min)		2.121(14) (B)
		1.97(2) (max)		1.944(14) (C)
				2.084(14) (D)
O1–N1^{i}	2.6446(16)	2.629(2) (mean)	0.07	2.6976(14) (A)
		2.586(2) (min)		2.5736(14) (B)
		2.672(2) (max)		2.6726(14) (C)
				2.5974(42) (D)
O2–N2^{ii}	2.7722(16)	2.763(2) (mean)	0.09	2.7086(15) (A)
		2.715(3) (min)		2.8251(15) (B)
		2.811(3) (max)		2.7264(15) (C)
				2.8062(15) (D)
O1–H1o1–N1^{i}	159 (3)	144.8(15) (mean)	9.9	143.8(11) (A)
		139.5(14) (min)		154.4(11) (B)
		149.7(16) (max)		149.3(10) (C)
				152.6(10) (D)
O2–H1o2–N2^{ii}	145(2)	149.2(18) (mean)	5.4	153.7(11) (A)
		146.4(17) (min)		147.5(12) (B)
		152.0(18) (max)		154.5(11) (C)
				147.60(12) (D)

Symmetry codes for N1 and N2 in the structure model at $T = 139$ K are: (i) $x-1, y, z$; (ii) $x, y+1, z$. [a]From (Gotoh et al., 2007). [b]From (Noohinejad et al., 2014); the labels A, B, C, and D refer to the four molecular chains, which have become independent in the crystal structure at low temperatures.

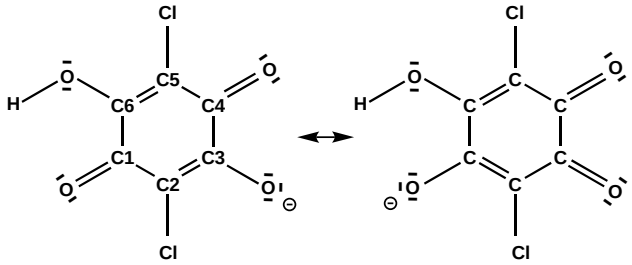

Figure 3.4: Schematic representation of resonance within the anion Hca^- of chloranilic acid.

single-bond character into these formally double bonds (Fig. 3.4). Concomitantly, C1–C2 and C3–O1 have become shorter due to admixture of double-bond character into formally single bonds. A similar variation of bond lengths is found in the crystal structure of the FE-II phase (Table 3.4). The results support the model of partial proton transfer (see Section 3.3.3).

3.3.3 The ferroelectric phase transitions

Ferroelectricity in Phz-H_2ca at low temperatures is the result of intermolecular proton transfer within the O1–H1o1$\cdots$N1 hydrogen bonds (Horiuchi, Kumai and Tokura, 2005; Kumai et al., 2007; Gotoh et al., 2007; Kumai et al., 2012; Noohinejad et al., 2014). Consideration of the positions of the hydrogen atoms within the O1–H1o1$\cdots$N1 hydrogen bonds of the crystal structures of the three phases leads to the following model for the phase transitions.

At room temperature (PE phase) all hydrogen bonds are equivalent by symmetry of the centrosymmetric space group. Consequently, any dipole moment of the O1–H1o1$\cdots$N1 hydrogen bond will be perfectly compensated by a dipole moment of the O2–H1o2$\cdots$N2 hydrogen bond on the same molecule that points in the opposite direction, because O1 and O2 are related by the inversion center. The ferroelectric phase transition towards the FE-I phase is characterized by loss of inversion symmetry. The O2–H1o2 remains short and should be interpreted as a covalent O–H bond that acts as hydrogen-bond donor towards N2 (Table 3.3). The O1–H1o1 is clearly elongated as compared to a covalent bond, but it is not completely broken. The N1–H1o1 distance is clearly shorter than in the PE phase, but it is not yet the distance of ≈ 1.03 Å of a covalent N–H bond. Therefore, it can be concluded that this structure exhibits partial proton transfer within the O1–H1o1$\cdots$N1 hydrogen

Table 3.4: Selected bond lengths (Å) at different temperatures corresponding to the FE-I, FE-IC and FE-II phases, respectively. (max-min) provides the difference between maximum (max) and minimum (min) separation in dependence on the phase t of the modulation in the FE-IC phase. Mean gives the value averaged over t. Standard uncertainties are given in parentheses.

Bond	170 K [a]	139 K		100 K [b]
	distance	distance	max-min	distance
C3–O1	1.2923(13)	1.281(2) (mean)	0.060	1.3200(14) (A)
		1.251(2) (min)		1.2536(14) (B)
		1.311(2) (max)		1.3054(14) (C)
				1.2676(14) (D)
C6–O2	1.3204(13)	1.312(3) (mean)	0.004	1.3133(15) (A)
		1.310(2) (min)		1.3204(15) (B)
		1.314(2) (max)		1.3118(14) (C)
				1.3214(14) (D)
C4–O3	1.2269(15)	1.219(2) (mean)	0.008	1.2243(14) (A)
		1.215(2) (min)		1.2211(14) (B)
		1.223(2) (max)		1.2248(14) (C)
				1.2201(14) (D)
C1–O4	1.2291(15)	1.221(2) (mean)	0.026	1.2183(14) (A)
		1.208(2) (min)		1.2385(14) (B)
		1.234(2) (max)		1.2210(14) (C)
				1.2355(14) (D)
C1–C2	1.4404(15)	1.428(3) (mean)	0.043	1.4590(8) (A)
		1.406(3) (min)		1.4114(7) (B)
		1.449(3) (max)		1.4496(8) (C)
				1.4207(8) (D)
C2–C3	1.3713(16)	1.372(3) (mean)	0.047	1.3517(9) (A)
		1.349(3) (min)		1.3949(9) (B)
		1.396(3) (max)		1.3622(9) (C)
				1.3843(9) (D)
N1–C12	1.3493(13)	1.342(2) (mean)	0.006	1.3451(11) (A)
		1.339(2) (min)		1.3465(11) (B)
		1.345(2) (max)		1.3468(14) (C)
				1.3443(12) (D)
N1–C17	1.3472(17)	1.344(2) (mean)	0.005	1.3490(14) (A)
		1.342(2) (min)		1.3505(14) (B)
		1.347(2) (max)		1.3464(14) (C)
				1.3526(14) (D)

[a]From (Gotoh et al., 2007). [b]From (Noohinejad et al., 2014).

bonds.

The low-temperature FE-II has four crystallographically independent O1–H1o1$\cdots$N1 hydrogen bonds. The partial proton transfer of the FE-I phase is replaced in the FE-II phase by complete proton transfer in one half of these hydrogen bonds (B and D), and the absence of proton transfer in the other half (A and C) (Table 3.3). The FE-I phase transfers into the FE-II phase via the intermediate FE-IC phase. Structurally, the FE-IC phase appears intermediate between the high- and low-temperature ferroelectric phases too. The incommensurate modulations represents a modulation of the O1–H1o1$\cdots$N1 hydrogen bond between one with almost full proton transfer and one which can be characterized as almost no proton transfer (Table 3.3 and Fig. 3.3). Despite an incommensurability of the FE-IC phase, it appears that—on average—one quarter of the hydrogen bonds has full proton transfer in both the FE-IC and FE-II phases, while half of the hydrogen bonds in the FE-I phase are affected by partial proton transfer. These similarities might explain the only marginal effects of the ferroelectric incommensurate and lock-in transitions on the macroscopic electric dipole moment (Horiuchi et al., 2009).

3.4 Conclusions

The incommensurately modulated structure of the ferroelectric incommensurate (FE-IC) phase of Phz-H_2ca has been successfully determined. It is shown that this structure is intermediate between the ferroelectric FE-I and FE-II phases. Half of the intermolecular hydrogen bonds exhibit partial proton transfer within the FE-I phase. This becomes an incommensurate variation between strong and very weak proton transfer within the FE-IC phase, while in the FE-II phase, the active half of the hydrogen bonds splits into a hydrogen bond with complete proton transfer and one without proton transfer. Strong support for proton transfer in part of the hydrogen bonds has been obtained through the variations of the lengths of precisely those bonds that are involved in resonance stabilization of the Hca^- ion (Section 3.3.2). Proton transfer in only part of the hydrogen bonds has been explained as the result of Coulomb interactions between the resulting ionic species (Kumai et al., 2012). Proton transfer is in line with the acidities of the two molecules with $pK_{a1} = 1.23$ for the proton acceptor Phz, and $pK_{a1} = 0.76$ for the proton donor H_2ca (Albert and Phillips, 1956; Molcanov and Kojic-Prodic, 2010). One could thus suggest that the incommensurability will be the result of competition between the inclination to-

wards proton transfer of single hydrogen bonds and avoiding unfavorable Coulomb repulsion within the crystalline lattice of molecules.

3.5 Acknowledgement

Single crystals were grown by Alfred Suttner at the Laboratory of Crystallography in Bayreuth. The help of Carsten Paulmann with diffraction experiments with synchrotron radiation at beamline F1 of Hasylab at DESY, Hamburg, is gratefully acknowledged. Beamtime has been awarded under proposal No. II-20100019. The research of L. N. has been made possible through financial support by the German Academic Exchange Service (DAAD).

Chapter 4

Ferroelectricity of phenazine–chloranilic acid at T = 100 K [1]

4.1 Introduction

Most applications of ferroelectric materials involve inorganic compounds, such as lead zirconate titanate Pb(Zr,Ti)O_3 (PZT), barium titanate $BaTiO_3$ (BTO), layered perovskites like strontium bismuth tantalate $SrBi_2Ta_2O_9$ (SBT), and lithium niobate $LiNbO_3$ (LNB).(Gonzalo, 1990) The performance of low-molecular-weight organic ferroelectrics generally is less good than of these oxides. Nevertheless, organic compounds are an attractive alternative to inorganic ferroelectric materials, because they are lead free, environmentally friendly and potentially cheaper to produce.

Recently, diisopropylammonium bromide (DIPAB) has been reported to exhibit a spontaneous electrical polarisation of similar magnitude as BTO.(Fu et al., 2013) Ferroelectricity in DIPAB is the result of alignment of the polar molecules in the crystal. Another mechanism of ferroelectricity is proton transfer within hydrogen bonds, resulting in charge separation on originally neutral molecules. A single-molecule material of this type is croconic acid.(Horiuchi et al., 2010) Ferroelectric properties have also been reported for the hydrogen-bonded co-crystal of phenazine (Phz) and 2,5-dichloro-3,6-dihydroxy-p-benzoquinone (chloranilic acid, H_2ca) as well

[1] This chapter has been published as: Leila Noohinejad, Swastik Mondal, Alexander Wölfel, Sk Imran Ali, Andreas Schönleber, and Sander van Smaalen : Ferroelectricity of phenazine–chloranilic acid at T = 100 K; *J. Chem. Crystallogr*, **44**: 387- 393 (2014)

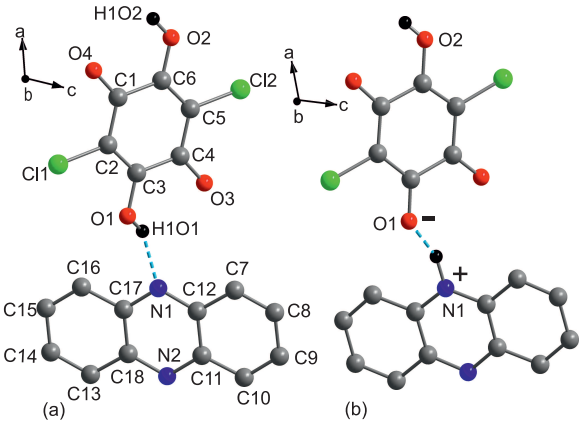

Figure 4.1: Phenazine $C_{12}H_8N_2$ (bottom) and chloranilic acid $C_6Cl_2H_2O_4$ (top) with the atom labels as employed in the present work. (a) Neutral form with an O–H$\cdots$N intermolecular hydrogen bond (molecules A—see Fig. 5.5), and (b) ionic form with an O$\cdots$ H–N hydrogen bond (molecules B). Hydrogen atoms attached to carbon atoms of Phz are not shown.

as for similar co-crystals containing bromanilic acid or fluoranalic acid instead of H_2ca (Fig. 4.1).(Horiuchi, Ishii, Kumai, Okimoto, Tachibana, Nagaosa and Tokura, 2005)

Phz-H_2ca is paraelectric at room temperature (PE phase). The crystal contains mixed chains of hydrogen bonded, neutral Phz and H_2ca molecules, which run along $[1\,1\,0]$ and $[1\,\bar{1}\,0]$ of the monoclinic unit cell with space group $P2_1/n$ (Fig. 4.2).(Horiuchi, Ishii, Kumai, Okimoto, Tachibana, Nagaosa and Tokura, 2005) The first ferroelectric (FE-I) phase forms at temperatures below $T_c^I = 253$ K. The reduction of symmetry towards $P2_1$ is the result of proton displacements within half of the hydrogen bonds (one per molecule).(Horiuchi, Ishii, Kumai, Okimoto, Tachibana, Nagaosa and Tokura, 2005; Gotoh et al., 2007; Kumai et al., 2007) Ferroelectricity remains on further cooling, but two more phase transitions have been identified.(Saito et al., 2006) An incommensurate (FE-IC) phase forms below $T_c^{IC} = 147$ K, which becomes a twofold superstructure below the lock-in transition at $T_c^{II} = 137$ K (FE-II phase).(Horiuchi et al., 2009) Crystal structures have not been reported for the FE-IC and FE-II phases. However, models have been proposed for the FE-II phase, which involve various distributions over the unit cell of neutral and ionic hydrogen bonds (Fig. 4.1).(Horiuchi et al., 2009; Amano et al., 2009; Lee et al., 2012) In particular, Kumai *et al.*(Kumai et al., 2012) proposed that Coulomb repulsion would be responsible for an arrangement of neutral (Fig. 4.1(a)) and ionic

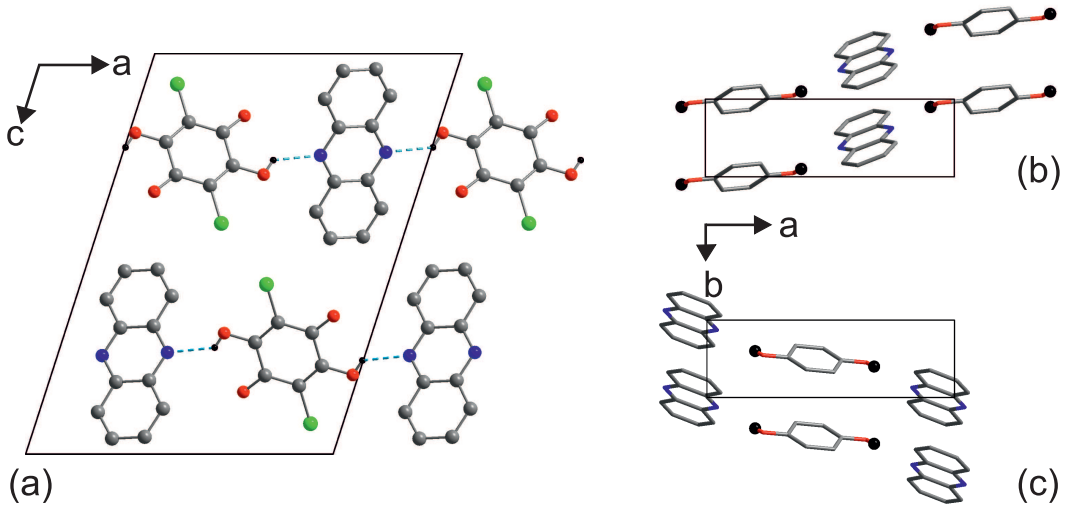

Figure 4.2: Crystal structure at ambient conditions. (a) Projection along **b**. (b) Projection along $\mathbf{c}^*$ of the layer centered on $z = 0.25$ containing hydrogen-bonded chains along $[1\,1\,0]$, (c) and of the layer centered on $z = 0.75$ with chains along $[1\,\bar{1}\,0]$.

(Fig. 4.1(b)) chains, which alternate along **b**.

Here, we report the twofold superstructure of the FE-II phase at 100 K. A description as commensurately modulated structure within the superspace approach(van Smaalen, 2012; Schönleber, 2011) appeared to be essential for solving this superstructure. We establish proton transfer in one quarter of the hydrogen bonds in a pattern similar to the charge order proposed by Kumai *et al.*,(Kumai et al., 2012) and at variance with other models.(Horiuchi et al., 2009; Amano et al., 2009; Lee et al., 2012) The role of hydrogen bonding in stabilizing the Fe-II phase is analyzed.

4.2 Experimental

4.2.1 Crystal growth

Sublimation experiments were performed in evacuated quartz glass ampoules (pressure less than 7×10^{-3} mbar) with a temperature T_1 at the educt side and a temperature T_2 at the product side. Phenazine (Alfa; purity 99%) and chloranilic acid (Alfa; 98%) were purified by repeated sublimation with $T_1 = 423$ and $T_2 = 293$ K for phenazine, and $T_1 = 458$ and $T_2 = 293$ K for chloranilic acid. Co-crystals were obtained by sublimation of a mixture of phenazine and chloranilic acid of molar ratio 1:1 placed at the educt side in a quartz glass tube.(Horiuchi, Ishii, Kumai,

Okimoto, Tachibana, Nagaosa and Tokura, 2005) The following temperature profile was used: heating of product side to $T_2 = 453$ K (2 hours), heating of educt side to $T_1 = 423$ K (2 hours), cooling of product side to $T_2 = 293$ K (6 hours), slow cooling of ampoule to ambient temperature (1 hour). Dark brown crystals in the shapes of plates were obtained at the product side.

In alternative procedures, a 1:1 molar mixture of phenazine and chloranilic acid was dissolved in ethanol or in acetone. Crystallisation was achieved by slow evaporation of the solvent. Needle-shaped crystals were obtained in this case.

4.2.2 X-ray diffraction

Single-crystal X-ray diffraction experiments have been performed at beam line F1 of Hasylab at DESY (Hamburg, Germany) with monochromatic radiation of wavelength $\lambda = 0.5600$ Å. Single crystals of dimensions between 0.05 and 0.30 mm were glued to glass hairs attached to copper pins and mounted on a standard goniometer head placed on a Huber four-circle *kappa* diffractometer. Diffraction data were collected with a MAR165CCD area detector, employing ϕ and ω scans. The temperature of the crystal was regulated by an open-flow nitrogen-gas cryostat by Oxford Cryosystems.

Preliminary diffraction experiments confirmed that both needle-shaped and platelike crystals possess the lattice parameters of Phz-H_2ca.(Horiuchi, Ishii, Kumai, Okimoto, Tachibana, Nagaosa and Tokura, 2005) A platelet crystal of dimensions $0.22 \times 0.13 \times 0.05$ mm^3 was selected for the diffraction experiment at $T = 100$ K. Diffraction data were collected in multiple runs, employing various off-sets for the setting angles of the diffractometer. The effective dynamic range of the experiment was increased by repeating runs with exposure times of 4, 36 and 300 s.

The software Eval15(Schreurs et al., 2010) was used for data processing of the measured diffraction images. All Bragg reflections could be indexed by a pseudo-monoclinic, F-centered $2\mathbf{a} \times 2\mathbf{b} \times 2\mathbf{c}$ supercell of the primitive monoclinic unit cell valid at temperatures above T_c^{IC} (twofold superstructure). Alternatively, the diffraction data can be indexed on the primitive $\mathbf{a} \times \mathbf{b} \times \mathbf{c}$ monoclinic unit cell together with a commensurate modulation wavevector $\mathbf{q}$, then allowing the superspace approach to be used for structural analysis (Table 5.1).(Janssen et al., 2006; Schönleber, 2011; van Smaalen, 2012) In this description, all Bragg reflections are indexed by four integers (h, k, l, m) according to:

$$\mathbf{H} = h\mathbf{a}^* + k\mathbf{b}^* + l\mathbf{c}^* + m\mathbf{q} \tag{4.1}$$

Main reflections have indices $(h, k, l, 0)$, while superlattice reflections are indexed as satellite reflections with indices $(h, k, l, 1)$. Because $2\mathbf{q} = (1, 1, 1)$ is a reciprocal lattice vector of the basic-structure lattice, only one order of satellite reflections $(m = 1)$ exists.

Employing either kind of indexing, integrated intensities were obtained of 61772 Bragg reflections. Absorption correction was applied to these data by SADABS (Sheldrick, 2008). The data were averaged in point group 1 (Table 5.1). Since inversion twin domains possess equal volume fractions (Section 4.2.3), the absorption correction was determined by SADABS employing equivalence relations based on point symmetry $\bar{1}$.

4.2.3 Determination of the superstructure

The crystal structure of the FE-I phase with space group $P2_1$ is preserved as basic structure at low temperatures. Accordingly, a successful refinement of this structure was obtained against the main reflections, resulting in a R value of $R_F^{obs} = 0.0411$.

The superstructure is described as commensurately modulated structure within the superspace approach.(van Smaalen, 2012) The symmetry then is given by the monoclinic superspace group $P2_1(1/2\,\sigma_2\,1/2)0$, No. 4.1.6.3 with standard setting $P2_1(1/2\,0\,\gamma)0$ and $\gamma = \sigma_2$.(Stokes et al., 2011; van Smaalen et al., 2013) The positions of the atoms are described as the sum of a position in the basic-structure unit cell and a value of a single-harmonic modulation function defined by

$$u_i^{\mu}(\bar{x}_{s4}) = A_i^{\mu} \sin(2\pi\bar{x}_{s4}) + B_i^{\mu} \cos(2\pi\bar{x}_{s4}) \tag{4.2}$$

Each atom μ in the basic-structure unit cell has modulation amplitudes A_i^{μ} and B_i^{μ} for coordinates $i = x, y, z$. Similar modulation functions were applied to the anisotropic atomic displacement parameters (ADPs) for all non-hydrogen atoms.

In the present case, all physical-space sections t of superspace lead to the same superstructure, so that the value $t = 0$ was chosen for all computations. Employing the transformation from the superspace to the supercell descriptions shows that the twofold superstructure has triclinic symmetry $P1$. Here, we describe this superstructure by an eightfold $2\mathbf{a} \times 2\mathbf{b} \times 2\mathbf{c}$ pseudo-monoclinic unit cell, which then is F centered (space group $F1$). Since the low-temperature phase has been obtained through phase transitions by cooling a crystal with originally $P2_1/n$ symmetry at room temperature, one can expect the crystal to be twinned by pseudo-merohedry. The structure refinements showed that domains related by the inversion have equal

Table 4.1: Crystal data and structure refinements for the superspace and supercell models M_{free}.

	Superspace	Supercell
Temperature (K)	100	100
Chemical formula	$C_{18}H_{10}Cl_2N_2O_4$	$C_{18}H_{10}Cl_2N_2O_4$
Formula weight	389.19	389.19
(Super-)space	$P2_1(1/2\,\sigma_2\,1/2)0$	$F1$
group	No. 4.1.6.3	No. 1
q	(1/2, 1/2, 1/2)	–
a (Å)	12.4141(2)	24.8282(4)
b (Å)	3.7627(5)	7.5254(10)
c (Å)	16.855(2)	33.711(4)
β (deg)	107.772(7)	107.772(7)
V (Å^3)	749.76(14)	5998.1(11)
Z	2	16
D_{calc} ($g\,cm^{-3}$)	1.7234	1.7234
Crystal size (mm^3)	$0.22 \times 0.125 \times 0.05$	
Crystal color	dark brown	
Crystal form	platelet	
Radiation type	synchrotron	
Wavelength (Å)	0.5600	
Scan mode	ω and ϕ	
Theta range (deg)	1.9–29.8	
μ (mm^{-1})	0.242	
Absorption corr.	SADABS	
T_{min}, T_{max}	0.5288, 0.7459	
No. of reflections		
Measured	61772	
Independent	27880	
Observed	25683	
Main (obs, all)	13289, 13945	
Satellites (obs, all)	12394, 13935	
R_{int}	0.0478	
GOF^{obs},GOF^{all}	2.81, 2.71	2.30, 2.19
R_F^{obs}, R_F^{all} (all)	0.0431, 0.0468	0.0431, 0.0468
R_F^{obs}, R_F^{all} (main)	0.0404, 0.0434	0.0405, 0.0435
R_F^{obs}, R_F^{all} (sat)	0.0604, 0.0680	0.0605, 0.0680
No. of parameters	719	2[a]
Extinction	Type I, Isotropic	
correction	Gaussian distribution	
$\Delta\rho_{max}$, $\Delta\rho_{min}$	0.67, -0.71	0.74, -0.96
(e Å^{-3})		

[a] *Refinement of only the scale factor and extinction parameter.*

volume fractions. Employing this constraint on the four possible domains resulted in a volume fraction of 0.2476 (6) for the initial twin domain.

All structure refinements were performed with JANA2006.(Petricek et al., 2014) The atomic coordinates of the crystal structure at $T = 160$ K were used as starting point for the successful refinement of the basic structure against main reflections within space group $P2_1$. Hydrogen atoms attached to the carbon atoms were placed at calculated positions in the plane of the phenyl ring with bond lengths of d(C–H) = 0.96 Å and equal C–C–H bond angles. Their positions and ADPs were constrained employing a riding model with isotropic ADPs equal to 1.2 times that of the carbon atoms they are bonded to. Hydrogen atoms of the hydroxyl groups were initially located in the difference Fourier map. Their positions were subsequently refined while applying restraints d(O–H) = 0.85±0.02 Å on the bond lengths and 109.5±2.0° on the C–O–H bond angles.(Müller et al., 2005; Engh and Huber, 1991) The second value indicates the steepness of each constraint. A riding model was used for the ADPs with isotropic ADPs of hydrogen atoms set equal to 1.5 times the equivalent isotropic ADP of the oxygen atom it is bonded to.

Employing the monoclinic superspace symmetry, modulation amplitudes according to Eq. 4.2 were introduced for all atoms of the basic structure, and they were given small positive values. Refinement of the modulated structure against all reflections, while keeping the constraints and restraints for hydrogen atoms, converged to a good fit to the diffraction data with R_F^{obs}(all) = 0.0434, R_F^{obs}(main) = 0.0407 and R_F^{obs}(sat) = 0.0612. The resulting structure model is denoted as $\mathrm{M_{res}}$.

A second structure model, denoted as $\mathrm{M_{free}}$, was created by a refinement in which the restraints on the bond lengths and bond angles of the hydrogen atoms of the hydroxyl groups were removed. A marginally better fit to the diffraction data was obtained than for $\mathrm{M_{res}}$ (Table 5.1). Main differences between the two models are the positions of the hydrogen atoms.

The final superspace models were transformed into structure models on the eightfold $2\mathbf{a}\times 2\mathbf{b}\times 2\mathbf{c}$ supercell with space group $F1$. Refinements of only the scale factor and extinction parameter reproduced the R values of the superspace refinements (Table 5.1). The triclinic supercell models contain four crystallographically independent atoms for each independent atom of the basic structure, which are distinguished by appending the letters A through D to the atomic names.

In a second approach, structure solution was tried within a conventional approach, directly employing the F centered eightfold supercell. Application of SUPERFLIP(Palatinus, 2004) allowed all non-hydrogen atoms to be located. Structure

refinements followed by the introduction of hydrogen atoms (riding model) finally resulted in a fit to the diffraction data with $R_F^{obs}(\text{all}) = 0.0456$, $R_F^{obs}(\text{main}) = 0.0420$ and $R_F^{obs}(\text{sat}) = 0.093$. The significantly higher partial R value for the superlattice reflections testifies that the solution for the superstructure is less good in this case than in case of the superspace approach (compare Table 5.1).

4.3 Results and discussion

Single crystals of Phz-H_2ca grown by sublimation possess a much less anisotropic shape than single crystals grown from solution. The former are thus more suitable for X-ray diffraction experiments, and one specimen has been used for the present diffraction experiment of the FE-II phase at a temperature of 100 K.

The superstructure has been successfully solved within the superspace approach. Apart from small displacements of all atoms, major effect of the formation of the superstructure is the repositioning of hydrogen atoms of the hydroxyl groups as compared to their positions within the FE-I phase at 160 K.(Horiuchi, Ishii, Kumai, Okimoto, Tachibana, Nagaosa and Tokura, 2005; Gotoh et al., 2007) The refinement with strong restraints on the O–H bond lengths (model M_{res}) already suggests that two out of eight hydrogen atoms are not bonded to oxygen any more (Table 4.2). Free refinement of the positions of all eight hydrogen atoms of the four H_2ca molecules (model M_{free}) then gives proof that these two hydrogen atoms are transferred from oxygen to nitrogen; the observed N–H distances are close to the value of 1.03 Å expected for N–H bonds in organic salts.(Allen et al., 1987) The O–H$\cdots$N hydrogen bond is replaced by an O$\cdots$H–N hydrogen bond.

Both the PE and FE-I phases contain a single crystallographically independent molecule of Phz and of H_2ca [Fig. 4.1(a)]. H_2ca is centrosymmetric within the PE phase, such that any supposed polarization through proton transfer within the O1–H$\cdots$N1 hydrogen bond would be matched by a polarization of opposite sign within the O2–H$\cdots$N2 hydrogen bond. The FE-I phase is defined by O1 and O2 being crystallographically independent atoms, thus allowing for partial proton transfer of solely the O1–H$\cdots$N1 hydrogen bond [Fig. 4.1(b)].(Horiuchi, Ishii, Kumai, Okimoto, Tachibana, Nagaosa and Tokura, 2005; Gotoh et al., 2007; Kumai et al., 2007) The FE-II phase is characterized by loss of the twofold screw axis as well as by the formation of a twofold superstructure, resulting in a total of four crystallographically independent molecules of both species. They separate into four hydrogen-bonded

mixed chains that run along [1, ±1, 1] (Fig. 5.5), and that we denote by A, B, C and D chains, while the appropriate letter is appended to the symbols of the atoms (compare Table 4.2).

As is apparent from the experimental O–H and N–H distances, one of the two hydrogen bonds of each of the four H_2ca molecules remains an O–H$\cdots$N hydrogen bond (O2 and N2 atoms; see Table 4.2), whereas half of the molecules is involved in proton transfer, then resulting in an O$\cdots$H–N type of hydrogen bond for O1 and N1 atoms. Proton transfer thus is found on chains B and D, while molecules in chains A and C remain neutral. The present results provide strong experimental evidence in favor of the theoretical model proposed by by Kumai *et al.*(Kumai et al., 2012) and it is at variance with the model proposed by Lee *et al.*(Lee et al., 2012) as well as earlier models for the mechanism of ferroelectricity in this compound.

Table 4.2: Intermolecular hydrogen bonds (Å, deg) for both structure models M_{free} and M_{res}.

Hydrogen bond		d(O–H)	d(H–N)	d(O$\cdots$N)	angle
O1A–H1o1A$\cdots$N1A^{i}	M_{free}	0.943(15)	1.879(15)	2.6976(14)	143.8(11)
	M_{res}	0.909(13)	1.921(13)	2.6997(14)	142.5(10)
O1B$\cdots$H1o1B–N1B^{i}	M_{free}	1.609(15)	1.027(15)	2.5736(14)	154.4(11)
	M_{res}	1.247(13)	1.397(13)	2.5747(14)	153.8(9)
O1C–H1o1C$\cdots$N1C^{ii}	M_{free}	1.066(14)	1.700(14)	2.6726(14)	149.3(10)
	M_{res}	0.956(13)	1.830(12)	2.6735(14)	145.5(9)
O1D$\cdots$H1o1D–N1D^{ii}	M_{free}	1.467(14)	1.205(14)	2.5974(42)	152.6(10)
	M_{res}	1.190(13)	1.487(12)	2.5999(14)	152.1(9)
O2A–H1o2A$\cdots$N2A^{iii}	M_{free}	0.863(15)	1.908(14)	2.7086(15)	153.7(11)
	M_{res}	0.806(13)	1.989(12)	2.7104(15)	148.8(9)
O2B–H1o2B$\cdots$N2B^{iii}	M_{free}	0.796(15)	2.121(14)	2.8251(15)	147.5(12)
	M_{res}	0.794(13)	2.149(12)	2.8259(16)	143.3(10)
O2C–H1o2C$\cdots$N2C^{iii}	M_{free}	0.840(14)	1.944(14)	2.7264(15)	154.5(11)
	M_{res}	0.809(13)	2.002(12)	2.7271(15)	148.9(9)
O2D–H1o2D$\cdots$N2D^{iii}	M_{free}	0.815(43)	2.084(14)	2.8062(15)	147.60(12)
	M_{res}	0.788(13)	2.135(12)	2.8081(15)	143.4(10)

Symmetry codes: $^{i}x-1,y,z$; $^{ii}x+1,y,z$; $^{iii}x,y+1,z$.

A simple point charge model with a negative charge of one electron on oxygen O1 and a positive charge on the matching N1 atom leads to a dipole moment of this hydrogen bond that is approximately directed along [±1, 2 0] (Table 4.3). Since only

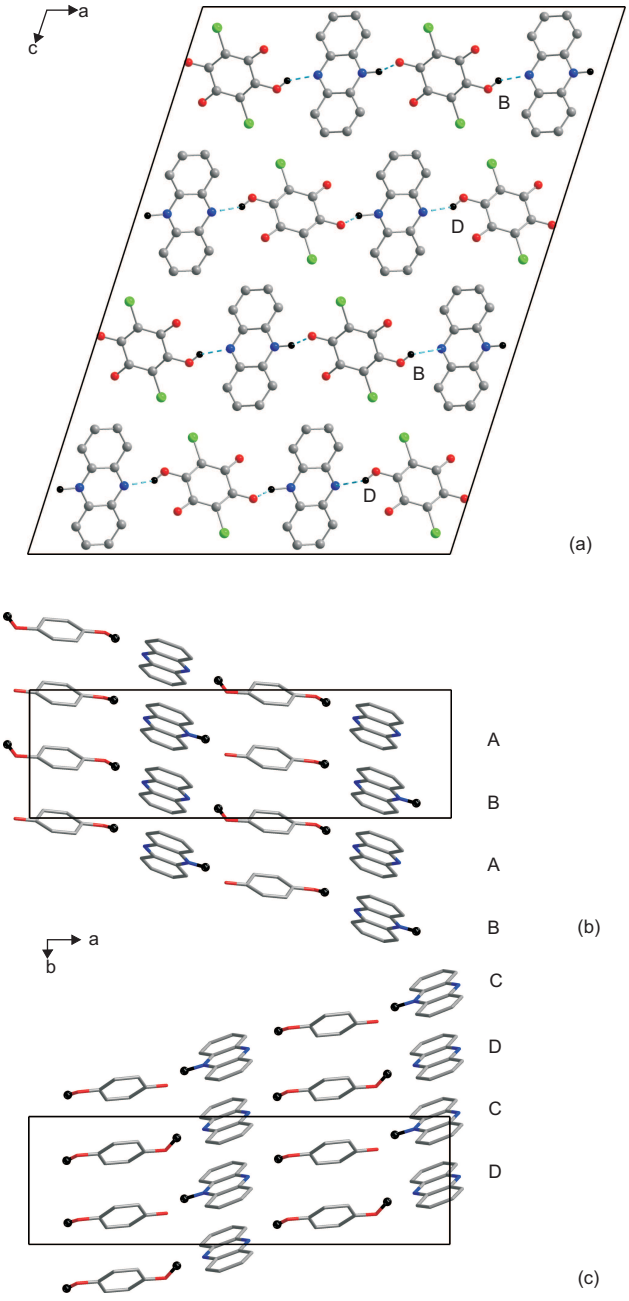

Figure 4.3: Projections of the crystal structure of the FE-II phase. (a) **a**, **c** Plane of the F-centered triclinic supercell with a projection of the type B and type D chains. (b) **a**, **b** Plane with type A and type B chains centered on $z \approx 0.125$. (c) **a**, **b** Plane with type C and type D chains centered on $z \approx 0.375$. Cl atoms, H atoms of Phz, and double-bonded O atoms have been omitted from (b) and (c) for clarity.

chains B and D contain the ionic O1$\cdots$H–N1 hydrogen bond, the polarisation of the material is the sum of their contributions. The direction of the resulting polarisation vector is close to **b**, reminiscent of the monoclinic symmetry at higher temperatures. Consideration of dipole moments of the A and C chains shows that the direction of a polarisation that would be the sum of A, B, C and D is exactly along **b** (Table 4.3). This feature is the result of the superspace approach to the crystal structure, by which atomic displacements are described by a single normal mode of the high temperature space group $P2_1$.(Perez-Mato et al., 2010; van Smaalen, 2012)

Within the model of Kumai *et al.*(Kumai et al., 2012) only B and D chains contribute to the polarisation. Accordingly, we find a magnitude of 2.54 μC/cm^2 from the point charge model and the experimental crystal structure. This value is in good agreement with the experimental value.(Horiuchi, Kumai and Tokura, 2005) It is also close to the value of 2.25 μC/cm^2 as obtained from full electronic structure calculations.(Lee et al., 2012) (Lee *et al.*(Lee et al., 2012) obtained 4.5 μC/cm^2 assuming proton transfer on all molecules.)

However, it is interesting to note that the two molecules without clear proton transfer do show elongated O–H bonds (O1A-H and O1C-H in Table 4.2) similar to the elongated O1–H bond in the FE-I phase.(Horiuchi, Ishii, Kumai, Okimoto, Tachibana, Nagaosa and Tokura, 2005; Gotoh et al., 2007; Kumai et al., 2007) The latter is supposedly responsible for the polarisation above T_c^{IC}. Contributions to the polarisation of these molecules should be considered in any theoretical approaches.

Table 4.3: Dipole moments of intermolecular hydrogen bonds O1–H$\cdots$N. Vectors **p** are given by their approximate lattice directions, and with respect to a Cartesian coordinate system with $\hat{x}_c \parallel \mathbf{a}$, $\hat{y}_c \parallel \mathbf{b}$, and $\hat{z}_c \perp \mathbf{a}, \mathbf{b}$. Values are normalised to give the contribution to the polarisation in μC/cm^2. Data are for the structure model M_{free}. B + D: sum of contributions of molecules B and D; A + C: sum of contributions of molecules A and C.

Hydrogen bond	lattice direction	(p_x, p_y, p_z)	magnitude
O1A–H1o1A$\cdots$N1A^{i}	[1, 2, 0]	(2.413, 1.341, −0.829)	2.882
O1B$\cdots$H1o1B–N1B^{i}	[1, 2, 0]	(2.352, 1.261, −0.664)	2.750
O1C–H1o1C$\cdots$N1C^{ii}	[−1, 2, 0]	(−2.403, 1.322, 0.795)	2.856
O1D$\cdots$H1o1D–N1D^{ii}	[−1, 2, 0]	(−2.361, 1.280, 0.698)	2.775
B + D		(−0.010, 2.541, 0.034)	2.542
A + C		(0.010, 2.664, −0.034)	2.664

Symmetry codes: $^{i}x-1, y, z$; $^{ii}x+1, y, z$.

4.4 Conclusions

Crystals of Phz-H_2ca have been grown by sublimation as well as by slow evaporation of a solvent. A needle-shaped morphology has been obtained by crystallisation from solution, while platelike crystals were obtained by sublimation.

The precise crystal structure is presented for the second ferroelectric phase FE-II at a temperature of 100 K. The structural distortion with respect to the FE-I phase is successfully described by a single normal mode, which thus is found to be responsible for the low-temperature phase transitions.

The mechanism of ferroelectricity is proton transfer within one of the two hydrogen bonds of each molecule, but for only half of the molecules. A simple point charge model with one negative charge on O1 and a positive charge on N1 quantitatively reproduces the polarisation of the material. The resulting pattern of ionized hydrogen bonds O$\cdots$H–N is in agreement with the theoretical model proposed by Kumai *et al.*,(Kumai et al., 2012) and it is at variance with other theories.(Horiuchi et al., 2009; Amano et al., 2009; Lee et al., 2012) However, the O1–H$\cdots$N1 hydrogen bonds of the second half of the molecules do show elongated O1–H bonds. It is thus proposed that contributions of these molecules to the polarisation of the material should be considered in future studies.

4.5 Acknowledgement

Single crystals were grown by Alfred Suttner at the Laboratory of Crystallography in Bayreuth. We thank Carsten Paulman for assistance during the experiment at beamline F1 of Hasylab at DESY in Hamburg, Germany. The research of L. N. has been made possible through financial support by the German Academic Exchange Service (DAAD).

Chapter 5

Disordered BF_4^- Anions in the Incommensurate Crystal of Morpholinium Tetrafluoroborate[1]

5.1 Introduction

Among non-covalent interactions between molecules, hydrogen bonding has been recognized as an important and powerful interaction towards building supramolecular assemblies (Biedermann and Schneider, 2016). Hydrogen-bonded supramolecular assemblies can be found in a wide range of key systems ranging from the building blocks of life, DNA, to technological devices, *e.g.* non-linear optical devices and ferroelectrics (Sun et al., 2014; Horiuchi and Tokura, 2008). Ferroelectric and non-linear optical properties have been reported for hydrogen-bonded organic–inorganic hybrid complexes with stoichiometry ABX_4, where BX_4^- is a tetrahedral anion, like perchlorate or tetrafluoroborate, and A^+ is a heteroatomic aromatic or cycloalkane cation, like pyridinium (Czarenki et al., 1994a;b) or imidazolium (Pajak et al., 2004; Czapla et al., 2005). Different mechanisms of the ferroelectric phase transitions for these type of compounds have been reported. For the compounds mentioned above, the ferroelectric phase transition is related to the partial ordering of both the dipolar cationic moieties and the distorted tetrahedral anions at lower temperatures in comparison to higher temperatures or intermolecular hydrogen bond between cation and anion. In the case of the cation 1,4-diazabicyclo[2.2.2]octane the mechanism of the phase transition is connected to proton transfer within the intermolecular hydrogen

[1]This chapter is in preparation for publication by Leila Noohinejad, Vaclav Petricek, Andreas Schönleber, and Sander van Smaalen.

bond (Katrusiak and Szafranski, 1999).

Recently, the salt of morpholinium and tetrafluoroboric acid has been studied (Owczarek et al., 2008). At room temperature (phase I), the crystal contains hydrogen bonded chains of $[C_4H_{10}NO]^+[BF_4]^-$ in the orthorhombic unit cell with space group $Pnam$. The crystal structure of phase I has been reported by Szklarz et al. (2009) at several temperatures: 160, 180, 240 and 290 K. An incommensurate phase (phase II) forms below $T_{c,I} = 153$ K, which becomes a threefold superstructure below $T_{c,II} = 117$-118 K (phase III) (Szklarz et al., 2009; Owczarek et al., 2008). The phase transition from I to II has been classified as second order and continuous. The reduction of symmetry towards $P2_12_12_1$ on a threefold supercell (phase III) is the result of fully ordered anions at lower temperatures (Owczarek et al., 2008). The incommensurate to commensurate phase transition is classified as first order and it exhibits discontinuous character but it is non ferroelectric (Owczarek et al., 2011). For understanding the mechanism of phase transition, analysis of the structural changes in different phases is necessary. Here, we report the disordered incommensurate structure in phase II of $[C_4H_{10}NO]^+[BF_4]^-$. The incommensurately modulated structure is described within the superspace approach (van Smaalen, 2012) by the centrosymmetric superspace group $Pnam(\sigma_1\,0\,0)00s$ (No. 62.1.9.6 with standard setting $Pmcn(0\,0\,\sigma_3)s00$ (Stokes et al., 2011)). The modulation is found to involve a variation of occupancies of the four orientations of $[BF_4]^-$, correlated with displacements of the morpholinium cations. We also report the crystal structure in phase I at $T = 160$ K that is successfully refined by using the pseudo-rigid body approach for $[BF_4]^-$. The pseudo-rigid-body approach eases the refinement of the orientational fourfold disordered anion by reducing the number of parameters.

5.2 Experimental

5.2.1 Crystal growth and X-ray diffraction

16 mL of an aqueous solution of ammonium tetrafluoroborate (2.5 g, 23.8 mmol) was added to 8 mL of an aqueous solution of morpholinium (2.1g, 24.1 mmol). The solution was stirred and the volume was reduced by slow evaporation until the yellowish crystals were formed. The co-crystal was recrystallized from methanol by slow evaporation. The resulting colorless crystals were collected by filtration and dried in a vacuum desiccator over P_2O_5.

Single-crystal X-ray diffraction has been measured at T= 160 K (phase I), T

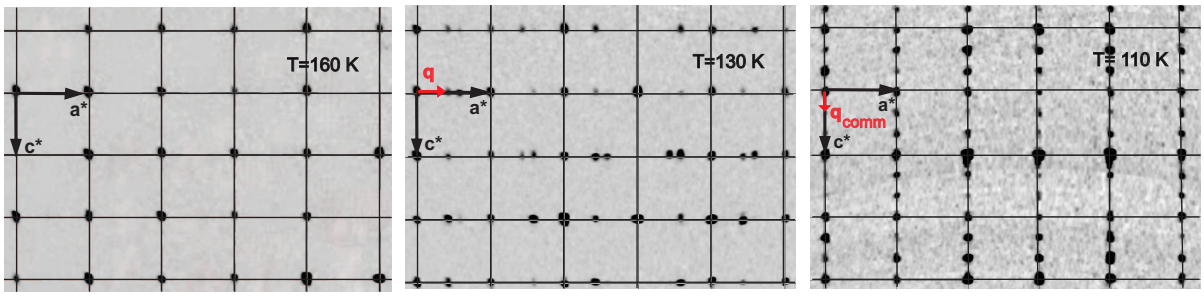

Figure 5.1: Reconstruction of $h4l$ layers of reciprocal space of morpholinium tetrafluoroborate in its (a) normal phase (phase I), (b) incommensurate phase (phase II) and (c) commensurate phase (phase III). Notice satellite reflection with $\mathbf{q} = (0.4126, 0, 0)$ in phase II and with $\mathbf{q}_{comm} = (0, 0, \frac{1}{3})$ in phase III.

= 130 K (phase II), and T= 110 K (phase III) on a MAR345 diffractometer with Mo-Kα radiation. Diffraction data were collected in multiple runs, with zero off-set of the area detector for data at 160 K, and with zero and 30 degree off-sets for data at 130 K and 110 K. The temperature of the crystal was regulated by an open-flow nitrogen cryostat. In the incommensurate and commensurate phases three different exposure times of 4, 25, and 200 seconds were used in five different runs with the same measurement strategy, in order to obtain a complete dataset including strong and weak reflections. The diffraction pattern of phase I reflects a rectangular reciprocal lattice of main reflections [Fig. 5.1(a)]. Additional Bragg peaks appeared at lower temperatures, indicating the formation of modulated phases. At T= 130 K, the diffraction pattern represents main reflections and first-order satellite reflections that can be indexed with the incommensurate modulation wave vector $\mathbf{q} = (\sigma_1, 0, 0)$, $\sigma_1 = 0.4126$ [Fig. 5.1(b)]. At T=110 K, the diffraction pattern can be indexed by main reflections together with first-order satellite reflections of commensurate modulation with $\mathbf{q}_{comm} = (0, 0, \sigma_3)$ and the rational component $\sigma_3 = \frac{1}{3}$ [Fig. 5.1(c)].

Indexing of the 130 K data by the software Eval15 (Schreurs et al., 2010) resulted in a primitive orthorhombic unit cell together with the modulation wave vector. Integrated intensities of Bragg reflections were obtained with Eval15. They were scaled and absorption correction was applied by the software Sadabs (Sheldrick, 2008). The diffraction symmetry appeared to be mmm, and the data were averaged in this point group. Main reflections are surrounded by strong first-order satellite reflections, which is noticeable in the values of R_σ (the value of the

average standard uncertainty over intensity). Nearly equal values have been found for satellite reflections (R_σ(sat) = 0.0191) and main reflections (R_σ(main) = 0.0170). In a second attempt second-order satellite reflections were included into the integration procedure with Eval15. Only a few weak second-order satellite reflections were found (R_σ(sat) = 0.1537). Incorporation into the refinement did not improve the structure model. Therefore, the structural analysis is based on the reflections up to first-order satellite reflections: reflections (h, k, l, m) with $m = 0, \pm 1$ (Fig. 5.1). Crystal data are summarized in Table 5.1.

5.2.2 Structure solution and rigid body refinement

The diffraction pattern indicates a primitive orthorhombic lattice [Fig. 5.1(b)]. The centrosymmetric orthorhombic crystal structure ($Pnam$) at high temperatures is preserved as basic structure in the incommensurate phase. Reflection conditions on the observed data are in agreement with the orthorhombic superspace group $Pnam(\sigma_1\,0\,0)00s$. (No. 62.1.9.6 with standard setting $Pmcn(0\,0\,\sigma_3)s00$ (Stokes et al., 2011; van Smaalen et al., 2013)).

The atomic coordinates of the crystal structure at T = 160 K (Szklarz et al., 2009) were used as starting point for the successful refinement of the basic structure against main reflections within space group $Pnam$. All refinements have been performed with the software Jana2006 (Petricek et al., 2014). Anisotropic atomic displacement parameters (ADPs) have been refined for the atoms of the morpholinum molecular cation. Hydrogen atoms were placed at calculated positions with bond lengths of d(C–H)=0.96 Å, and d(N–H)=0.92 Å. They were refined using a riding model with isotropic ADPs equal to 1.2 times or 1.5 times the equivalent anisotropic ADPs of the carbon or nitrogen atoms to which they are bonded to, respectively. For refinement of the fourfold orientationally disordered tetrafluoroborate anion a pseudo-rigid body approach is applied by using Jana2006. The tetrafluoroborate anion is described as one molecule. Although the ideal geometry for the tetrafluoroborate anion seems to be tetrahedral, a search in CCDC database (using ConQuest2015) as well as several recently published crystal structures of molecular compounds containing $[BF_4]^-$ show that bond lengths and angles deviate significantly from tetrahedral symmetry (Price et al., 2014; Mercadal et al., 2014; Schick et al., 2014; Buist et al., 2014). Therefore, the point group 1 is used as local symmetry of the anion (see Tables 5.2 and 5.3).

Boron has been placed at the origin of the local coordinate system of the pseudo-

Table 5.1: Crystal data and refinement details

Temperature (K)	130
Chemical formula	C_4NOH_{10} BF_4
Formula weight	174.93
Superspace group	$Pnam(\sigma_1\,0\,0)00s$
q	(0.4216(5),0,0)
a (Å)	8.0948(13)
b (Å)	9.4092(15)
c (Å)	9.5492 (14)
V (Å^3)	727.3(14)
Z	4
D_{calc} ($g\,cm^{-3}$)	1.5975
Crystal size (mm^3)	$0.22 \times 0.29 \times 0.15$
Crystal color	Colorless
Radiation type	Mo-Kα
Wavelength (Å)	0.7107
Scan mode	ϕ
Theta range (deg)	1.92 to 33.33
Range of h	0 to 10
Range of k	0 to 18
Range of l	0 to 18
Range of m	-1 to 1
μ (mm^{-1})	0.174
Absorption corr.	SADABS
T_{min}, T_{max}	0.4553 ,0.7486
No. of reflections	
Measured	47623
Independent	6389
Main reflections (obs, all)	1070, 2231
Satellites, 1st order (obs, all)	1732, 4158
$R_{int}(obs, all)$ averaged in mmm	3.16, 6.59
Criterion for observed reflection	$I > 3\sigma(I)$
Refinement, Software	on F, JANA2006
GOF^{obs},GOF^{all}	4.44, 3.04
R_F^{obs}, R_F^{all} (all),wR(all)	0.0642, 0.1711, 0.0818
R_F^{obs}, R_F^{all} (main), wR(all)	0.0519, 0.1378, 0.0817
R_F^{obs}, R_F^{all} (sat), wR(all)	0.0848, 0.2204, 0.0820
No. of parameters	185
$\Delta\rho_{max}$, $\Delta\rho_{min}$ (e Å^{-3})	0.71, -0.57

Table 5.2: Selected bond lengths (Å) with average values, maximum values and minimum values as a function of phase of modulation, t for the morpholinium molecule. The bond lengths of $[BF_4]^-$ are independent of phase of modulation. Standard uncertainties are given in parentheses.

Bond	Average	Min.	Max.
O1-C1	1.4323(13)	1.4162(13)	1.4468(13)
N1-C2	1.4942(12)	1.4784(13)	1.5086(13)
B1a-F1a	1.383(16)	1.383	1.383
B1a-F2a	1.376(17)	1.376	1.376
B1a-F3a	1.381(18)	1.381	1.381
B1a-F4a	1.377(15)	1.376	1.377
B1b-F1b	1.38(3)	1.38	1.38
B1b-F2b	1.378(14)	1.378	1.378
B1b-F3b	1.38(2)	1.38	1.38
B1b-F4b	1.38(2)	1.38	1.39

Table 5.3: Selected bond angles (deg) of the $[BF_4]^-$ molecules.

Atoms	Angle
F1a-B1a-F2a	110.6(11)
F1a-B1a-F3a	108.8(10)
F1a-B1a-F4a	109.1(11)
F2a-B1a-F3a	110.1(11)
F2a-B1a-F4a	110.2(10)
F3a-B1a-F4a	108.1(11)
F1b-B1b-F2b	110.5(12)
F1b-B1b-F3b	108.6(16)
F1b-B1b-F4b	109(2)
F2b-B1b-F3b	110.3(13)
F2b-B1b-F4b	110.2(17)
F3b-B1b-F4b	108.0(15)

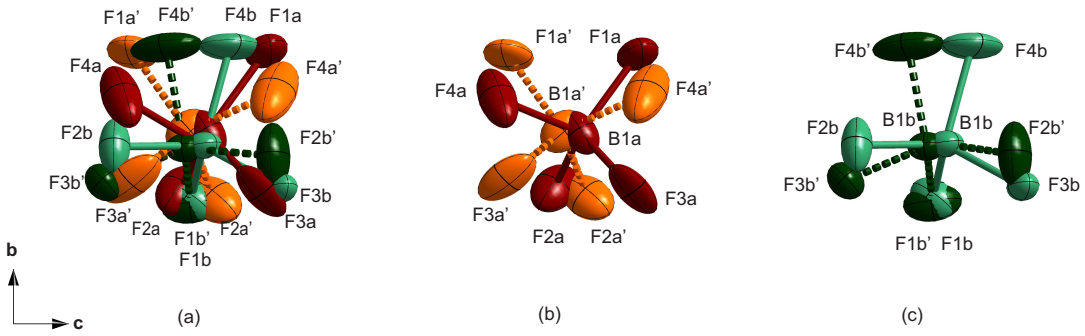

Figure 5.2: (a) Molecular structure of the fourfold disordered $[BF_4]^-$ ion, with the atom labels as employed in the present work. (a) Superposition of the four orientations of $[BF_4]^-$. (b) Orientation Ma together with Ma′ obtained from Ma by the mirror operator. (c) Orientation Mb together with Mb′.

rigid body, and it has been used to define the central point of the molecule. Disorder is described by defining and refining four positions/orientations of this molecule. The orientation of the first molecule (Ma) is defined by three rotations (angles ϕ, χ and ψ) about axes through the origin of the local coordinate system. The position of the rotated molecule Ma then is defined by a translation (again three parameters). Values of these six parameters have been initially chosen such that the atoms of Ma coincide with the atoms in the atomic model. The orientation and position of the second pseudo-rigid body (Mb) is obtained in a similar way (Tables C.1 and C.2 in the appendix). Two more positions/orientations are obtained because of the mirror symmetry of the space group, resulting in molecules Ma′ (with the same occupancy as Ma) and Mb′ (with the same occupancy as Mb). All four positions/orientations occupy the same region within the unit cell and therefore describe fourfold orientational disorder (Fig. 5.2). In order to preserve stoichiometry, the sum of occupancies of Ma and Mb has been constrained to 0.5 in all refinements.

The best fit to the diffraction data is obtained for a refinement of the average structure against main reflections, employing the TLS model for the ADPs of $[BF_4]^-$, resulting in $R_F^{obs}(main) = 0.0539$ and $wR_F^{all}(main) = 0.0838$. The refined occupancies of the different orientations of $[BF_4]^-$ are Occ(Ma) = Occ(Ma′) = 0.180 (14) and Occ(Mb) = Occ(Mb′) = 0.320. The average structure is nearly equal to the structural model at 160 K (see Table C.7 in Appendix C.2).

Charge flipping in superspace has been applied for solution of the incommensurately modulated structure (Palatinus, 2013; Palatinus and Chapuis, 2007). For the resulting superspace electron density Superflip suggested the centrosymmet-

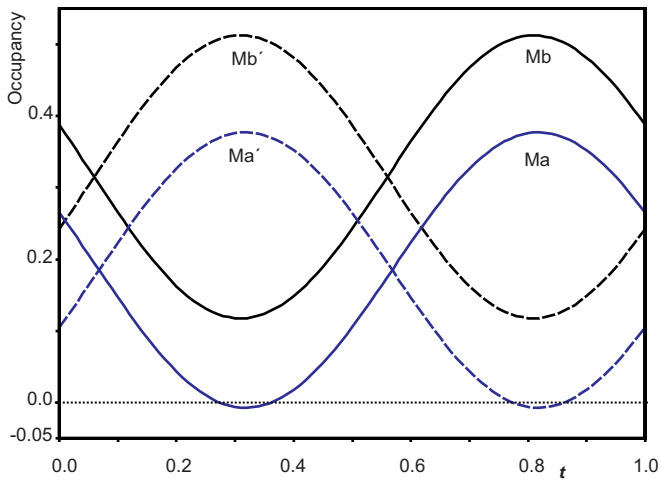

Figure 5.3: Occupancies of the four orientations of disordered $[BF_4]^-$ as a function of the phase of modulation t. Occupancies in the final structure model are shown for Ma and Mb. Dashed curves represent occupancies of Ma′ and Mb′, which are related to Ma and Mb by the superspace mirror operator.

ric superspace group $Pnam(\sigma_1\,0\,0)00s$, in agreement with subsequent refinements of the modulated structure. The amplitudes of first-order harmonics of the displacive modulation functions of the C, N and O atoms were extracted from the electron density, and used as starting point for the refinement. The displacive modulation of hydrogen atoms was refined according to the riding model. Refinement of this modulated structure model against main and first-order satellite reflections resulted in R_F^{obs}(main) = 0.0817, R_F^{obs}(sat) = 0.5505 and wR_F^{all}(all) = 0.4843.

In the second step modulations were introduced for the occupancies of Ma and Mb. With small initial values for the modulation parameters, the refinement converged to R_F^{obs} (main) = 0.0616, R_F^{obs}(sat) = 0.1239 and wR_F^{all}(all) = 0.1180. The much better fit to the diffraction data demonstrates the importance of varying occupancies for the modulation. The average occupancies changed dramatically, resulting in Occ(Ma) = 0.279 (5) and Occ(Mb) = 0.221 (Figs. 5.2 and 5.3, and Table 5.4).

Thirdly, first-order harmonic modulation amplitudes were introduced for the displacements and rotations of the molecular orientations. Independent parameters are used for Ma and Mb, while those of Ma′ and Mb′ follow by symmetry. The fit to the diffraction data is improved at R_F^{obs}(main) = 0.0528, R_F^{obs}(sat) = 0.0882 and wR_F^{all}(all) = 0.0857. The resulting orientations are illustrated for four t values in Fig. 5.4. (see Tables C.1 and C.2 in Appendix C.1).

Table 5.4: Modulation parameters for the occupations of the two unique orientations of $[BF_4]^-$. $P^0(\mu)$ is the average occupancy, $P^s(\mu)$ the sine component and $P^c(\mu)$ the cosine component of the modulation function of orientation μ given by $p^\mu(\bar{x}_{s4}) = P^0(\mu) + P^s(\mu)\sin(2\pi\bar{x}_{s4}) + P^c(\mu)\cos(2\pi\bar{x}_{s4})$.

Molecule	$P^0(\mu)$	$P^s(\mu)$	$P^c(\mu)$
Ma	0.185(8)	-0.120(6)	0.150(9)
Mb	0.315(8)	-0.140(8)	0.139(9)

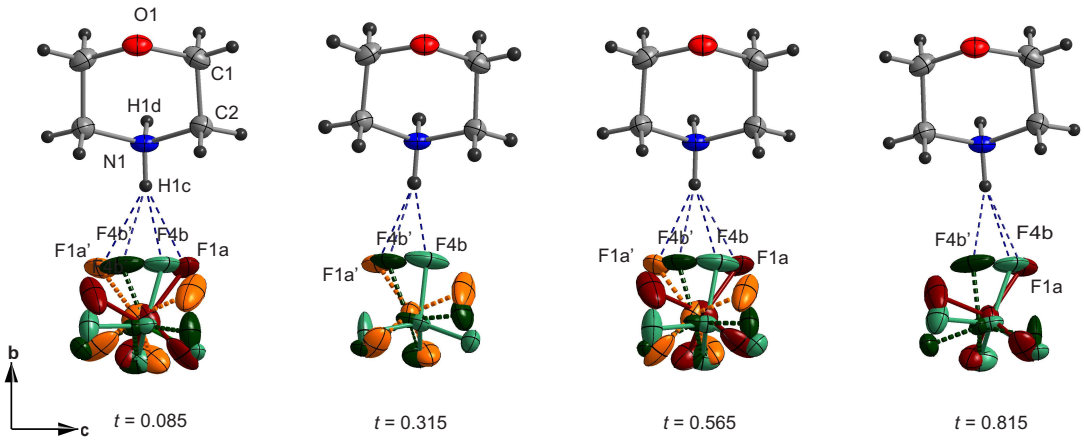

Figure 5.4: Hydrogen bonding between the morpholinium cation and the disordered anion $[BF_4]^-$. Hydrogen-bonded contacts in the modulated structure are shown at four values of t. Conformations of cationic molecule and orientations of $[BF_4]^-$ vary as a function of phase of modulation t.

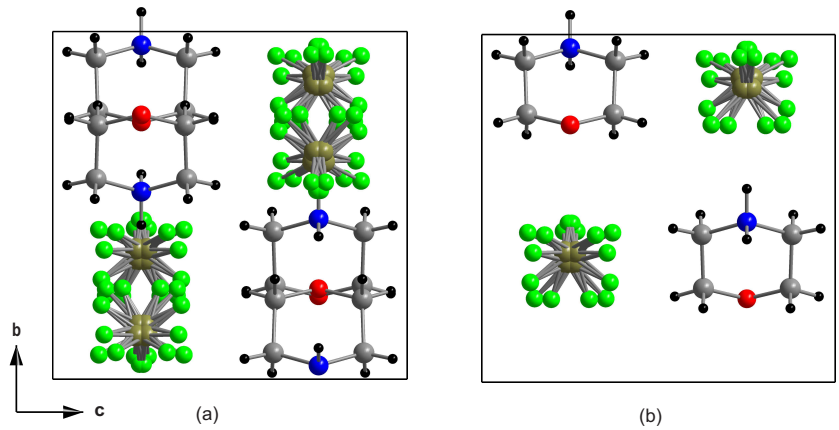

Figure 5.5: Crystal packing of morpholinium tetrafluoroborate (average structure). (a) Projection of one unit cell. (b) Projection of one pair of molecules ($0 < x < 1/2$). Blue= nitrogen, red= oxygen, gray= carbon, black= hydrogen, green indicates partially occupied atom sites of disordered $[BF_4]^-$.

Finally, a modulation was introduced for the TLS parameters. Due to large correlations in the refinements, the S tensors of TLS parameters set to zero. Again, a significant improvement of the fit to the data has been obtained, with R_F^{obs}(main) = 0.0519, R_F^{obs}(sat) = 0.0848 and wR_F^{all}(all) = 0.0818.

5.3 Discussion

Molecular packing in crystalline morpholinium tetrafluoroborate is similar within the whole range of temperatures 80–300 K. Compared to the Pnam structure at ambient conditions (Phase I; Szklarz et al. (2009)), the incommensurate (phase II; present work) and low-temperature (phase III; Owczarek et al. (2008)) phases incorporate small molecular and lattice distortions accompanying partial order of the orientations of $[BF_4]^-$ in phase II and complete order of $[BF_4]^-$ in phase III.

In agreement with the crystal structure of phase I (Szklarz et al., 2009), the average or basic structure of phase II can be described as a stacking along **c** of hydrogen-bonded molecular layers centered on mirror planes of *Pnam* (Fig. 5.5). The two layers per unit cell are equivalent to each other through the *n*–glide. Morpholinium cations are interconnected by N–H$\cdots$O hydrogen bonds to form molecular zigzag chains along **a** (Fig. 5.6). Cavities between the chains accommodate the fluoroborate anions. At higher temperatures, the cavities are larger than fluorob-

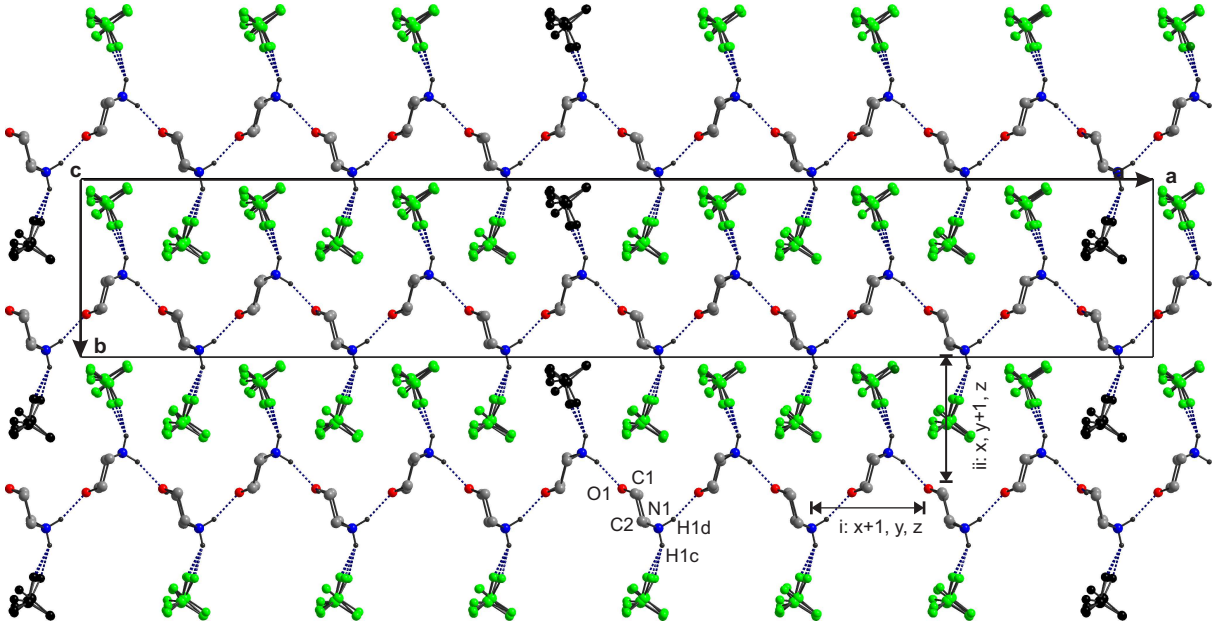

Figure 5.6: Crystal structure of phase II in the commensurate approximation as a sevenfold superstructure along **a**. One molecular layer ($0 < z < 1/2$) is shown in projection along **c**. Dashed lines indicate H1d$\cdots$O and H1c$\cdots$F hydrogen bonds. Multiple orientations are shown for the $[BF_4]^-$ anions (atoms in green). Black $[BF_4]^-$ anions mark sites where only three out of four orientations are present. Doubly pointed arrows connect molecules for which interatomic distances are given in Table 5.5 and Fig. 5.9.

Table 5.5: Interatomic distances (Å) between molecules connected by doubly pointed arrows in Fig. 5.6. Average, minimum (min) and maximum (max) values (Å) are given for the t dependence of interatomic distances. Standard uncertainties are given in parentheses.

Atom pair	Direction	Average	Min	Max	Max-Min
C1–C1	a	8.112(6)	7.930(6)	8.260(6)	0.312
C2–C2	a	8.112(6)	7.912(6)	8.280(6)	0.368
O1–O1	a	8.101(6)	8.095(6)	8.107(6)	0.01
N1–N1	a	8.097(6)	8.095(6)	8.099(6)	0.004
C1–C1	b	9.4092(14)	9.4092(14)	9.4092(14)	0.0
C2–C2	b	9.4092(13)	9.4092(13)	9.4092(13)	0.0
O1–O1	b	9.4092(10)	9.4092(10)	9.4092(10)	0.0
N1–N1	b	9.4092(10)	9.4092(10)	9.4092(10)	0.0
C1–C1	c	9.5492(15)	9.5492(15)	9.5492(15)	0.0
C2–C2	c	9.5492(13)	9.5492(13)	9.5492(13)	0.0
O1–O1	c	9.5492(13)	9.5492(13)	9.5492(13)	0.0
N1–N1	c	9.5492(11)	9.5492(11)	9.5492(11)	0.0

orate, thus explaining the orientational disorder of the ions (Szklarz et al., 2009). The diminished importance of entropy together with thermal expansion reducing the average size of the cavities on cooling explain the development of orientational order at lower temperatures.

The incommensurate modulation affects the positions and conformations of the morpholinium ions, while keeping a nearly rigid pattern of N–H$\cdots$O hydrogen bonds (Fig. 5.7). Displacements of all atoms along z reflect displacements of the molecular anion along **c** (Fig. 5.8). Displacements parallel to the planes are restricted to the carbon atoms [Fig. 5.8(a,b)]. They are responsible for conformational variations of the morpholinium anions. The length of the cavities along the chain direction is almost independent of t (Fig. 5.9) However, the modulation of the carbon atoms parallel to the planes do affect the shapes of the cavities, while the modulation of nitrogen (with attached hydrogen) will strongly affect the single, N–H$\cdots$F hydrogen bond between morpholinium and each individual orientation of fluoroborate.

The second part of the incommensurate modulation is a variation of the occupancies of the four different orientation of $[BF_4]^-$. Depending on the phase of the modulation, the occupancies of single orientations varies between 0 and 0.5, indicating a high degree of remaining disorder. Comparing t-plots shows that maxi-

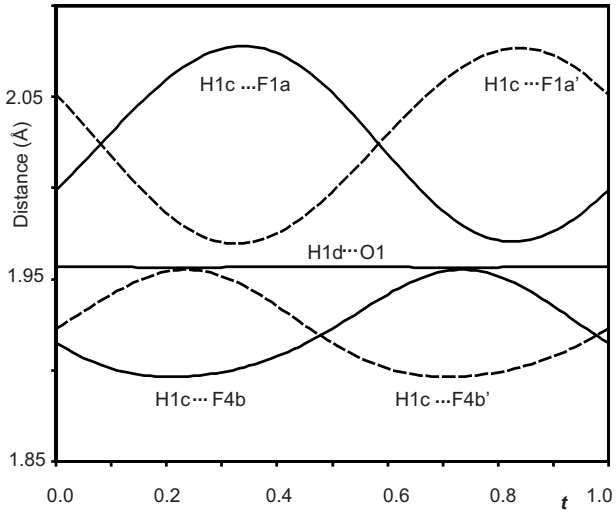

Figure 5.7: Distance (Å) as a function of t for H$\cdots$A in N–H$\cdots$O and N–H$\cdots$F hydrogen bonds. Compare to Table 5.6. Solid curves (F1a and F4b) and dashed curves (F1a′ and F4b′) are related by the mirror plane x, y, $-z+1/2$, $t+1/2$.

Table 5.6: Geometry of intermolecular hydrogen bonds (Å, deg).

D–H$\cdots$A	D–H		H$\cdots$A	D$\cdots$A	$\angle$D–H$\cdots$A
N1–H1c$\cdots$F1a	0.92	(max)	2.07(9)	2.823(13)	137.66
	0.92	(min)	1.98(9)	2.791(13)	147.40
N1–H1c$\cdots$F1a$'$	0.92	(max)	2.07	2.823(13)	137.66
	0.92	(min)	1.95	2.790(13)	145.35
N1–H1c$\cdots$F4b	0.92	(max)	1.95	2.74(2)	142.06
	0.92	(min)	1.90	2.66(2)	139.68
N1–H1c$\cdots$F4b$'$	0.92	(max)	1.95	2.73(2)	141.09
	0.92	(min)	1.90	2.66(2)	138.93
N1–H1d$\cdots$O1^{ii}	0.92	(max)	1.96	2.8516(12)	164.30
	0.92	(min)	1.96	2.8531(12)	164.10

Symmetry code: ^{ii} x, y+1, z

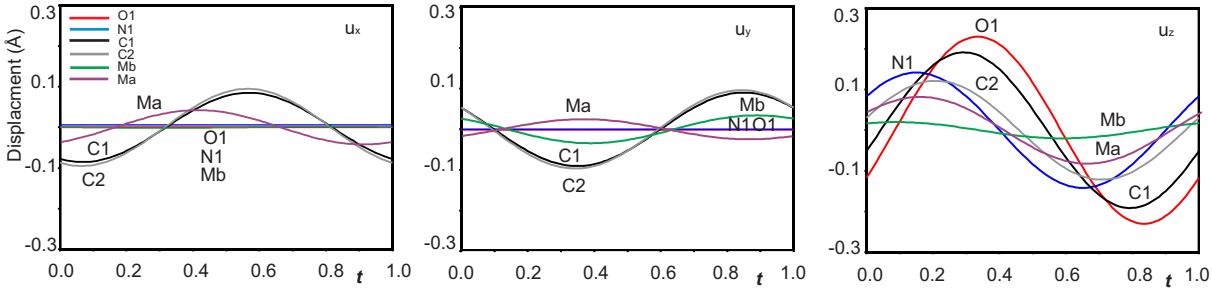

Figure 5.8: Displacement modulations (Å) of atoms of morpholinium and of the pseudo-rigid bodies Ma and Mb describing different orientations of $[BF_4]^-$.

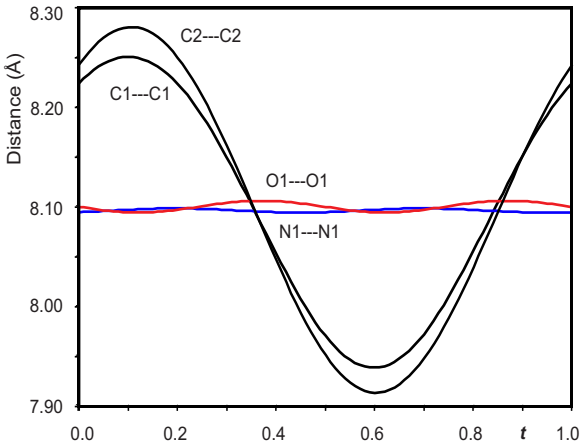

Figure 5.9: Interatomic distances (Å) between atoms of morpholinium ions neighboring along **a**. Compare Fig. 5.6.

mum occupancy of orientations Ma and Mb coincides with H$\cdots$F hydrogen–acceptor lengths close to the average H$\cdots$F length of $\sim$1.95 Å, *i.e.* the shortest hydrogen bond has its maximum value and the longest hydrogen bond has its minimum value at $t \approx 0.8$. Minimum occupancy correlates with environments corresponding to too short or too long hydrogen bonds (Figs. 5.3 and 5.7).

The observed contributions of all atoms to the modulation lead to a mechanism for the phase transition, whereby at low temperatures morpholinium ions are shaped around the fluoroborate ion, such as to optimize the interactions with one orientation of this ion. Packing forces between morpholinium ions prevent one optimal shape of cavities to be achieved, then leading to an incommensurately modulated structure of the crystal.

This mechanism is more complicated than a simple order-disorder phase transition proposed by Owczarek et al. (2011). They have measured the transition entropies of both phase transitions as $\Delta S_{exp}^{I-II} = 7.13$ J/mol·K and $\Delta S_{exp}^{II-III} = 4$ J/mol·K. It was noticed by Owczarek et al. (2011) that the sum of these two entropies is nearly equal to the difference in configurational entropy of $S_{conf} = R\ln[4] = 11.52$ J/mol·K for a fourfold disordered anion and the fully ordered state with $S_{conf} = R\ln[1] = 0$. Accordingly, it was suggested that the largest part of the orientational disorder would disappear at the transition from phase I to phase II.

We have computed the configurational entropy for phase II from its structure model. At each value of t the configurational entropy is obtained by the standard expression, employing the four different occupancies of $[BF_4]^-$ according to Fig. 5.3. The configurational entropy of the incommensurate phase then is defined as the average of this value over t. For the modulated occupancies at $T = 130$ K displayed in Fig. 5.3 a configurational entropy of $S_{conf}^{inc} = R\ln[3.23] = 9.75$ J/mol·K is obtained. The normal-to-incommensurate phase transition thus corresponds to $\Delta S_{conf}^{I-II} = 1.7$ J/mol·K, much lower than the experimental value reported by Owczarek et al. (2011). The small value of the change in configurational entropy indicates that most of the disorder remains in the incommensurate phase II. The change on configurational entropy (loss of disorder) cannot explain the much larger experimental transition entropy. This supports the interpretation that the phase transition is not a simple order-disorder transition, but that conformational changes of morpholinium play at least an equally important role.

5.4 Conclusions

A superspace structure model has been obtained for the incommensurately modulated crystal structure of morpholinium tetrafluoroborate crystal (phase II at $T = 130$ K). The superspace group indicates that inversion symmetry is preserved in phase II. Furthermore, the superspace group is in agreement with the second-order character of the phase transition I–II (Owczarek et al., 2011). Switching the modulation wave vector from incommensurate along $\mathbf{a}^*$ towards 1/3 along $\mathbf{c}^*$ imposes first-order character onto the transition II–III, in agreement with the measurements by Owczarek et al. (2011).

The incommensurate modulation involves both displacive modulations of morpholinium and occupational modulation of fluoroborate ions. The mechanism of the incommensurate phase transition involves a tendency of morpholinium ions to adapt their conformations such as to optimize the interactions with one orientation of the tetrafluoroborate ion. A tendency that is counteracted by packing forces between morpholinium ions preventing one optimal shape of cavities to be achieved, then leading to an incommensurately modulated structure of the crystal. Accordingly it could be shown that experimental transition entropies (Owczarek et al., 2011) cannot be explained by changes in the configurational entropy derived from partial order of tetrafluoroborate ions.

5.5 Acknowledgement

Single crystals were grown by Alfred Suttner at the Laboratory of Crystallography in Bayreuth. The research of L. N. has been made possible through financial support by the German Academic Exchange Service (DAAD) and Department of Equal Opportunities for Women of the University of Bayreuth.

Chapter 6

Summary

This thesis reports on phase transitions of hydrogen-bonded supramolecular crystals. Two compounds have been selected, namely phenazine–chloranilic acid $C_{18}H_{10}Cl_2N_2O_4$ (Phz-H_2ca) and morpholinium tetrafluoroborate $C_4NOH_{10}BF_4$ (MoB). Temperature-dependent x-ray diffraction has been used, in order to uncover the atomic mechanism of ferroelectricity in Phz-H_2ca, and to understand incommensurability in molecular crystals for both compounds. Single crystals of both compounds have been grown according to procedures published in the literature. X-ray diffraction experiments were done with synchrotron radiation on Phz-H_2ca, employing a four-circle *kappa* diffractometer and CCD area detector. X-ray diffraction on MoB was measured on a two-circle diffractometer with an image-plate area detector in the laboratory in Bayreuth, employing Mo-Kα radiation.

According to the literature, Phz-H_2ca is paraelectric (PE phase) at room temperature. Upon cooling, this material undergoes three phase transitions: paraelectric (PE) to ferroelectric (FE-I phase) at $T_c^I = 253$ K, FE-I to incommensurately modulated (FE-IC phase) at $T_c^{IC} = 147$ K, and finally a lock-in transition to a ferroelectric twofold superstructure (FE-II phase) at $T_c^{II} = 137$ K. The present study sought to find the mechanism of ferroelectricity and the origin of the incommensurability in Phz-H_2ca. Diffraction data were collected at T = 139 K (FE-IC) and at 100 K (FE-II). It was established that the non-centrosymmetric space group $P2_1$ of the FE-I phase is preserved as symmetry of the average structures at lower temperatures. The crystal structures of both the FE-IC and FE-II phases were successfully solved and refined within the superspace approach. The superspace group is $P2_1(\frac{1}{2}\,\sigma_2\,\frac{1}{2})0$, whith $\sigma_2 = 0.5139$ in the FE-IC and $\sigma_2 = \frac{1}{2}$ in the FE-II phases. Accurate crystal structures are reported for the FE-IC phase. One major result of the present work

is the determination of the exact locations of hydrogen atoms within the intermolecular O–H$\cdots$N hydrogen bonds. On the basis of the crystal structures, the following mechanism for the phase transitions is proposed. The phase transitions are related to proton transfer within the intermolecular O–H$\cdots$N hydrogen bonds. In the PE phase all hydrogen bonds are equivalent by symmetry. In the FE-IC phase, the modulation corresponds to an incommensurate variation between strong and very weak proton transfer. In the FE-II phase, full proton transfer is found in part of the hydrogen bonds O–H$\cdots$N, resulting in an alternation of neutral hydrogen-bonded chains and ionic hydrogen-bonded chains.

Morpholinium tetrafluoroborate (MoB) belongs to a series of hydrogen bonded ionic organometallic compounds with stoichiometry of ABX_4 and orthorhombic symmetry *Pnam*. According to the literature, MoB undergoes two phase transition upon cooling. At $T_{c1} = 153$ K an incommensurate phase (phase II) forms. Further cooling leads to a threefold superstructure (phase III) below $T_{c2} = 117$-118 K. Diffraction data have been collected at T = 160 K (phase I), T = 130 K (phase II) and T = 110 K (phase III). The basic structure of phase II has an orthorhombic lattice close to the lattice of phase I at higher temperatures. The symmetry of phase II is described by the orthorhombic superspace group $Pnam(\sigma_1\,0\,0)00s$. The incommensurate modulation wavevector at T = 130 K is found as $\mathbf{q} = (\sigma_1\ , 0, 0)$ with $\sigma_1 = 0.4126$. A structure model for phase I is developed on the basis of $[BF_4]^-$ described as a pseudo-rigid body that is then placed in four orientations, in order to describe the disorder of this anion. This model is in accordance with the crystal structure in the literature. The incommensurate modulation of phase II is found to involve a modulation of occupancies of the four orientations of $[BF_4]^-$, correlated with displacements of the morpholinium cations. $[BF_4]^-$ in phase III is fully ordered. The proposed mechanism for the phase transitions involves the notion of entropy becoming less important at lower temperatures, while thermal expansion leads to tighter cavities for $[BF_4]^-$, and morpholinium adapts its conformations to fit to one of the four orientations of $[BF_4]^-$. It is shown that the incommensurate phase transition is not driven by a change to the configurational entropy, and that the computed changes of the configurational entropy do not explain the measured transition entropies.

Chapter 7

Zusammenfassung

Diese Doktorarbeit berichtet über Phasenübergänge in supramolekularen Kristallen mit Wasserstoffbrückenbindungen. Zwei Verbindungen wurden ausgewählt. Diese sind zum einen Phenazin-Chloranilsäure $C_{18}H_{10}Cl_2N_2O_4$ (Phz-H_2ca) und zum andern Morpholinum-tetrafluoroboat $C_4NOH_{10}BF_4$ (MoB). Um den atomaren Mechanismus der Ferroelektriziät in Phz-H_2ca aufzuklären und die Inkommensurabilität in beiden Verbindungen zu verstehen, wurden temperaturabhängige Röntgenbeugungsexperimente durchgeführt. Einkristalle von beiden Verbindungen wurden nach literaturbekannten Vorschriften gezüchtet. Phz-H_2ca wurde am Synchrotron an einem Vierkreis-*Kappa*-Diffraktometer mit CCD-Flächendetektor untersucht. Die Röntgenbeugung von MoB wurde an einem Zweikreis-Difraktometer mit einer Imageplate und mithilfe von Mo-Kα-Strahlung im Labor des Lehrstuhls für Kristallographie in Bayreuth gemessen.

Der Literatur entsprechend ist Phz-H_2ca bei Zimmertemperatur paraelektrisch (PE-Phase). Durch Abkühlen erfährt dieses Material drei Phasenübergänge: paraelektrisch (PE) zu ferroelektrisch (FE-I-Phase) bei T_c^I = 253 K, FE-I zu inkommensurabel moduliert (FE-IC-Phase) bei T_c^{IC} = 147 K, und letztendlich ein Lock-in-Übergang zu einer ferroelektrischen zweifachen Überstruktur (FE-II-Phase) bei T_c^{II} = 137 K. Die vorliegende Studie versucht den Mechanismus der Ferroelektrizität und den Ursprung der Inkommensurabilität in Phz-H_2ca aufzuklären. Die Beugungsdaten wurden bei T = 139 K (FE-IC) und 100 K (FE-II) aufgenommen. Es wurde herausgefunden, dass die nichtzentrosymmetrische Raumgruppe $P2_1$ der FE-I-Phase in der gemittelten Strutur bei tieferer Temperatur erhalten bleibt. Die Kristallstrukturen der beiden Phasen (FE-IC and FE-II) konnten erfolgreich mittels der Superraummethode gelöst und verfeinert werden. Die Superraumgruppe ist $P2_1(\frac{1}{2}\,\sigma_2\,\frac{1}{2})0$,

mit $\sigma_2 = 0.5139$ in der FE-IC und $\sigma_2 = \frac{1}{2}$ in der FE-II-Phase. Genaue Kristallstrukturen wurden von der FE-IC-Phase berichtet. Ein wesentliches Ergebnis dieser Arbeit ist die Bestimmung der exakten Position der Wasserstoffatome in den intermolkularen Wasserstoffbrückenbindungen. Basierend auf den vorliegenden Kristallstrukturen wird der folgende Mechanismus vorgeschlagen. Den Phasenübergängen liegt ein Protonentransfer zwischen intermolekularen O–H$\cdots$N-Wasserstoffbrückenbingen zugrunde. In der PE-Phase sind alle Wasserstoffbrückenbingen symmetrieäquivalent. In der FE-IC-Phase basiert die Modulation auf einer inkommensurablen Veränderung zwischen schwachem und starkem Protontransfer. In der FE-II-Phase wurde in einem Teil der O–H$\cdots$N-Wasserstofbrückenbindungen ein kompletter Protonentransfer gefunden, wodurch sich neutrale und ionische Wasserstofbrücken entlang einer Kette abwechseln.

Morpholinum-tetrafluoroboat (MoB) gehört zu einer Gruppe von wasserstoffverbrückten organometallischen Verbindungen mit einer ABX_4-Stöchiometrie und einer orthorhombischen *Pnam*-Symmetrie. Literaturgemäß erfährt MoB beim Abkühlen zwei Phasenübergänge. Bei $T_{c1} = 153$ K bildet siche eine inkommensurable Phase (II). Weiteres Abkühlen führt zu einer dreifachen Überstrukturphase (III) unterhalb von $T_{c2} = 117$-118 K. Beugungsdaten wurden bei T = 160 K (Phase I), T = 130 K (Phase II) und T = 110 K (Phase III) aufgenommen. Die Basisstruktur von Phase II hat ein orthorhomisches Gitter sehr ähnlich dem Gitter der Phase I bei höheren Temperaturen. Die Symmetrie der Phase II wird durch the orthorhombische Superraumgruppe $Pnam(\sigma_1\,0\,0)00s$ beschrieben. Der incommensurable Modulationswellenvektor bei T = 130 K wurde als $\mathbf{q} = (\sigma_1\ , 0, 0)$ mit $\sigma_1 = 0.4126$ gefunden. Das Strukturmodel von Phase I wurde mit einem $[BF_4]^-$-Anion beschrieben als pseudo starrem Gerüst, weches dann in vier verschingenen Lagen eingefügt wurde, um die Fehlordnung zu beschreiben, entwickelt. Dieses Modell stimmt mit dem der Literatur beschiebenen Kistallstruktur überein. In der inkommensurablen Modulation von Phase II wurde eine Besetztungsmodulation von $[BF_4]^-$ gefunden welche mit einer Verschiebungsmodulation der Morpholinumkationen einhergeht. $[BF_4]^-$ in Phase III ist vollständig geordnet. In dem vorgeschlagenen Mechanismus für die Phasenübergänge beinhaltet ein geringerer Einfluss der Entropie bei gerinerer Temperutur, während thermische Ausdehnung zu engeren Kavitäten für $[BF_4]^-$ führt. Die Konformation vom Morpholinum passt sich den vier verschiedenen Lagen von $[BF_4]^-$ an. Es wurde gezeigt, das der inkommensurable Phasenübergang nicht durch die Entropieänderung gesteuert wird, und dass die berechneten Änderungen der Konformationsentropie nicht die gemessenen Übergangsentropien erklären.

Appendix A

Incommensurate phenazine–chloranilic acid

A.1 Structural parameters of model A

Table A.1: Fractional atomic coordinates (x, y, z) and amplitudes of the displacement modulation functions (in Å) of model A. Standard uncertainties are given in parentheses.

Atom	x	y	z	$A_x \times a$	$A_y \times b$	$A_z \times c$	$B_x \times a$	$B_y \times b$	$B_z \times c$
Cl2	0.39426(2)	0.7594	0.425664(9)	0.0027(4)	0.0000	0.0064(3)	-0.0019(4)	-0.0108(3)	0.0012(3)
Cl1	0.10334(2)	1.36699(6)	0.076472(9)	-0.0235(7)	-0.0042(3)	0.0044(5)	-0.0197(9)	-0.0002(3)	0.0023(3)
O1	0.01710(6)	1.0198(3)	0.20084(4)	0.0032(11)	0.0045(1)	-0.0032(13)	-0.0088(11)	-0.0320(1)	0.0069(10)
O2	0.47869(6)	1.1115(3)	0.30175(3)	-0.0354(11)	0.0158(1)	-0.0067(10)	0.0135(16)	-0.0128(1)	0.0016(10)
O3	0.14288(6)	0.7382(3)	0.34754(4)	0.0042(10)	0.0124(2)	-0.0025(12)	-0.0004(10)	-0.0399(1)	0.0043(10)
O4	0.35598(6)	1.3761(3)	0.15557(3)	-0.0174(10)	0.0087(1)	0.0170(10)	0.0069(12)	-0.0113(1)	-0.0010(12)
N1	0.85572(7)	0.6962(3)	0.24458(4)	0.0111(12)	0.0034(1)	0.0293(12)	0.0030(12)	0.0030(1)	-0.0012(15)
N2	0.64611(7)	0.4400(3)	0.25095(4)	-0.0027(14)	0.0015(1)	0.0093(13)	-0.0214(12)	0.0000(1)	0.0043(12)
C1	0.30168(9)	1.2333(3)	0.19627(4)	-0.0437(15)	0.0041(1)	0.0042(13)	-0.0036(21)	-0.0034(1)	0.0003(15)
C2	0.18097(9)	1.2022(3)	0.17186(4)	-0.0191(15)	0.0011(1)	0.0032(13)	-0.0095(16)	-0.0019(1)	0.0022(13)
C3	0.12546(9)	1.0428(3)	0.22157(4)	-0.0104(20)	-0.0019(1)	0.0040(15)	-0.0414(16)	-0.0132(1)	0.0027(13)
C4	0.19362(9)	0.8866(3)	0.30527(4)	0.0022(15)	-0.0030(2)	0.0079(15)	-0.0126(17)	-0.0173 (1)	0.0040(15)
C5	0.31591(8)	0.9219(3)	0.33025(4)	-0.0140(16)	-0.0038(1)	0.0091(13)	-0.0171(15)	-0.0098(1)	0.0020(13)
C6	0.36782(8)	1.0814(3)	0.27986(4)	-0.0334(15)	0.0041(1)	0.0027(13)	-0.0054(19)	-0.0053(1)	0.0007(13)
C7	0.81178(9)	0.5094(3)	0.10230(4)	0.0032(15)	-0.0147(1)	0.0252(17)	-0.0071(15)	0.0026(1)	0.0070(17)
C8	0.73694(9)	0.3530(3)	0.03492(4)	0.0084(15)	-0.0166(1)	-0.0039(17)	0.0028(15)	-0.0060(1)	0.0059(13)
C9	0.63221(9)	0.2204(3)	0.03867(4)	0.0079(15)	-0.0056(1)	-0.0185(15)	0.0069(15)	-0.0075(1)	0.0031(15)

Continued on next page.

Continued from previous page.

Atom	x	y	z	$A_x \times a$	$A_y \times b$	$A_z \times c$	$B_x \times a$	$B_y \times b$	$B_z \times c$
C10	0.60119(9)	0.2457(3)	0.10984(4)	-0.0009(15)	-0.0045(1)	-0.0187(13)	-0.0153(15)	-0.0008(1)	0.0020(15)
C11	0.67723(9)	0.4113(3)	0.18154(4)	-0.0062(17)	-0.0026 (1)	0.0035(17)	-0.0142(15)	0.0015(1)	0.0052(13)
C12	0.78295(8)	0.5441(3)	0.17721(4)	-0.0090(15)	-0.0011(1)	0.0269(17)	-0.0046(15)	0.0038(1)	0.0062(17)
C13	0.69135(9)	0.6285(3)	0.39302(4)	-0.0146(15)	0.0038(1)	0.0214(13)	0.0014(15)	0.0011(1)	-0.0006(15)
C14	0.76521(9)	0.7854(3)	0.46057(4)	-0.0145(15)	-0.0072(1)	0.0135 (15)	0.0148(15)	0.0056(1)	-0.0049(15)
C15	0.87021(9)	0.9210(3)	0.45697(5)	0.0000 (15)	-0.0038(1)	0.0008(17)	0.0090(16)	0.0132(1)	-0.0059(15)
C16	0.90122(9)	0.8951(3)	0.38591(5)	-0.0010(16)	-0.0049(1)	0.0056(15)	0.0235(17)	0.0151(1)	-0.0051(15)
C17	0.82595(9)	0.7284(3)	0.31464(4)	-0.0131(16)	-0.0030(1)	0.0125(15)	0.0121(15)	0.0034(1)	-0.0008(15)
C18	0.71946(9)	0.5983(3)	0.31757(4)	-0.0209(15)	0.0030(1)	0.0155(13)	-0.0047(16)	0.0019(1)	0.0007(15)
H1o1	-0.0461(11)	0.765(4)	0.2321(8)	0.1868(15)	0.0527(1)	0.0168(15)	-0.0792(15)	-0.0113(2)	0.0075(13)
H1o2	0.5251(11)	1.158(4)	0.2704(8)	-0.0074(15)	0.0151(1)	-0.0101(15)	0.0000(15)	-0.0113(1)	-0.0064(15)
H7	0.8834	0.5955	0.0992	0.0062	-0.0211	0.0471	-0.0074	0.0098	0.0038
H8	0.7558	0.3327	-0.0161	0.0087	-0.0248	-0.0067	0.0099	-0.0079	0.0064
H9	0.5814	0.1096	-0.0098	-0.0012	0.0011	-0.0219	0.0161	-0.0136	-0.0004
H10	0.5296	0.1537	0.1115	0.0074	-0.0030	-0.0168	-0.0210	0.0064	-0.0023
H13	0.6202	0.5382	0.3962	-0.0148	0.0053	0.0185	-0.0074	0.0053	0.0011
H14	0.7459	0.8045	0.5115	-0.0161	-0.0072	0.0067	0.0173	0.0090	-0.0053
H15	0.9207	1.0334	0.5054	0.0012	0.0072	-0.0135	0.0025	0.0196	-0.0053
H16	0.9727	0.9881	0.3842	0.0111	0.0041	-0.0050	0.0186	0.0188	-0.0056

Table A.2: Anisotropic atomic displacement parameters (anisotropic ADPs) U_{ij} of model A. For each atom are given the basic-structure value (first line), the sine amplitude of the first-harmonic modulation function (sin; second line), and the cosine amplitude (cos; third line). Standard uncertainties are given in parentheses.

Atom		U_{11}	U_{22}	U_{33}	U_{12}	U_{13}	U_{23}
Cl2		0.01737(18)	0.01914(12)	0.01152(7)	-0.00017(11)	0.00280(9)	0.00293(6)
	sin	0.0032(2)	-0.00022(16)	0.00007(18)	0.00000(15)	0.00024(17)	0.00049(11)
	cos	0.0021(2)	-0.00196(17)	-0.00069(18)	0.00006(14)	-0.00065(16)	0.00021(11)
Cl1		0.01772(18)	0.01883(12)	0.01129(7)	0.00005(11)	0.00285(9)	0.00285(6)
	sin	0.0017(2)	-0.00089(16)	-0.00044(17)	-0.00150(17)	-0.00058(16)	0.00029(12)
	cos	-0.0007(2)	-0.00023(16)	-0.00047(18)	-0.00050(17)	-0.00097(17)	0.00067(11)
O1		0.0117(4)	0.0259(4)	0.0183(2)	-0.0023(4)	0.0042(3)	0.0039(3)
	sin	0.0026(7)	0.0004(5)	-0.0007(6)	0.0002(4)	0.0012(5)	0.0001(4)
	cos	0.0037(7)	-0.0035(6)	0.0001(6)	-0.0010(4)	0.0010(5)	0.0020(4)
O2		0.0132(4)	0.0253(4)	0.0169(2)	-0.0030(4)	0.0056(3)	0.0055(3)
	sin	0.0001(7)	0.0037(5)	0.0002(6)	-0.0028(5)	-0.0007(5)	-0.0008(4)
	cos	0.0009(7)	-0.0024(5)	-0.0004(6)	0.0002(4)	-0.0002(5)	0.0008(4)
O3		0.0167(4)	0.0272(4)	0.0177(2)	-0.0030(5)	0.0081(3)	0.0054(3)
	sin	-0.0025(7)	0.0019(6)	0.0002(6)	0.0008(4)	0.0008(5)	0.0003(4)
	cos	0.0055(7)	-0.0061(6)	-0.0011(6)	0.0007(5)	0.0001(5)	0.0029(4)
O4		0.0160(4)	0.0254(4)	0.0165(2)	-0.0021(5)	0.0067(3)	0.0054(3)
	sin	0.0002(7)	0.0019(5)	-0.0009(6)	-0.0007(5)	0.0003(5)	0.0012(4)
	cos	0.0013(7)	-0.0011(6)	-0.0002(6)	0.0012(4)	0.0018(5)	-0.0007(4)
N1		0.0132(5)	0.0140(3)	0.0123(2)	0.0001(4)	0.0029(3)	0.0007(2)
	sin	-0.0004(8)	0.0000(5)	-0.0016(6)	-0.0002(5)	-0.0029(6)	0.0022(4)
	cos	-0.0024(8)	0.0013(5)	-0.0001(6)	-0.0012(5)	-0.0016(6)	-0.0014(4)
N2		0.0133(5)	0.0142(3)	0.0127(2)	-0.0009(4)	0.0037(3)	0.0005(2)
	sin	0.0020(8)	-0.0005(5)	0.0005(6)	-0.0003(5)	0.0002(6)	0.0005(4)
	cos	-0.0007(7)	0.0005(5)	-0.0001(6)	-0.0015(5)	-0.0019(5)	0.0016(4)
C1		0.0165(6)	0.0137(4)	0.0114(2)	-0.0004(5)	0.0044(3)	0.0002(3)
	sin	0.0107(10)	0.0011(6)	-0.0032(7)	-0.0030(6)	-0.0016(7)	0.0006(4)
	cos	-0.0030(10)	-0.0001(6)	0.0004(7)	0.0006(6)	-0.0010(7)	-0.0003(4)
C2		0.0144(6)	0.0152(4)	0.0107(2)	-0.0016(4)	0.0035(3)	0.0005(2)
	sin	-0.0024(10)	0.0019(6)	-0.0020(7)	-0.0020(6)	-0.0024(7)	-0.0002(4)
	cos	-0.0025(9)	-0.0001(6)	-0.0004(7)	0.0004(6)	-0.0013(7)	0.0009(4)
C3		0.0145(6)	0.0152(4)	0.0122(2)	-0.0001(5)	0.0039(3)	0.0000(3)
	sin	0.0014(10)	0.0000(6)	-0.0009(8)	-0.0020(6)	-0.0001(7)	0.0005(5)
	cos	0.0026(10)	-0.0031(6)	-0.0002(7)	-0.0029(6)	0.0004(7)	0.0010(4)
C4		0.0143(6)	0.0150(4)	0.0120(2)	-0.0011(5)	0.0050(3)	-0.0004(3)
	sin	0.0006(9)	0.0001(6)	0.0012(7)	0.0022(6)	0.0020(7)	-0.0003(5)
	cos	0.0042(10)	-0.0029(7)	-0.0015(8)	-0.0015(6)	-0.0016(7)	0.0003(4)
C5		0.0125(6)	0.0137(4)	0.0110(2)	-0.0009(4)	0.0029(3)	0.0007(2)
	sin	-0.0053(9)	-0.0006(6)	0.0021(7)	0.0016(6)	0.0004(7)	0.0030(4)
	cos	-0.0004(9)	-0.0005(6)	-0.0015(7)	-0.0010(6)	-0.0005(6)	-0.0003(4)
C6		0.0110(6)	0.0137(4)	0.0118(2)	-0.0009(4)	0.0028(3)	0.0002(2)
	sin	0.0030(9)	0.0002(6)	0.0003(7)	-0.0023(6)	-0.0003(7)	0.0008(4)
	cos	0.0059(10)	-0.0002(6)	-0.0011(7)	0.0007(5)	-0.0005(7)	0.0008(4)

Continued on next page.

Continued from previous page.

Atom		U_{11}	U_{22}	U_{33}	U_{12}	U_{13}	U_{23}
C7		0.0159(6)	0.0159(4)	0.0142(3)	-0.0004(5)	0.0051(3)	-0.0009(3)
	sin	0.0032(10)	-0.0017(6)	-0.0005(7)	0.0001(6)	-0.0012(7)	0.0022(5)
	cos	0.0021(9)	-0.0011(6)	0.0007(7)	0.0016(6)	-0.0005(7)	0.0020(5)
C8		0.0187(6)	0.0179(4)	0.0139(2)	0.0045(5)	0.0055(3)	0.0000(3)
	sin	0.0037(11)	-0.0040(7)	0.0009(8)	-0.0013(6)	0.0009(7)	-0.0001(5)
	cos	0.0002(10)	-0.0024(6)	0.0020(7)	-0.0012(6)	0.0009(7)	0.0030(5)
C9		0.0166(6)	0.0165(4)	0.0138(3)	0.0015(5)	0.0022(3)	-0.0020(3)
	sin	0.0048(10)	0.0002(6)	-0.0014(8)	-0.0003(6)	0.0009(7)	-0.0007(5)
	cos	0.0142(10)	-0.0009(6)	-0.0038(8)	0.0013(6)	0.0024(7)	0.0006(5)
C10		0.0148(6)	0.0164(4)	0.0137(2)	-0.0047(5)	0.0023(3)	-0.0020(3)
	sin	-0.0042(9)	0.0009(6)	-0.0004(7)	-0.0022(6)	-0.0014(7)	-0.0020(5)
	cos	-0.0011(10)	0.0003(6)	-0.0004(8)	0.0012(6)	-0.0034(7)	0.0024(5)
C11		0.0161(6)	0.0119(4)	0.0118(2)	0.0000(4)	0.0028(3)	0.0008(2)
	sin	0.0037(11)	-0.0007(6)	0.0003(8)	-0.0011(5)	-0.0007(7)	-0.0005(4)
	cos	-0.0014(9)	0.0000(6)	-0.0008(7)	-0.0008(6)	0.0000(6)	0.0021(4)
C12		0.0112(5)	0.0127(4)	0.0130(2)	0.0023(4)	0.0038(3)	0.0018(2)
	sin	0.0023(9)	-0.0002(6)	-0.0006(7)	-0.0002(5)	0.0001(6)	0.0018(4)
	cos	0.0015(9)	0.0004(6)	0.0007(7)	-0.0022(5)	-0.0005(7)	0.0014(4)
C13		0.0159(6)	0.0180(4)	0.0135(2)	0.0018(5)	0.0060(3)	0.0012(3)
	sin	0.0045(10)	0.0005(6)	-0.0020(7)	0.0004(6)	-0.0011(7)	0.0016(5)
	cos	-0.0003(9)	0.0007(7)	0.0000(7)	-0.0013(6)	-0.0003(7)	0.0002(5)
C14		0.0200(6)	0.0177(4)	0.0143(3)	0.0006(5)	0.0057(3)	-0.0027(3)
	sin	-0.0021(10)	-0.0015(7)	-0.0002(8)	-0.0022(6)	-0.0019(7)	0.0012(5)
	cos	-0.0012(10)	-0.0008(6)	0.0024(8)	-0.0023(6)	0.0019(7)	-0.0014(5)
C15		0.0160(6)	0.0168(4)	0.0143(3)	0.0002(5)	0.0024(3)	-0.0028(3)
	sin	-0.0004(9)	0.0002(6)	-0.0020(7)	0.0017(6)	-0.0018(7)	-0.0007(5)
	cos	0.0044(11)	0.0025(6)	-0.0004(8)	0.0021(6)	0.0010(7)	-0.0010(5)
C16		0.0126(6)	0.0144(4)	0.0144(2)	0.0010(5)	0.0009(3)	-0.0006(3)
	sin	0.0023(8)	-0.0013(6)	0.0000(7)	-0.0005(6)	-0.0007(6)	0.0001(5)
	cos	-0.0013(11)	0.0014(6)	0.0017(8)	0.0011(5)	0.0009(7)	-0.0012(4)
C17		0.0144(6)	0.0124(4)	0.0124(2)	0.0018(4)	0.0050(3)	0.0009(2)
	sin	0.0049(9)	-0.0011(6)	-0.0005(7)	-0.0002(6)	0.0007(7)	0.0012(4)
	cos	-0.0060(9)	0.0003(6)	0.0011(7)	0.0032(5)	-0.0014(7)	0.0001(4)
C18		0.0151(6)	0.0117(4)	0.0117(2)	-0.0009(4)	0.0023(3)	0.0007(2)
	sin	0.0015(9)	-0.0001(6)	-0.0012(7)	-0.0013(5)	-0.0005(7)	0.0021(4)
	cos	-0.0001(9)	0.0010(6)	-0.0009(7)	-0.0012(6)	0.0000(6)	0.0005(4)

A.2 Modulation of the acidic hydrogen atoms

The difference Fourier map obtained after the final refinement of model A reveals maxima on the covalent bonds (Fig. A.1). Apparently, the resolution of the diffraction data (Table 1 in the main text) was sufficient to obtain the reorganisation of electron density due to chemical bonding. Nevertheless, the resolution of the diffraction data is worse and the temperature of the crystal is higher than is generally accepted as necessary for a multipole refinement. Furthermore, software is not available for multipole refinements of modulated structures. Therefore, we present model A in the independent-atom approximation as the best model that we have been able to achieve.

Similarly to covalent bonds, the difference Fourier map reveals density at lone pairs of oxygen atoms. This density interferes with the density of the modulated hydrogen atoms. Nevertheless, the difference Fourier map obtained after refinement of a model without the acidic hydrogen atoms clearly shows positive density near O2 of the O2–H1o2$\cdots$N2 hydrogen bond, which is well described by introducing a virtually non-modulated hydrogen atom. See top row *vs* bottom row in Fig. A.2. The remaining density near O2 in the difference Fourier map of model A will represent the lone pair of O2.

Sections through the O1–H1o1$\cdots$N1 hydrogen bond of the same two difference Fourier maps reveal density close to N1 for $t = 0.31$ and density close to O1 for $t = 0.85$ (bottom row in Fig. A.3). This density is well described by the modulated positions of H1o1 hydrogen atom, while the remaining density near O1 in the difference Fourier map of model A should be interpreted as the lone pair of O1.

Table A.3: Bond lengths (Å) for bonds between non-hydrogen atoms in model A. Standard uncertainties are given in parentheses.

Bond	Mean	Min.	Max.	Max-Min
Cl2-C5	1.7153(15)	1.7131(15)	1.7178(15)	0.0047
Cl1-C2	1.7155(15)	1.7119(15)	1.7190(15)	0.0071
O1-C3	1.281(2)	1.251(2)	1.311(2)	0.060
O2-C6	1.312(3)	1.310(2)	1.314(2)	0.004
O3-C4	1.219(2)	1.215(2)	1.223(2)	0.008
O4-C1	1.221(2)	1.208(2)	1.234(2)	0.026
C1-C2	1.428(3)	1.406(3)	1.449(3)	0.043
C1-C6	1.508(2)	1.505(2)	1.510(2)	0.005
C2-C3	1.372(3)	1.349(3)	1.396(3)	0.047
C3-C4	1.522(2)	1.507(2)	1.537(2)	0.030
C4-C5	1.447(3)	1.438(3)	1.456(3)	0.018
C5-C6	1.351(3)	1.346(3)	1.356(3)	0.010
N1-C12	1.342(2)	1.339(2)	1.345(2)	0.006
N1-C17	1.344(2)	1.342(2)	1.347(2)	0.005
N2-C11	1.342(2)	1.338(2)	1.345(2)	0.007
N2-C18	1.3470(19)	1.342(2)	1.352(2)	0.010
C7-C8	1.360(2)	1.355(2)	1.364(2)	0.009
C7-C12	1.417(3)	1.415(3)	1.420(3)	0.005
C8-C9	1.408(3)	1.403(3)	1.413(3)	0.010
C9-C10	1.368(3)	1.364(3)	1.373(3)	0.009
C10-C11	1.427(2)	1.420(2)	1.434(2)	0.014
C11-C12	1.423(3)	1.420(3)	1.426(3)	0.006
C13-C14	1.357(2)	1.351(2)	1.363(2)	0.012
C13-C18	1.420(3)	1.417(3)	1.423(3)	0.006
C14-C15	1.414(3)	1.405(3)	1.424(3)	0.019
C15-C16	1.367(3)	1.361(3)	1.372(3)	0.011
C16-C17	1.420(2)	1.417(2)	1.424(2)	0.007
C17-C18	1.421(3)	1.417(3)	1.424(3)	0.007

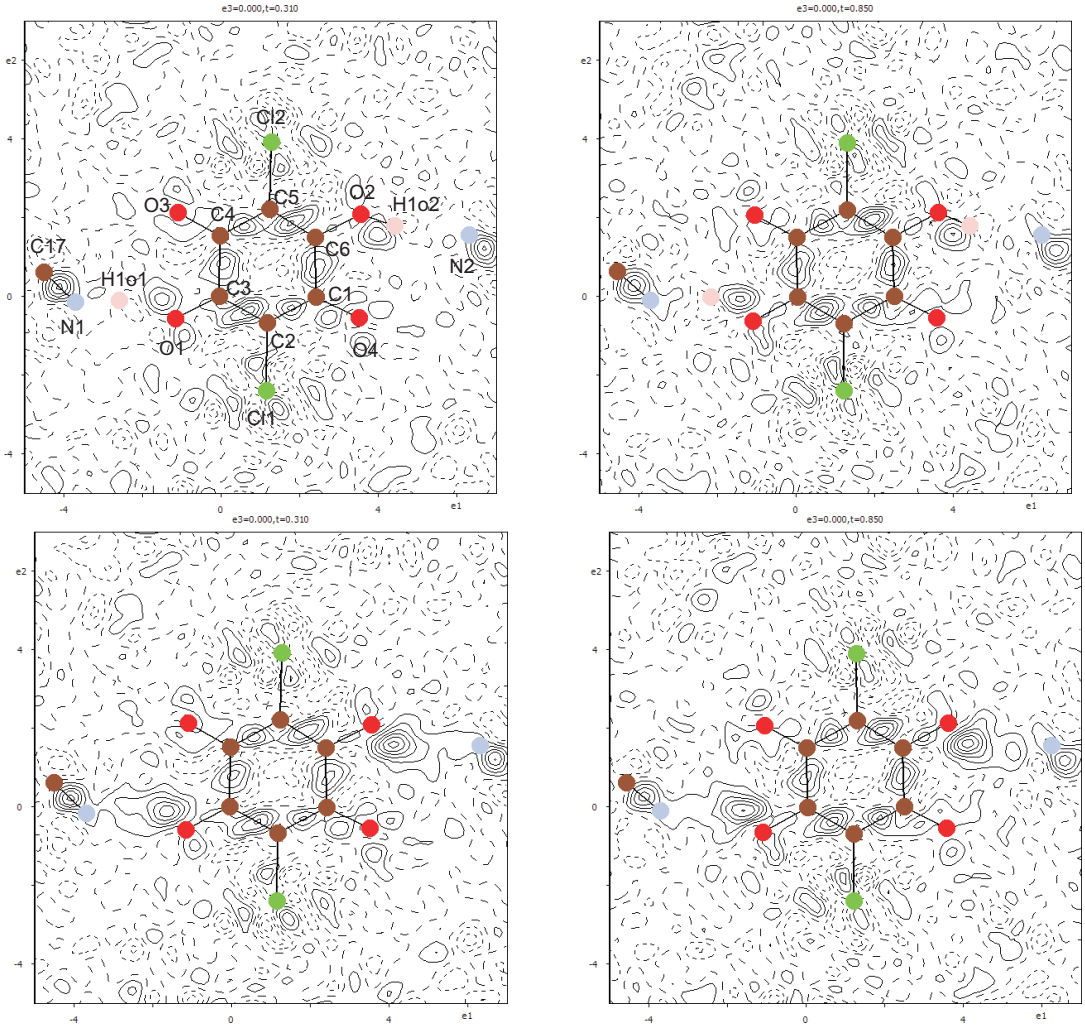

Figure A.1: Difference Fourier maps showing a section of 12×12 Å^2 in the plane through the atoms C1—C3—C5 of the chloranilic acid ring.
Top row: model A.
Bottom row: model A without the acidic hydrogen atoms.
Left: section $t = 0.31$ corresponding to a maximum of the distance O1–H1o1 (*cf* Fig. 3 in the main text).
Right: section $t = 0.85$ corresponding to a minimum of the distance O1–H1o1.
Positive contours (solid lines), negative contours (dotted lines) and the zero contour (dashed lines) are drawn at intervals of 0.1 electrons/Å^3. Coloured circles are the projected positions of atoms that appear within 0.42 Å from the plane.

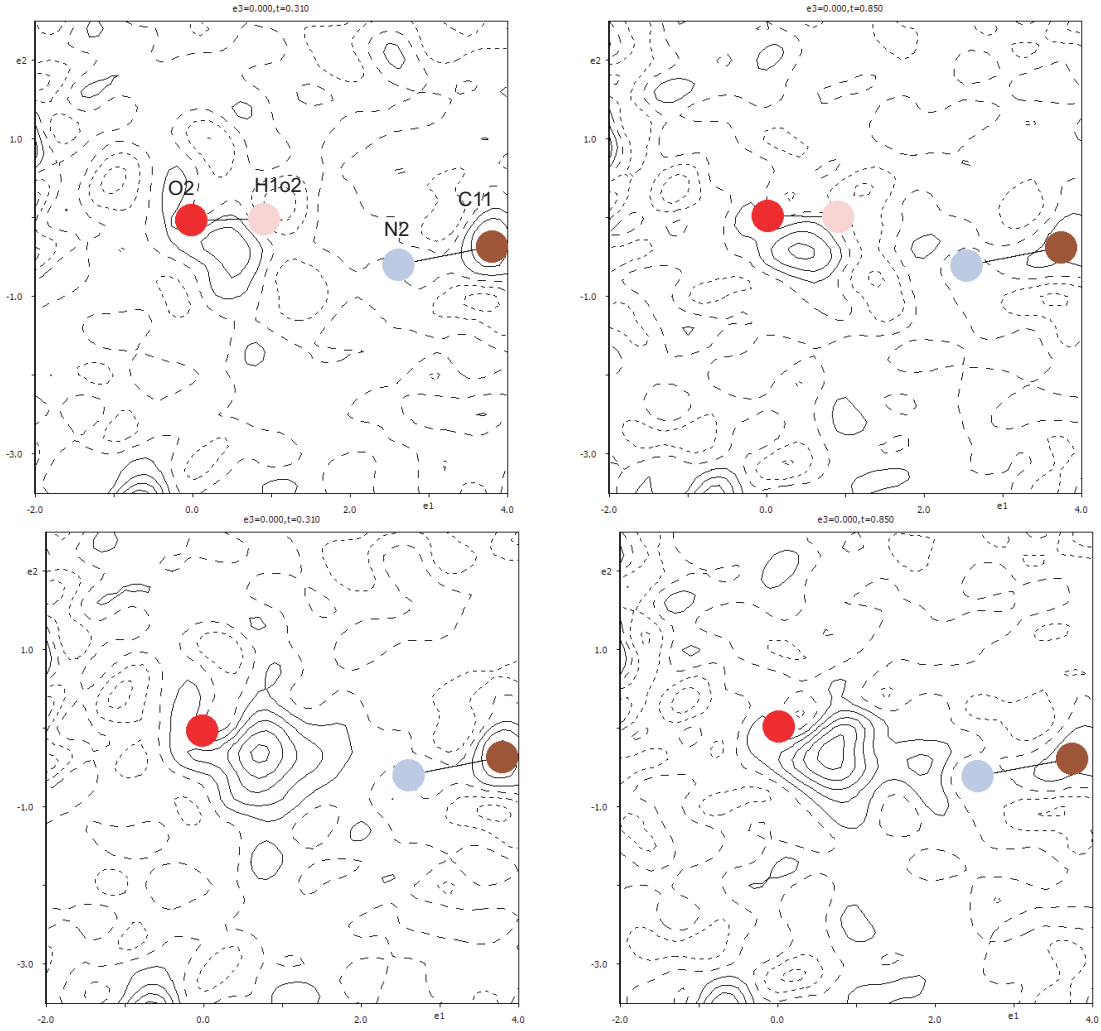

Figure A.2: Difference Fourier maps showing a section of 6×6 Å^2 in the plane through the hydrogen bond defined by the atoms O2—H1o2$\cdots$N2.
Top row: model A.
Bottom row: model A without the acidic hydrogen atoms.
Left: section $t = 0.31$ corresponding to a maximum of the distance O1–H1o1 (*cf* Fig. 3 in the main text).
Right: section $t = 0.85$ corresponding to a minimum of the distance O1–H1o1.
Positive contours (solid lines), negative contours (dotted lines) and the zero contour (dashed lines) are drawn at intervals of 0.1 electrons/Å^3. Coloured circles are the projected positions of atoms that appear within 0.42 Å from the plane.

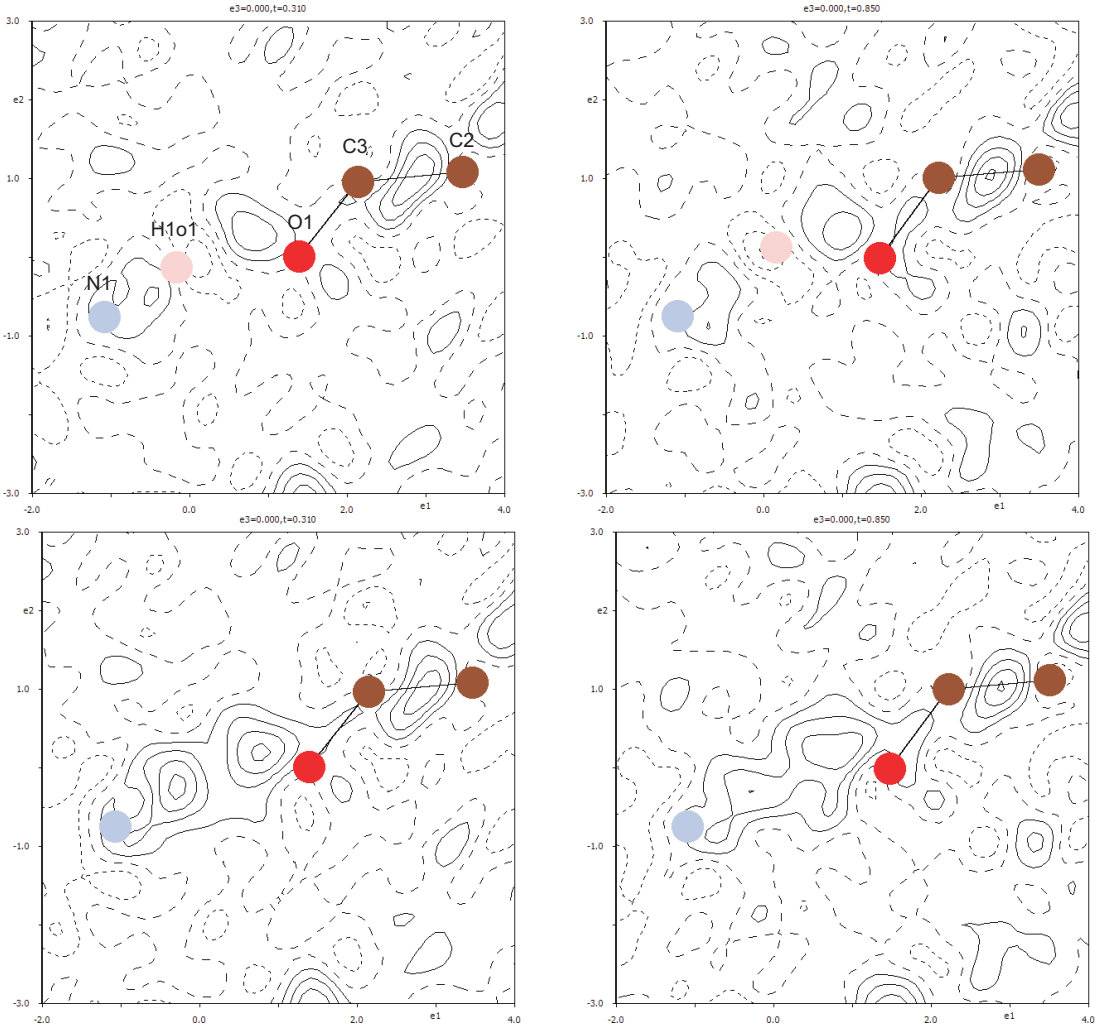

Figure A.3: Difference Fourier maps showing a section of 6×6 Å^2 in the plane through the hydrogen bond defined by the atoms O1—H1o1$\cdots$N1.
Top row: model A.
Bottom row: model A without the acidic hydrogen atoms.
Left: section $t = 0.31$ corresponding to a maximum of the distance O1–H1o1 (*cf* Fig. 3 in the main text).
Right: section $t = 0.85$ corresponding to a minimum of the distance O1–H1o1.
Positive contours (solid lines), negative contours (dotted lines) and the zero contour (dashed lines) are drawn at intervals of 0.1 electrons/Å^3. Coloured circles are the projected positions of atoms that appear within 0.42 Å from the plane.

Appendix B

Commensurate phenazine–chloranilic acid

B.1 Supplementary Material For Phenazine–Chloranilic Acid at 100 K

Figures 4.2 in the main text shows the supramolecular chain B is on top of the chain A and C is on top of the chain D which differentiate between each by 1/2 x fractional coordinate. A with B chain and C with D are stacked by π–π interactions along **b** with a typical π–π contacts of min. 3.368 Å, and max. 3.39 Å (Janiak, 2000). The bond distances of the asymmetric unit are comparable with the observed average values for similar organic compounds listed in the Cambridge Crystallographic Database (Macrae et al., 2008).

The structural changes can be explained based on the model in superspace. According the continuous modulation functions, H1o1 atom exhibit the largest modulation amplitude (Table B.2 and Fig. B.1), especially along **a** and they are responsible for modulation and ferroelectric transformation. This interpretation is supported by the variation in interatomic bonding distances due to the modulation wave, which is by far the largest variation for the H1O1 atoms. The modulation of C3, O1, and N1 follow of H1o1 Fig. B.1. Due to the formation of superstructure with a period twice as large as the main period, the freezing of displacement wave gives four valid points which can be explained in superspace model by t-plots at t equals to 0, 0.25, 0.5, and 0.75 or it can be explained as a two-fold superstructure by A, B, C, and D fragments, Table B.3 and Fig. 1.5- B.1.

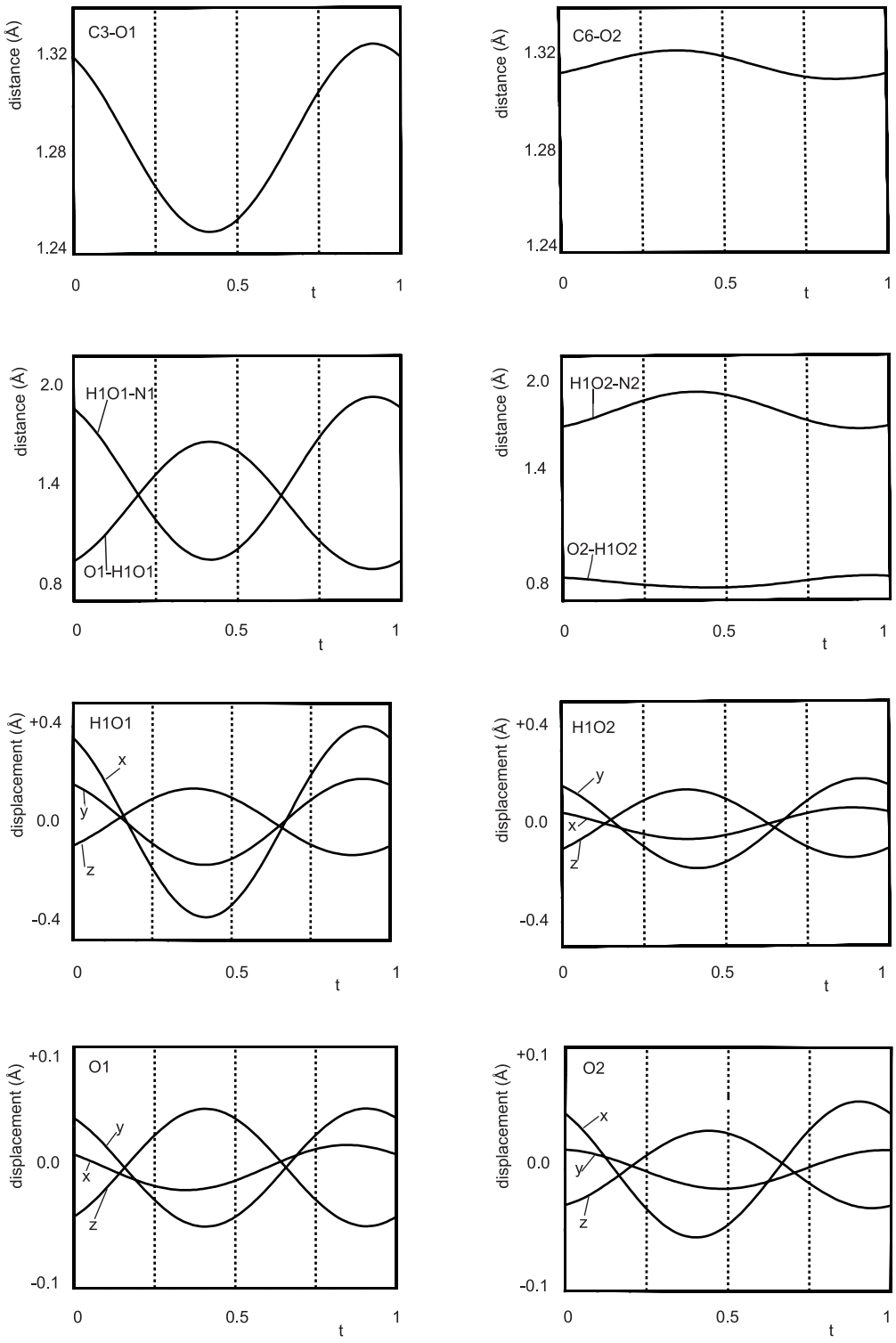

Figure B.1: Interatomic distances and displacement parameters as a function of phase t of modulation wave. Only the dashed lines in t-plots are giving a valid value due to the commensurate phase.

Table B.1: Intramolecular hydrogen bonds geometry (Å, deg) in refinement models, M_{free}

Hydrogen bond	d(O–H)	d(H–O)	d(O$\cdots$O)	angle
O1A–H1o1A$\cdots$O3A	0.943(15)	2.371(12)	2.7112(11)	100.9(9)
O1B$\cdots$H1o1B$\cdots$O3B	1.609(15)	2.725(12)	2.7024(11)	72.0(5)
O1C–H1o1C$\cdots$O3C	1.066(14)	2.457(11)	2.7075(12)	91.7(7)
O1D$\cdots$H1o1D$\cdots$O3D	1.467(14)	2.608(11)	2.7061(12)	77.7(5)
O2A–H1o2A$\cdots$O4A	0.863(15)	2.437(11)	2.7055(11)	98.7(8)
O2B–H1o2B$\cdots$O4B	0.796(15)	2.434(11)	2.6320(11)	95.4(9)
O2C–H1o2C$\cdots$O4C	0.840(14)	2.450(11)	2.6903(10)	97.4(8)
O2D–H1o2D$\cdots$O4D	0.815(14)	2.420(11)	2.6471(10)	97.1(8)

Table B.2: Fractional coordinates of the basic structure (basic) and modulation parameters (eqn (2) in the main text) for selected atoms

Atom	i	basic	A_i (Å)	B_i (Å)
O1	x	0.01723 (4)	0.0038 (5)	-0.0183 (5)
	y	1.02038 (17)	-0.0083 (8)	-0.0479 (6)
	z	0.2097 (3)	0.008 (8)	0.0479 (6)
O2	x	0.47886 (4)	-0.0456 (7)	0.0322 (7)
	y	1.11199 (17)	0.0204 (6)	-0.0240 (6)
	z	0.30161 (3)	-0.0060(6)	0.0144 (6)
H1O1	x	-0.0397 (6)	0.190 (10)	-0.347 (12)
	y	0.8104 (23)	0.089 (9)	0.157 (10)
	z	0.2310 (5)	-0.097 (10)	0.105 (11)
H1O2	x	0.51538 (7)	-0.046 (9)	0.041 (9)
	y	1.1773 (32)	-0.058 (8)	0.062 (9)
	z	0.2708 (5)	-0.0179 (9)	0.008 (10)

Table B.3: Selected bond distances and angles in A, B, C, and D supramolocular chains (Å, deg)

	A	*B*	*C*	*D*
C3–O1	1.3200(14)	1.2536(14)	1.3054(14)	1.2676(14)
C6–O2	1.3133(15)	1.3204(15)	1.3118(14)	1.3214(14)
C4–O3	1.2211(14)	1.2243(14)	1.2248(14)	1.2201(14)
C1–O4	1.2183(14)	1.2385(14)	1.2210(14)	1.2355(14)
N1–C12	1.3451(11)	1.3465(11)	1.3443(14)	1.3468(12)
N1–C17	1.3490(14)	1.3505(14)	1.3464(14)	1.3526(14)
C3–O1–H1o1	115.4(7)	134.4(4)	122.2(6)	130.7(4)
C6–O2–H1o2	123.1(7)	126.9(8)	125.0(7)	125.2(7)

Appendix C

Morpholinium tetrafluoroborate

C.1 Structural parameters in the incommensurate phase

Table C.1: Displacement modulation functions for two crystallographically independent of $[BF_4]^-$ as defined in the pseudo-rigid-body approach. Molecular translations and their harmonic modulations amplitudes A_t and B_t are given as relative coordinates.

Molecule		x_{trans}	y_{trans}	z_{trans}
Ma		0.1764(10)	0.1458(7)	0.2620(5)
	A_t	0.0004(8)	0.0009(7)	0.0086(6)
	B_t	-0.0052(9)	-0.0025(8)	0.0009(6)
Mb		0.1542(4)	0.1251(3)	0.2632(4)
	A_t	-0.0016(4)	-0.0001(3)	0.0015(2)
	B_t	-0.0025(4)	0.0007(3)	-0.0029(3)

Table C.2: Angles for rotations of the pseudo-rigid bodies Ma and Mb towards their final orientations, together with their harmonic modulation amplitudes A_r and B_r.

Molecule		ϕ	χ	ψ
Ma		0	0	0
	A_r	0.0056(8)	-0.0024(7)	0.0074(8)
	B_r	-0.0035(9)	0.0013(8)	0.0018(8)
Mb		-66.8(15)	72.3(4)	17.0(14)
	A_r	0.0032(4)	-0.0048(5)	0.0014(3)
	B_r	0.0031(4)	0.0124(5)	-0.0011(3)

Table C.3: Fractional atomic coordinates for $[BF_4]^-$ model molecule at T = 130 K in pseudo rigid body approach. Standard uncertainties are given in parentheses.

Atom	x	y	z
B1	0.0	0.0	0.0
F1	0.05610(10)	0.11165(67)	0.08092(77)
F2	0.12854(71)	-0.08766 (77)	-0.03676(72)
F3	-0.11639 (93)	-0.07496 (81)	0.07523(98)
F4	-0.0753(11)	0.05334(99)	-0.11803(45)

Table C.4: Anisotropic atomic displacement parameters (anisotropic ADPs) U_{ij} (Å^2) for atoms of the morpholinium cation. Standard uncertainties are given in parentheses.

Atom	U_{11}	U_{22}	U_{33}	U_{12}	U_{13}	U_{23}
O1	0.0268(4)	0.0225(3)	0.0408(4)	0.0068(2)	0	0
N1	0.0226(4)	0.0140(3)	0.0348(4)	0.0002(2)	0	0
C1	0.0319(4)	0.0254(3)	0.0355(4)	0.0038(2)	-0.0016(3)	-0.0080(3)
C2	0.0317(4)	0.0245(3)	0.0258(3)	0.0000(2)	-0.0024(3)	-0.0002(2)

Table C.5: Fractional atomic coordinates (x, y, z) and amplitudes of displacement modulation functions (in Å). The coordinates and amplitudes of atomic displacive modulation function for individual atoms involved in model molecule, BF_4 (i.e. rigid body), obtained after transformation of molecular model to the atomic model, two molecular positions are labeled as a and b in atomic model. Standard uncertainties are given in parentheses.

Atom	x	y	z	$A_x \times a$	$A_y \times b$	$A_z \times c$	$B_x \times a$	$B_y \times b$	$B_z \times c$
O1	0.03325(8)	0.76042(7)	0.25	0	0	0.18697(86)	0	0	-0.13398(86)
N1	0.26967(10)	0.53852(7)	0.25	0	0	0.14133(76)	0	0	-0.12223(76)
C1	0.12677(9)	0.72991(7)	0.37325(7)	-0.0590(7)	-0.0519(7)	0.1573(8)	-0.0614(7)	0.0740(7)	-0.1091(8)
C2	0.17305(9)	0.57457(7)	0.37788(7)	-0.0722(7)	-0.0487(7)	0.1181(7)	-0.0616(6)	0.0834(7)	-0.0243(7)
H1c	0.2937	0.4431	0.25	0	0	0.1366	0	0	0.0516
H2b	0.2391	0.5566	0.4593	-0.1271	-0.0499	0.1413	-0.0793	0.1364	-0.0134
H2a	0.0747	0.5179	0.3809	-0.0567	-0.0687	0.0563	-0.0818	0.0725	-0.0134
H1d	0.3671	0.5886	0.25	0	0	0.1900	0	0	-0.0745
H1b	0.0626	0.7533	0.4544	-0.0696	-0.1016	0.1681	-0.1206	0.1016	-0.1251
H1a	0.2251	0.7867	0.374	-0.0712	-0.0339	0.1824	-0.0429	0.0828	-0.1537
B1a	0.1764(10)	0.1458(8)	0.262(5)	-0.003(7)	0.009(7)	0.082(6)	-0.042(7)	-0.024(8)	0.009(6)
F1a	0.2325(14)	0.2575(10)	0.3429(9)	-0.096 (11)	0.007(9)	0.136(9)	-0.037(012)	0.006(10)	-0.047(11)
F2a	0.3049(12)	0.0581(11)	0.2253(9)	0.055(9)	0.0875(10)	0.071(10)	-0.053(10)	-0.047(11)	-0.005(12)
F3a	0.06(13)	0.0708(11)	0.3373(11)	0.041(10)	-0.081(10)	0.015(10)	-0.009(11)	-0.046(11)	0.047(11)
F4a	0.1011(14)	0.1991(12)	0.144(7)	-0.007(11)	-0.030(10)	0.089(8)	-0.065(11)	-0.061(12)	0.020(8)
B1b	0.1542(4)	0.1251(3)	0.2632(4)	-0.001(3)	-0.009(3)	0.016(3)	0.001(3)	0.033(3)	0.012(4)
F1b	0.298(4)	0.047(4)	0.2512(13)	0.012(4)	0.023(5)	0.024(6)	-0.019(4)	0.020(5)	-0.112(6)
F2b	0.065(2)	0.119(3)	0.1410(10)	0.017(4)	-0.122(6)	0.007(5)	-0.016(5)	0.157(7)	0.019(5)
F3b	0.062(3)	0.071(3)	0.3725(12)	-0.002(4)	0.039(6)	0.040(5)	0.011(5)	-0.070(6)	-0.026(6)
F4b	0.194(5)	0.264(2)	0.2939(13)	-0.033(5)	0.011(5)	-0.025(7)	-0.032(5)	-0.009(5)	0.162(7)

Table C.6: Parameters for the harmonic occupational modulations for individual atoms, as obtained by transformation of the pseudo-rigid-body model. Average occupancy ($P^0(\mu)$) and the amplitudes of the harmonic modulation function $P^s(\mu)$ and $P^c(\mu)$.

Atom	$P^0(\mu)$	$P^s(\mu)$	$P^c(\mu)$
B1a	0.184953	-0.120295	0.150007
F1a	0.184953	-0.096757	0.166166
F2a	0.184953	-0.063294	0.181568
F3a	0.184953	-0.160144	0.106428
F4a	0.184953	-0.1431	0.1183
B1b	0.315047	-0.139946	0.139398
F1b	0.315047	-0.07811	0.181426
F2b	0.315047	-0.168714	0.1027724
F3b	0.315047	-0.169437	0.101526
F4b	0.315047	-0.12416	0.153257

C.2 Rigid body refinement for the crystal structure at 160 K

X-ray diffraction is employed for the same crystal that is used in incommensurate phase. Data were collected on a 2-circle diffractometer equipped with image plate MAR345 detector. The crystal was cooled down to T=160 K employing an open flow nitrogen cryostat by Oxford Cryosystems. The software Eval15 (Schreurs et al., 2010) was used for data processing of the measured diffraction images. All Bragg reflections that indexed by software Eval15 resulted in a primitive orthorhombic cell, [see Fig.5.1.a]. The integrated intensities (integration by Eval15) were scaled and absorption correction was applied by the software Sadabs (Sheldrick, 2008) and averaged in point group mmm. Initial values for the parameters of the structure have been taken from the basic structure at 130 K (Section 5.2.2). Space group *Pnam* has been selected. The same as the model of Szklarz et al. (2009) and model at incommensurate phase (Section 5.2.2), the atoms O1, N1, H1c and H1d and the $[BF_4]^-$ molecule occupy special position on the mirror symmetry plan. Therefore, two orientations, Ma and Mb, for the molecular part have been used and the sum of occupancies of two positions was restricted to 0.5. Two other symmetry related orientations were generated by mirror operator, Table C.12. Anisotropic atomic displacement parameters (ADPs) have been used for all non-H atoms excluding atoms involved in the molecular part. Instead, TLS parameters for two orientations of the $[BF_4]^-$ molecule have been refined. Employing JANA2006 (Petricek et al., 2014), the positions of all atoms of morpholinium molecule and two orientations of $[BF_4]^-$ molecule were refined. Refining the occupancies of two molecular orientations which are located on m symmetry plane resulted in 19% (Ma) and 31% (Mb). The refinement of structure by application of rigid body approach results in a good fit to data with $R_F^{obs} = 5.06\%$, and $R_F^{all} = 10.3\%$. More details about crystal structure data and refinement parameters are given in Table C.7.

For comparison of the molecular model with the independent atomic model which is reported by Szklarz et al. (2009), the data were refined against the model of Szklarz et al. (2009). Refinement parameters and geometrical parameters for the molecular model improve in the model that the four orientation of the anion are defined by the rigid-body approach (Tables C.7, C.8, C.9 and C.10).

Table C.7: Crystal data and refinement details

	Rigid body model	Atomic model[a]
Temperature (K)	160	
Chemical formula	C_4NOH_{10} BF_4	
Formula weight	174.93	
Space group	$Pnam$	
a (Å)	8.142(1)	
b (Å)	9.419(2)	
c (Å)	9.597(2)	
V (Å^3)	736.0(2)	
Z	4	
D_{calc} ($g\,cm^{-3}$)	1.5787	
Crystal color	Colorless	
Radiation type	Mo-Kα	
Wavelength (Å)	0.7107	
Scan mode	ϕ	
Theta range (deg)	3.03 to 39.03	
Range of h	-10 to 10	
Range of k	-13 to 16	
Range of l	-17 to 16	
μ (mm^{-1})	0.172	
Absorption corr.	SADABS	
No. of reflections		
Measured	14079	
Independent	1797	
Observed	997	
$R_{int}(obs, all)$ averaged in mmm	4.41, 5.31	
Criterion for observed reflections	$I > 3\sigma(I)$	
Refinement, Software	on F, JANA2006	
GOF^{obs},GOF^{all}	3.31,2.47	3.16, 2.43
R_F^{obs}, wR_F^{obs}	0.0506, 0.0664	0.0542, 0.0724
No. of parameters	93	111
$\Delta\rho_{max}$, $\Delta\rho_{min}$(e Å^{-3})	0.26, -0.22	0.3, -0.33

[a] *Refinement of the model of Szklarzet al.* (2009) *against the measured data in Bayreuth.*

Table C.8: Bond lengths (Å) for two structural models at T = 160 K. Standard uncertainties are given in parentheses.

Bond	Rigid Body Model	Atomic Model[a]
O1-C1	1.430(2)	1.4280(17)
C1-C2	1.5084(16)	1.5093(18)
C1-H1a	0.96	0.96
C1-H1b	0.96	0.96
C2-H2a	0.96	0.96
C2-H2b	0.96	0.96
N1-C2	1.4952(14)	1.4936(15)
N1-H1d	0.92	0.92
N1-H1c	0.92	0.92
B1a-F1a	1.37(2)	1.40(3)
B1a-F2a	1.38(2)	1.31(3)
B1a-F3a	1.37(2)	1.40(4)
B1a-F4a	1.38(3)	1.20(3)
B1b-F1b	1.37(3)	1.387(13)
B1b-F2b	1.38(2)	1.36(3)
B1b-F3b	1.37(2)	1.12(3)
B1b-F4b	1.38(2)	1.317(15)

[a] *Refinement of the model of Szklarzet al.* (2009) *against the measured data in Bayreuth.*

Table C.9: Bond angles (deg) for two structural models at T = 160 K. Standard uncertainties are given in parentheses.

Angle	Rigid Body Model	Atomic Model[a]
C1-O1-C1^{i}	110.94(11)	110.97(10)
C1-C2-H2b	109.47	109.47
C2-N1-C2^{i}	110.33(10)	110.29(10)
C1-C2-H2a	109.47	109.47
C2-N1-H1d	109.47	109.47
H2b-C2-H2a	109.82	109.82
C2-N1-H1c	109.47	109.47
C2^{i}-N1-H1d	109.47	109.47
C2^{i}-N1-H1c	109.47	109.47
H1d-N1-H1c	108.64	108.64
O1-C1-C2	110.61(11)	110.58(10)
O1-C1-H1b	109.47	109.47
O1-C1-H1a	109.47	109.47
C2-C1-H1b	109.47	109.47
C2-C1-H1a	109.47	109.47
H1b-C1-H1a	109.47	108.34
N1-C2-C1	109.12(10)	109.12(9)
N1-C2-H2b	109.47	109.47
N1-C2-H2a	109.47	109.47
F1a-B1a-F2a	111.1(13)	110(2)
F1a-B1a-F3a	109.1(14)	105(3)
F1a-B1a-F4a	108.9(14)	109.2(19)
F2a-B1a-F3a	109.8(14)	103(2)
F2a-B1a-F4a	107.4(13)	118(3)
F3a-B1a-F4a	110.1(15)	111(2)
F1b-B1b-F2b	111.4(15)	113.0(10)
F1b-B1b-F3b	109.1(14)	107.5(14)
F1b-B1b-F4b	107.4(15)	107.2(8)
F2b-B1b-F3b	109.8(14)	108.0(9)
F2b-B1b-F4b	107.4(15)	112.7(15)
F3b-B1b-F4b	110.1(15)	108.2(4)

[i] $x, y, -z + 1/2$.

[a] *Refinement of the model of Szklarzet al.* (2009) *against the measured data in Bayreuth.*

Table C.10: Fractional atomic coordinates and isotropic displacement parameters (Å^2) for two structural models at T = 160 K. Standard uncertainties are given in parentheses.

Atom	x	y	z	U_{iso}
O1	0.02973(14)	0.76008(11)	0.25	0.0361(4)
O1^a	0.02973(16)	0.76000(13)	0.25	0.0369(4)
N1	0.26672(15)	0.53943(11)	0.25	0.0274(4)
N1^a	0.26672(17)	0.53936(13)	0.25	0.0282(4)
C1	0.12310(16)	0.73028(13)	0.37273(14)	0.0370(4)
C1^a	0.12299(18)	0.73033(14)	0.37261(16)	0.0378(4)
C2	0.17055(15)	0.57557(11)	0.37783(12)	0.0321(3)
C2^a	0.17055(17)	0.57554(13)	0.37769(14)	0.0331(4)
H1c	0.2906	0.444	0.25	0.041095
H1c^a	0.2905	0.4439	0.25	0.033822
H2b	0.2366	0.5583	0.4589	0.038547
H2b^a	0.2366	0.5583	0.4588	0.039688
H2a	0.0732	0.5182	0.3814	0.038547
H2a^a	0.0732	0.5181	0.3812	0.039688
H1d	0.3638	0.5894	0.25	0.041095
H1d^a	0.3638	0.5894	0.25	0.033822
H1b	0.0592	0.7536	0.4536	0.044439
H1b^a	0.0591	0.7536	0.4535	0.045368
H1a	0.2205	0.7878	0.3733	0.044439
H1a^a	0.2203	0.7879	0.3732	0.045368
B1a	0.1761	0.1497	0.262	0.026532
B1a^a	0.174(3)	0.137(2)	0.2684(5)	0.019(5)
F1a	0.2317	0.2605	0.3416	0.052829
F1a^a	0.233(3)	0.2557(18)	0.342(2)	0.049(4)
F2a	0.3006	0.0566	0.2302	0.047879
F2a^a	0.29684(15)	0.04914(12)	0.25	0.0520(5)
F3a	0.0539	0.0799	0.3329	0.059682
F3a^a	0.066(3)	0.085(4)	0.332(3)	0.081(6)
F4a	0.1163	0.2022	0.1382	0.078348
F4a^a	0.121(3)	0.208(3)	0.1381(11)	0.072(6)
B1b	0.1536	0.1228	0.2355	0.023328
B1b^a	0.1568(16)	0.1300(9)	0.228(4)	0.028(5)
F1b	0.2947	0.0456	0.2538	0.04441
F1b^a	0.29684(15)	0.04914(12)	0.25	0.0520(5)
F2b	0.0597	0.0688	0.1288	0.031546
F2b^a	0.0575(11)	0.0678(8)	0.1320(8)	0.0287(13)
F3b	0.065	0.1218	0.3572	0.056123
F3b^a	0.0638(14)	0.125(2)	0.3569(11)	0.061(4)
F4b	0.1948	0.2598	0.2003	0.062633
F4b^a	0.1957(16)	0.2624(10)	0.1991(19)	0.066(5)

^{a}*Refinement of the model of Szklarzet al.* (2009) *against the measured data in Bayreuth.*

Table C.11: Fractional atomic coordinates for the $[BF_4]^-$ model molecule at T = 160 K in pseudo rigid body approach. Standard uncertainties are given in parentheses.

Atom	x	y	z
B1	0.0	0.0	0.0
F1	0.0556(18)	0.1108(13)	0.0797(18)
F2	0.1246(14)	-0.0931 (14)	-0.0318 (12)
F3	-0.1222 (18)	-0.0698 (15)	0.0709(19)
F4	-0.0598 (24)	0.0525 (18)	-0.1237(8)

Table C.12: Rotational and translational parameters for two defined molecular positions of $[BF_4]^-$ anion, Ma and Mb, in rigid body approach for the structure at T=160 K.

Molecule	ϕ	χ	ψ	x_{trans}	y_{trans}	z_{trans}
Ma	0	0	0	0.1761(13)	0.1497(13)	0.2620(11)
Mb	-78.49	51.22	4.492	0.1536(8)	0.1228(6)	0.2353(9)

Bibliography

Albert, A. and Phillips, J. N. (1956). Ionization constants of heterocyclic substances. part ii. hydroxy-derivatives of nitrogenous six-membered ring-compounds, *J. Chem. Soc.* pp. 1294–1304.

Allen, F. H., Kennard, O., Watson, D. G., Brammer, L., Orpen, A. G. and Taylor, R. (1987). Tables of bond lengths determined by x-ray and neutron diffraction. part 1. bond lengths in organic compounds, *J. Chem. Soc. Perkin Trans. 2* (12): S1–S19.

Amano, M., Yamamura, Y., Sumita, M., Yasuzuka, S., Kawaji, H., Atake, T. and Saito, K. (2009). Calorimetric and dielectric study of organic ferroelectrics, phenazine-chloranilic acid, and its bromo analog, *J. Chem. Phys.* **130**(3): 034503,1–7.

Atake, T. and Chihara, H. (1980). Heat capacity anomalies due to successive phase transitions in 1,1'–biphenyl, *Solid State Commun* **35**: 131–135.

Bastiansen, O. and Samdal, S. (1985). Structure and barrier of internal rotation of biphenyl derivatives in the gaseous state: Part 4. barrier of internal rotation in biphenyl, perdeuterated biphenyl and seven non-ortho-substituted halogen derivatives, *J. Mol. Struct* **128**: 115–125.

Baudour, J. L. and Sanquer, M. (1983). Structural phase transition in polyphenyls. VIII. The modulated structure of phase III of biphenyl (T= 20 K) from neutron diffraction data, *Acta Crystallogr. B* **39**: 75–84.

Biedermann, F. and Schneider, H.-J. (2016). Experimental binding energies in supramolecular complexes, *Chem. Rev.* **116**: 5216–5300.

Bonnell, D. A. (2013). Ferroelectric Organic Materials Catch Up with Oxides, *Science* **339**: 401–403.

Buist, A. R., Kennedy, A. R. and Manzie, C. (2014). Four salt phases of theophylline, *Acta Crystallogr. C* **70**: 220–224.

Charbonneau, G. and Delugeard, Y. (1976). Structural transition in polyphenyls.iii. crystal structure of biphenyl at 110 k, *Acta Crystallogr. B* **32**: 1420–1423.

Charbonneau, G. and Delugeard, Y. (1977). Biphenyl: Three-dimensional data and new refinement at 293K, *Acta. Crystalloger. B* **33**: 1586–1588.

Czapla, Z., Dacko, S., Kosturek, B. and Waskowska, a. (2005). Dielectric and optical properties related to phase transitions in an imidazolium perchlorate $[C_3N_2H_5ClO_4]$ crystal, *Phys. Status Solidi B* **242**(14): R122–R124.

Czarenki, P., Nawrocik, W., Pajak, Z. and Wasicki, J. (1994a). Ferroelectric properties of pyridinium perchlorate, *J.Phys.: Condens. Matter.* **6**: 4955–4960.

Czarenki, P., Nawrocik, W., Pajak, Z. and Wasicki, J. (1994b). Ferroelectric properties of pyridinium tetrafluoroborate, *Phys. Rev. B* **49**: 1511–1512.

de Wolff, P. M. (1974). The pseudo-symmetry of modulated crystal structures, *Acta Crystallogr. A* **82**(30): 777–785.

de Wolff, P. M., Janssen, T. and Janner, A. (1981). The superspace groups for incommensurate crystal structures with a one-dimensional modulation, *Acta Crystallogr. A* **37**: 625–636.

Dzyabchenko, A. and Scheraga, H. A. (2004). Model for the crystal packing and conformational changes of biphenyl in incommensurate phase transitions, *Acta Crystallogr. B* **60**: 228–237.

Eaton, V. J. and Steele, D. (1973). Dihedral angle of biphenyl in solution and the molecular force field, *J. Chem. Soc., Faraday Trans. 2* **69**: 1601–1608.

Engh, R. A. and Huber, R. (1991). Accurate bond and angle parameters for x-ray protein structure refinement, *Acta Crystallogr. A* **47**(4): 392–400.

Fu, D. W., Cai, H. L., Liu, Y., Ye, Q., Zhang, W., Zhang, Y., Xue Yuan, C., Gianluca, G., Capone, M., Li, J. and Xiong, R. G. (2013). Diisopropylammonium bromide is a high-temperature molecular, *Science* **339**(2009): 425–428.

Furukawa, T. (1989). Ferroelectric properties of vinylidene fluoride copolymers, *Phase Trans.* **107**: 143–211.

Gilli, G. and Gilli, P. (2009). *The Nature of the Hydrogen Bond: Outline of a Comprehensive Hydrogen Bond Theory*, Oxford University Press.

Goldsmith, G. J. and White, J. G. (1959). Ferroelectric behavior of thiourea, *J.Chem.Phys.* **31**: 1175–1187.

Gonzalo, J. A. (1990). *Effective Field Approach to Phase Transitions and Some Applications to Ferroelectrics*, Vol. 76, 2nd edn, World Scientific.

Gotoh, K., Asaji, T. and Ishida, H. (2007). Hydrogen bonding in two solid phases of phenazine-chloranilic acid (1/1) determined at 170 and 93 K, *Acta Crystallogr. C* **63**(1): o17–o20.

Grigoriev, M. S., German, K. E. and Maruk, Y. (2007). Morpholinium tetraoxidorhenate (VII), *Acta Crystallogr. E* **63**: m2355.

Grigoriev, M. S., German, K. E. and Maruk, Y. (2008). Morpholinium perchlorate, *Acta Crystallogr. E* **64**: 390.

Haertling, G. H. (1999). Ferroelectric ceramics: History and technology, *J. Am. Ceram. Soc.* **82**: 797–818.

Hashino, S., Mitsuui, T. and Pepinsky, R. (1959). Dielectric and thermal study of tri-glycine sulfate and tri-glycine fluoberyllate, *Phys. Rev.* **107**: 1255–1258.

Horiuchi, S., Ishii, F., Kumai, R., Okimoto, Y., Tachibana, H., Nagaosa, N. and Tokura, Y. (2005). Ferroelectricity near room temperature in co-crystals of nonpolar organic molecules, *Nature Mater.* **4**(2): 163–166.

Horiuchi, S., Kumai, R. and Tokura, Y. (2005). Room-temperature ferroelectricity and gigantic dielectric susceptibility on a supramolecular architecture of phenazine and deuterated chloranilic acid, *J. Amer. Chem. Soc.* **127**(14): 5010–5011.

Horiuchi, S., Kumai, R. and Tokura, Y. (2009). Proton-displacive ferroelectricity in neutral cocrystals of anilic acids with phenazine, *J. Mater. Chem.* **19**(25): 4421–4434.

Horiuchi, S., Tokunaga, Y., Giovannetti, G., Picozzi, S., Itoh, H., Shimano, R., Kumai, R. and Tokura, Y. (2010). Above-room-temperature ferroelectricity in a single-component molecular crystal, *Nature* **463**(7282): 789–792.

Horiuchi, S. and Tokura, Y. (2008). Organic ferroelectrics, *Nature Mater.* **7**(5): 357–366.

Janiak, C. (2000). A critical account on π-π stacking in metal complexes with aromatic nitrogen-containing ligands, *J. Chem. Soc. Dalton Trans.* **21**: 3885–3896.

Janssen, T., Janner, A., Looijenga-Vos, A. and de Wolff, P. M. (2006). Incommensurate and commensurate modulated structures, *in* E. Prince (ed.), *Int. Tables for Crystallogr. Vol. C*, Kluwer Academic Publishers, Dordrecht, pp. 907–955.

Jeffrey, G. A. (1997). *An Introduction to Hydrogen Bonding*, Oxford University Press.

Katrusiak, A. and Szafranski, M. (1999). Ferroelectricity in NH...N Hydrogen Bonded Crystals, *Phys. Rev. lett.* **82**(3): 576–579.

Kittle, C. (2005). *Introduction to solid state physics*, 8th edn, John Wiley and Sons.

Kumai, R., Horiuchi, S., Fujioka, J. and Tokura, Y. (2012). Ferroelectricity and pressure-induced phenomena driven by neutral ionic valence instability of acid-base supramolecules, *J. Amer. Chem. Soc.* **134**(2): 1036–1046.

Kumai, R., Horiuchi, S., Okimoto, Y. and Tokura, Y. (2006). Large dielectric susceptibility associated with proton transfer in a supramolecular structure of chloranilic acid and 5,5'-dimethyl-2,2'-bipyridine, *J. Chem. Phys.* **125**(8): 084715.

Kumai, R., Horiuchi, S., Sagayama, H., Arima, T. H., Watanabe, M., Noda, Y. and Tokura, Y. (2007). Structural assignment of polarization in hydrogen-bonded supramolecular ferroelectrics., *J. Amer. Chem. Soc.* **129**(43): 12920–12921.

Lee, K., Kolb, B., Thonhauser, T., Vanderbilt, D. and Langreth, D. (2012). Structure and energetics of a ferroelectric organic crystal of phenazine and chloranilic acid, *Phys. Rev. B* **86**(10): 102–104.

Lines, M. and Glass, A. M. (2001). *Principles and Applications of Ferroelectrics and Related Materials*, Oxford University Press.

Macrae, C. F., Bruno, I. J., Chisholm, J. A., Edgington, P. R., McCabe, P., Pidcock, E., Rodriguez-Monge, L., Taylor, R., van de Streek, J. and Wood, P. A. (2008). Mercury CSD 2.0 new features for the visualization and investigation of crystal structures, *J. Appl. Crystallogr.* **41**(2): 466–470.

Mercadal, N., Day, S. P., Jarmyn, A., Pitak, M. B., Coles, S. J., Wilson, C., Rees, G. J., Hanna, J. V. and Wallis, J. D. (2014). O- vs. n-protonation of 1-dimethylaminonaphthalene-8-ketones: formation of a peri n-c bond or a hydrogen bond to the pi-electron density of a carbonyl group, *CrystEngComm* **16**(36): 8363–8374.

Molcanov, K. and Kojic-Prodic, B. (2010). Salts and co-crystals of chloranilic acid with organic bases: is it possible to predict a salt formation?, *CrystEngComm* **12**: 925–939.

Müller, P., Herbst-Irmer, R., Spek, A. L., Schneider, T. R. and Sawaya, M. R. (2005). *Crystal Structure Refinement. A Crystallographers Guide to SHELXL*, Oxford University Press.

Noohinejad, L., Mondal, S., Wölfel, A., Ali, S. I., Schönleber, A. and van Smaalen, S. (2014). Ferroelectricity of phenazine–chloranilic acid at T= 100 K, *J. Chem. Crystallogr.* **44**(8): 387–393.

Owczarek, M., Jakubas, R., Bator, G., Pawlukojć, a., Baran, J., Przesawski, J. and Medycki, W. (2011). Vibrational and thermodynamic properties and molecular motions in the incommensurate crystal of morpholinium tetrafluoroborate studied by ^{1}H NMR, *Chem. Phys.* **381**: 11–20.

Owczarek, M., Jakubas, R., Pietraszko, A., W., M. and Baranc, J. (2013). Investigation of structure properties relationship in a novel family of halogenoantimonates (III) and halogenobismuthates (III) with morpholinium cation: $[NH_2(C_2H_4)_2O]MX_4$. Crystal structure, phase transitions and dynamics of molecules, *Dalton Trans.* **42**: 15069–15079.

Owczarek, M., Szklarz, P., Jakubas, R. and Lis, T. (2008). The low temperature phase of morpholinium tetrafluoroborate, *Acta Crystallogr. E* **64**: 112–122.

Owczarek, M., Szklarz, P., Jakubas, R. and Miniewiczb, A. (2012). $[NH_2(C_2H_4)_2O]MX_5$: a new family of morpholinium nonlinear optical materials among halogenoantimonate(III) and halogenobismuthate(III) compounds.

Structural characterization, dielectric and piezoelectric properties, *Dalton Trans.* **41**: 7285–7294.

Pajak, Z., Czarnecki, P., Szafra, B., Mauzyska, H. and Fojud, Z. (2004). Ferroelectric order in highly disordered molecular-ionic crystals, *Phys. Rev. B: Condens. Matter* **69**: 2–4.

Palatinus, L. (2004). Ab initio determination of incommensurately modulated structures by charge flipping in superspace, *Acta Crystallogr. A* **60**(6): 604–610.

Palatinus, L. (2013). The charge-flipping algorithm in crystallography, *Acta Crystallogr. B* **69**: 1–16.

Palatinus, L. and Chapuis, G. (2007). SUPERFLIP a computer program for the solution of crystal structures by charge flipping in arbitrary dimensions, *J. Appl. Crystallogr.* **40**: 786–790.

Perez-Mato, J. M., Orobengoa, D. and Aroyo, M. I. (2010). Mode crystallography of distorted structures, *Acta Crystallogr. A* **66**: 558–590.

Petricek, V., Coppens, P. and Becker, P. (1985). Structure analysis of displacively modulated molecular crystals, *Acta Crystalloger. A* **41**: 478–483.

Petricek, V., Dusek, M. and Palatinus, L. (2014). Crystallographic computing system JANA2006: General features, *Z. Kristallogr* **229**(5): 345–352.

Price, J. T., Paquette, J. a., Harrison, C. S., Bauld, R., Fanchini, G. and Gilroy, J. B. (2014). 6-Oxoverdazyl radical polymers with tunable electrochemical properties, *Polym. Chem.* **5**: 5223–5226.

Saito, K., Amano, M., Yamamura, Y., Tojo, T. and Atake, T. (2006). Low-temperature phase transitions of an organic ferroelectrics, phenazine-chloranilic acid, *J. Phys. Soc. Jpn* **75**(3): 033601.

Schick, S., Pape, T. and Hahn, F. E. (2014). Coordination Chemistry of Bidentate Bis(NHC)Ligands with Two Different NHC Donors, *Organometalics* **33**: 4035–4041.

Schomaker, V. and Trueblood, K. N. (1968). On the rigid-body motion of molecules in crystals, *Acta Crystallogr. B* **24**: 63–76.

Schönleber, A. (2011). Organic molecular compounds with modulated crystal structures, *Z. Kristallogr.* **226**(6): 499–517.

Schönleber, A., van Smaalen, S. and Larsen, K. (2010). Orientational disorder in Λ-cobalt(III) sepulchrate trinitrate, *Acta Crystallogr. C* **66**: 107–109.

Schönleber, A., van Smaalen, S., Weiss, H.-C. and Kesel, A. J. (2014). N–H...O and C–H...F hydrogen bonds in the incommensurately modulated crystal structure of adamantan-1-ammonium 4-fluorobenzoate, *Acta Crystallogr. B* **70**: 652–659.

Schreurs, A. M. M., Xian, X. and Kroon-Batenburg, L. M. J. (2010). EVAL15: a diffraction data integration method based on ab initio predicted profiles, *J. Appl. Crystallogr.* **43**(1): 70–82.

Sheldrick, G. M. (2008). *SADABS, Version 2008/1*, Göttingen: University of Göttingen.

Stokes, H. T., Campbell, B. J. and van Smaalen, S. (2011). Generation of (3 + d)-dimensional superspace groups for describing the symmetry of modulated crystalline structures., *Acta Crystallogr. A* **67**: 45–55.

Stout, G. and Jensen, L. (1989). *X-Ray Structure Determination*, Wiley-Interscience.

Sun, Z., Li, S., Zhang, S., Deng, F., Hong, M. and Luo, J. (2014). Second-Order Nonlinear Optical Switch of a New Hydrogen-Bonded Supramolecular Crystal with a High Laser-Induced Damage Threshold, *Adv. Optic. Mater.* **2**: 1199–1205.

Szklarz, P., Owczarek, M., Bator, G., Lis, T., Gatner, K. and Jakubas, R. (2009). Crystal structure, properties and phase transitions of morpholinium tetrafluoroborate $[C_4H_{10}NO][BF_4]$, *J. Mol. Struct.* **929**(1-3): 48–57.

Valasek, J. (1920). Piezoelectric and allied phenomena in Rochelle salt, *Physical Review* **15**: 537.

van Smaalen, S. (2004). An elementary introduction to superspace crystallography, *Z. Kristallogr.* **219**: 681–691.

van Smaalen, S. (2012). *Incommensurate Crystallography*, Oxford University Press.

van Smaalen, S., Campbell, B. J. and Stokes, H. T. (2013). Equivalence of superspace groups, *Acta Crystallogr. A* **69**: 75–90.

Wagner, T. and Schönleber, A. (2009). A non-mathematical introduction to the superspace description of modulated structures, *Acta Crystallogr. B* **65**(3): 249–268.

Wang, Z.-M. and Gao, S. (2013). Can molecular ferroelectrics challenge pure inorganic ones?, *National Science Rev.* **1**: 25–26.

Publications

Parts of this thesis have been published in or will be submitted to scientific journals:

Chapter 3
L. Noohinejad, S. Mondal, S. I. Ali, S. Dey, S. van Smaalen and A. Schönleber:
Resonance-stabilized partial proton transfer in hydrogen bonds of incommensurate Phenazine–chloroanilic acid,
Acta Cryst. B, **71**: 228- 234 (2015)

Chapter 4
L. Noohinejad, S. Mondal, A. Wölfel, S. I. Ali, A. Schönleber, and S. van Smaalen:
Ferroelectricity of phenazine–chloranilic acid at $T = 100$ K,
J. Chem. Crystallogr, **44**: 387- 393 (2014)

Chapter 5
L. Noohinejad, V. Petricek, A. Schönleber, and S. van Smaalen:
Disordered $[BF_4]^-$ Anions in the Incommensurate Crystal of Morpholinium Tetrafluoroborate

During my doctoral studies I contributed to research projects which are not part of my PhD thesis. The following publication resulted from this work:
S. Mondal, S. van Smaalen, G. Parakhonskiy, P. S. Jagannatha, L. Noohinejad, E. Bykova, and N. Dubrovinskaia:
Experimental evidence of orbital order in α-B12 and γ-B28 polymorphs of elemental boron, *Phys. Rev. B*, **88**: 024118 (2013)

List of Figures

List of Tables

Declaration

Ich versichere hiermit eidesstattlich, dass ich diese Dissertation selbstständig und nur unter Verwendung angebener Quellen und zulässiger Hilfsmittel erstellt habe. Ich habe bisher keine Promotionsversuche unternommen. Ich habe bisher weder die Hilfe von gewerblichen Promotionsberatern bzw. -vermittlern in Anspruch genommen, noch werde ich sie künftig in Anspruch nehmen.

Leila Noohinejad

Bayreuth, den 13.07.2016